Seakeeping Analysis and Hull Optimisation on Wet Deck Slamming of Fast Ferry Catamarans

by

Daniel Cao Chiew

Seakeeping Analysis and Hull Optimisation on Wet Deck Slamming of Fast Ferry Catamarans

by

Daniel Cao Chiew

to obtain the degree of Master of Science at the Delft University of Technology, to be defended publicly on Wednesday October 28, 2020 at 2:00 PM.

Student number:	4740165	
Project duration:	September 1, 2019 – October 1, 2020	
Thesis committee:	Prof. dr. ir. I. Akkerman,	TU Delft, supervisor
	Ir. H. R. Luth,	Damen, supervisor
	Dr. ir. A. A. Kana,	TU Delft
	Ir. J. Lotz,	TU Delft

Abstract

The present research performed a design exploration of fast ferry catamarans with hard chined demihulls sailing in irregular head waves, to analyse the influence of the demihull shape (without appendages) on wet deck slamming, and identify the geometrical properties and their trends to reduce it. Wet deck slamming is a phenomenon known to cause passenger discomfort and seasickness, often a source of delay in the ferry's schedule and can even cause irreversible damages and endanger the crew.

The research is carried out with numerical methods, where two main programs are used, namely the strip theory-based program for non-linear motions of high speed crafts FASTSHIP, and the design optimisation, parameter estimation and sensitivity analysis software, DAKOTA.

To set up the experimental analysis, design and analysis of computer experiments (DACE) methods are used. The use of DACE involved the application of an in-house built parametric design tool for mass generation of hulls, coupled with a sampling-based method for the exploration of the design space. Because DACE methods require a large amount of data points (of the order of tens of thousands), it is deemed unfeasible to perform all the analysis with FASTSHIP. Therefore, a surrogate model is built instead, with the global approximation-based method known as Kriging. By considering the surrogate model in the study, mass production and evaluation of different hull forms were achieved, which led towards a brute force surrogate-based optimisation approach. Such approach enabled an in-depth exploration of both sub-optimal and Pareto-optimal regions of the multi-objective domain, thus not only showing the hull characteristics of the best hulls but also their trend of change from the sub-optimal to the Pareto-optimal region. Additionally, an alternative approach based on evolutionary algorithm is coupled to the surrogate model for a more direct and straightforward optimisation process, namely the multi-objective genetic algorithm (MOGA). Both approaches converged towards the same region, thus reinforcing the reached solution.

The outcome of the research established a valid framework for performing hull design explorations on catamarans while addressing wet deck slamming. Furthermore, it showed that the demihulls should adopt bulkier forms. However, a trade-off existed between the various considered objective functions, hence the final decision should be based upon the user's criteria.

Preface

"YEEEEEEEAH BUDDY ! LIGHT WEIGHT BABEEEEEE ! …WUUUUUHHH !"

—Ronnie D. Coleman, 8 times Mr. Olympia

As an avid weightlifting enthusiast, I cherish strength in all its forms, physical and mental. In weightlifting, when someone is able to lift the heaviest weight to date for a single repetition, we call it a Personal Record (PR) and with the present work, I am hitting a life PR.

I would like to thank my supervisors Robert and Ido for their 'coaching', they guided me through this little journey and made this thesis possible. Thank you, Robert for your patience, you always welcomed me and my doubts, I felt treated both like a student and a colleague on equal parts, I will remember our non-work related life chats. Fun times. Thank you, Ido for your patience as well, I look up to your fast critical mind, your feedback not only was helpful to my work, but also taught me about the proper 'scientific approach'. Furthermore, a thank you to the Damen colleagues, rest assure my Damen-induced coffee addiction will be hard to forget.

Last but not least, I would like to thank my family and friends, your support meant the world to me. I would like to dedicate this work to my grandparents, who passed away during my time abroad. I love you.

Daniel Cao Chiew
Delft, October 2020

Table of Contents

Glossary

FFC Fast Ferry Catamaran

RAO Response Amplitude Operator

CFD Computational Fluid Dynamics

DOE Design of Experiments

DACE Design and Analysis of Computer Experiments

MOAT Morris-One-At-A-Time

LHS Latin Hypercube Sampling

MOGA Multi-Objective Genetic Algorithm

BFSO Brute Force Surrogate-based Optimisation

List of Figures

1

Introduction

Over the course of maritime history, ferry vessels have been evolving in size and performance with a clear trend towards greater transport capabilities and speeds. This pursuit for transport efficiency has led to the creation of many variations of many Fast Ferry Catamarans (FFCs) (and multihulls), where demihulls are fine-tuned to be as narrow as possible in order to reduce resistance while conserving buoyancy.

Australia exemplifies the evolution of FFCs. Australia is acknowledged in the field for being home to two of the most renowned FFC shipbuilders, Incat and Austal. The former is known for introducing the first wave piercing catamaran (WPC), depicted in fig. 1.1, which unlocked the path towards increasingly larger FFCs. These FFCs have relatively good performance. They have narrow demihulls that can pierce through the waves, but they are ridden with poor buoyancy, which is compensated with a centre bow.

Nevertheless, an obvious limitation that confronts the FFC series of designs is the environment, especially the open sea. When a rough sea arises, none of the vessels will perform ideally, and in the FFC case, unwanted motions will surge that not only lead to passengers and crew discomfort, but also to potentially irreversible damages to the hull itself. In such scenario, captains will immediately associate these motions with slamming,

Figure 1.1: First wave piercing catamaran from Incat, Tassie Devil 2001 fleeted on 1986

commonly pictured as an abrupt impact of the hull against an incoming wave that causes high local pressure peaks in a short span and a posterior structural whip. The most common zones in FFCs to receive slamming are the bow section of the wet deck[1]and the demihulls' under-keel. The former are recognised as the most critical area for FFCs to receive slamming, due to the nature of the wet deck arrangement and its high exposure whereas under-keel slams on the demihulls are less frequent due to their slenderness, and are therefore less critical, unlike for monohulls. Hence, the focus of the present study on wet deck slamming only.

The magnitude of the potential structural damage and consequent passenger and crew life endangerment can be extremely serious, as can be appreciated in fig. 1.2.

(a) Structural damage due to wetdeck slamming on HSS Stena Discovery during operations in the North Sea, in 1997

(b) Practical bow loss due to sever slamming on Ocean Lala during voyage from Penghy, Taiwan to Taichung, Chine, on August 2010

Figure 1.2: Examples of ferry catamarans sea incidents due to slamming

In the shipping world, captains are typically given information on the maximum sea state the vessel can sail on. Any higher sea state is to be avoided. The criteria to define this limit are provided by the designers and corresponding rules such as the SOLAS, classification societies and in the particular case of FFCs, the High Speed Craft code (HSC).

---

[1] According to the DNV-GL classification society rule for high speed and light crafts [6], the wet deck is defined as the flat cross structure between the hulls having an exposed, down-facing, horizontal or near-horizontal surface above the waterline.

Moreover, in the face of any contingencies, manoeuvring strategies, such as reducing speed or changing course of direction, might be adopted by the captain himself upon his judgement. Nonetheless, all these measures will affect the planned schedule of the ferry and could put the ferry company's business plan in a real predicament. Even without considering setbacks due to the stochastic behaviour of the sea, the ferry business world is fraught with uncertainties, and mishaps are most likely to happen. Yet it is undeniable the fact that the more availability a ferry has and the more travels it can make, the more profit the ferry business owner can make.

In summary, there is a complex framework of catamaran features that the FFC market generally looks for, namely a high gross weight-to-lightweight payload ratio, low resistance to ensure high design cruise speeds and good seakeeping performance. Not only do these parameters counteract themselves, but external elements such as the interaction with the environment in off-design conditions can also determine the shape of the optimum design space. The present work focuses on how the off-design conditions will influence the optimum design space with slamming as the only source of negative interaction between the hull and the sea.

1.1 Introducing the Nina

Nina is a FFC built by Damen Shipyards, a 40m LoA vessel with a capacity for 440 passengers. It currently sails in the Sea of Japan connecting Busan, South Korea with Tsushima, a westside island of Japan.

Figure 1.3: Damen-built fast ferry catamaran Nina, sailing in the Sea of Japan

Slamming has become a frequent issue in the ferry route of *Nina*, as depicted in fig. 1.4. As it can be appreciated, when departing from Tsushima *Nina* initially heads to the east and progressively turns towards Busan. This initial section of the route has been reported to be the most delicate, because waves are coming from the bow, a sailing situation highly prone to slamming. Therefore, the captain is often forced to slow down the speed in order to avoid any potential damages and ensure the safety of the passengers and crew. As mentioned, this kind of situations not only poses a hindrance to the ferry's schedule but also to its passengers, which now have to endure a delay.

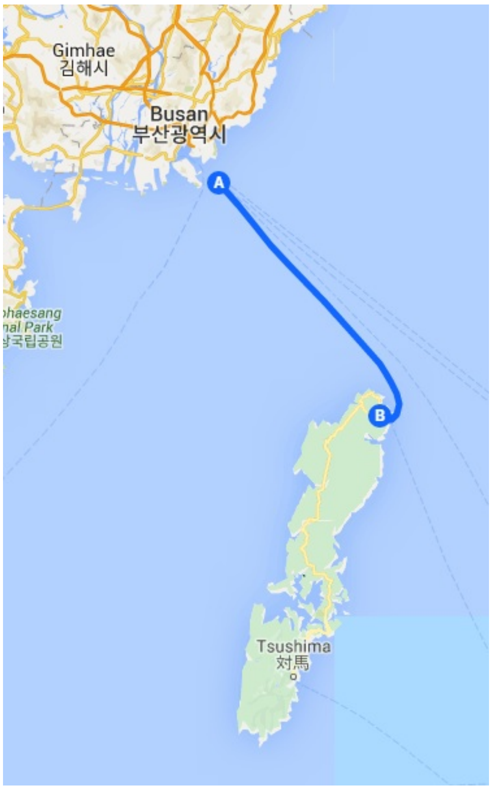

Figure 1.4: Ferry route between Busan, South Korea and Tsushima, Japan.

There is not a clear way of how to perfectly describe slamming nor how to perfectly model it in CFD. But its context is well understood as it is a byproduct of the relative motion between the hull and the waves. Ever since the first fast ferry, there have been many designs that pursued amongst other properties, the reduction of the relative motions thus reducing indirectly the chances of slamming.

The most straightforward solution to slamming is to rise the wet deck. However, as ship displacement increases such option becomes less feasible because the number of required stiffeners increases exponentially, causing a rise in the centre of gravity thus, stability can get penalised. Furthermore, operational difficulties can also ensue in loading/unloading mode at the port.

The design of the two demihulls has also been subject of many design endeavours, ranging from semi-displacement rounded demihulls and hard-chined demihulls to the aforementioned wave piercing catamaran. Moreover, different concepts have also been developed such as the SWATHs or air-cushioned catamarans. All of them have different attributes and advantages but comparing them is out of scope.

Other solutions to reduce slamming include the use of appendices or even hydrofoils. While the first choice might to a certain extent dampen the vertical motions of the vessel if fins are installed, which indeed reduces slamming, it also increases drag. The hydrofoil seems a very attractive option since in operational mode the hull is lifted above water and only the hydrofoils remain underwater. Furthermore, it conveniently solves the problem that accompanies the use of appendices since friction resistance is greatly reduced. However, hydrofoils are expensive, especially if they must be adapted to an existing hull. Moreover, depending on the sailing situation lift might drastically reduce or even disappear, for instance during broaching.

Therefore, the shipbuilding company Damen Shipyards wishes to perform a design exploration on their FFCs by purely modifying the demihulls shape, in order to analyze its effect on slamming with the aim to improve their seakeeping performance. With this premise, the scope of the present work will revolve around *Nina* as its study case, a starting point that not only provides a well defined scenario but also data availability.

1.2 Catamaran wet deck slamming current research state

The current research about slamming has explored all three major fields, namely full-scale sea trials, model scale experiments and numerical methods. Among them, full scale tests are the most non-deterministic and expensive, where the environment conditions cannot be controlled. Moreover, data tends to be poorer, as in practice heavy seas are to be avoided, thus only limited and specific slamming encounterings are recorded. Nevertheless, attempts to gather data from real cases has been carried out on many monohulls, as outlined by *Kapsenberg* [10] (2011) where some research focused on statistical data such as the probability of slamming, the number of propeller emergences per hour, bow acceleration or the probability of bow wetness. Others looked on the structural response like the vertical bending moments or impact pressures. The majority of the conclusions were rather general (given the uncertainty of the conditions but useful nonetheless. Like identifying the head sea conditions as the most prone for slamming). Furthermore, many of the slam events would occur even in situations well below the recommended by the classification societies. An effort was also made to estimate the relative impact velocity from the signals measured by pressure gauges, and a relation was found between the impact velocity and the peak pressure by Ochi et al. (1973) [17].

Full-scale experiments were also performed on catamarans, where considerable research about wave piercing catamarans has been done (where the majority of the found literature were often linked to an INCAT model or an Australian research institutions). As explained by *Shahraki J.* (2014) [22], several issues made it very difficult to correctly set the corresponding experimental environment, as setting up the instrumentation is a tedious process, ship owners are normally reluctant to drill holes in the vessel's hull and great difficulty lies in trying to reverse engineer the slam loads. Therefore, these type of experiments are not the most efficient or convenient. Thus, researchers tend to exploit more other alternatives such as model tests or numerical methods.

Model tests, despite still being a relatively expensive option, are a better alternative than full-scale experiments since many of the aforementioned issues can be better addressed such as the control over the environment and its conditions, making them less non-deterministic. Like full scale experiments, remarkable amount of research about slamming in WPC exists. Where *Shabani B. et al.* (2018) [21] performed various slamming tests and analyzed its structural effect by studying the influence of different center bow geometries and tunnel heights to a model of a $112m$ INCAT WPC, see fig. 1.5, for two different wave heights and various wave frequencies. All of them tested in head waves conditions and at same speed. Five different combinations of deck and center bow arrangements were tested, where the center bow was either shortened, enlarged and the wet deck lifted higher or put lower. The results showed that the higher wet deck and short center bow arrangement had the smallest slam loads. However, it also showcased the worst heave and pitch (the only allowed) motions. Thus, increasing the deck height can result in somewhat lighter slamming loads in expense of seakeeping performance, especially in following seas. Furthermore, it was also concluded that at resonance frequencies, typically at a non-dimensional encounter frequency $\tilde{\omega} = 4.5$, slamming was consequence of a highly heave-pitch coupling. Where the experienced relative wave length[2]was approximately $\lambda/LWL \approx 1.5$. While at $\lambda/LWL < 1$, typical of higher encountering frequencies, heave and pitch motions were smaller.

Although the experiments were focused on WPC, it can be extrapolated for standard FFCs that slamming occurrences are highly related to the encounter frequency with a relative wave length of $\lambda/LWL \approx 1.5$ suggesting that hull shapes cannot be optimized for all type of sea characteristics but only for specific ones. Therefore, designers should account for the significant sea state of the operational environment when choosing the vessels' length and design speed. Finally, it is worth mentioning that during the experiments, it was noticed how slamming often occurred when the bow was nosing down while a wave was incoming. And how subsequent interactions with the following incoming waves could enhance the heave-pitch motions, resulting in worser slamming occurrences, as further detailed in [22]. Suggesting the relevance of the context in which slamming occurs, which might be more accurate when accounting for the hull-wave interaction for a series of concatenated waves rather than focusing on single interactions, especially for an overall evaluation of ship performance in regards to slamming.

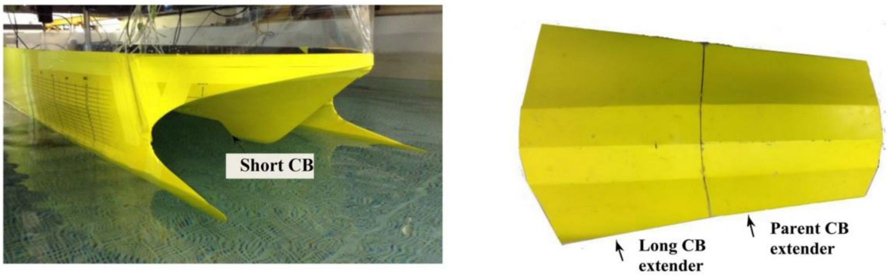

Figure 1.5: *Shabani B. et al.* 2018, photograph of the WPC parent model (left) and the center bow attachments (right)

Nevertheless, single wave-hull interaction has also been the center of attention in slamming research when the interest was focused at the local slamming loads and its subsequent structural response. Typically with free-fall tests of prismatic sections, hence considering 2D effects only, but limited amount of data is available for experimental set-ups of 3D models. Which in turns limits the available data for validating its counterpart with numerical methods. Therefore, *Swidan A.* (2015) [24] performed various 'constant drop velocity fall' experiments with both a prismatic section of a WPC fig. 1.6 and a generic INCAT WPC fore section fig. 1.7. Moreover, the data was subsequently used for validating numerical approaches by means of CFD. From the model tests, it was realized that the pressure gauges placed in the tunnel between the demihull and centerbow of the WPC model recorded the highest peak before even making contact with the mean free surface. Revealing the existence of waterjets and its severity and importance on wet deck slamming. As the hull continued to sink, the slamming force would decay but with a transient load, indicating structural wheeping effects. Furthermore, the pressure gauges at the aft-most location presented higher pressure peaks than the ones placed closer to the bow section. With a magnitude difference of the order of 2 times bigger for the aft-most pressure gauge with respect to the fore-most pressure gauge. This phenomenon highlighted the existence of 3D effects and how slamming can be highly dependent of the local wet deck geometry. Because water jets developed further inside the tunnel, that is, closer to the midsection,

---

[2] Ratio between the wave length λ and the vessel length at water level LWL

flow gets entrapped with nowhere to exit, opposite to water jets closer to the bow, that have the possibility to flow outside the tunnel area.

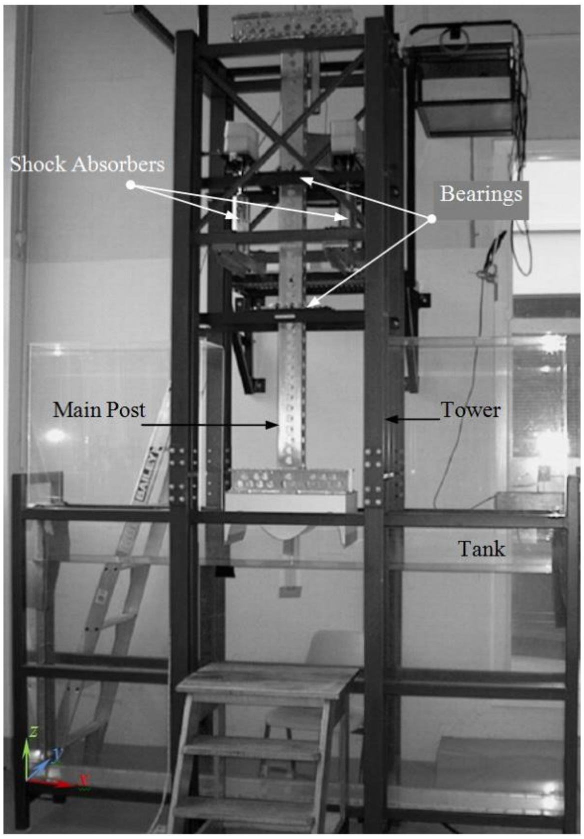

Figure 1.6: *Swidan A.* (2015), photograph of the quasi-2D free-falling drop test set-up at the University of Tasmania.

Moreover, a linear relation between the slamming peak force with the square of the water entry velocity was established, which opens the door to the possibility of building an empirical relationship of the type

$$F = av^2 \tag{1.1}$$

Where a is a constant factor that accounts for the relative impact angle between the local wet deck and the free surface. However, further experiments with varying trim angles and thus, relative impact angles, lead to big differences in slamming forces. The biggest impact forces were recorded when the relative impact angles were the smallest, suggesting that small changes in relative impact angles resulting in high load responses could be of non-linear behaviour. Nevertheless, further research is recommended. This study, although focused to WPCs, can also mean that for standard FFCs waterjets are not expected to be the main issue since the tunnel width in this type of ferries are roughly as wide as its demihulls separation, therefore the water pile-up at both inner sides of the demihulls are not as constrained as opposed to the narrow tunnels of WPCs. However, waterjets can still cause local loads to the structure therefore, further analysis should be made in order to quantify the magnitude of it and study the most suitable demihull-tunnel transition shape to damp or even avoid it.

Regarding the used methodology, local pressures have proved to be a poor indicator for slamming as they didn't provide enough consistency between hull shapes. Slam force

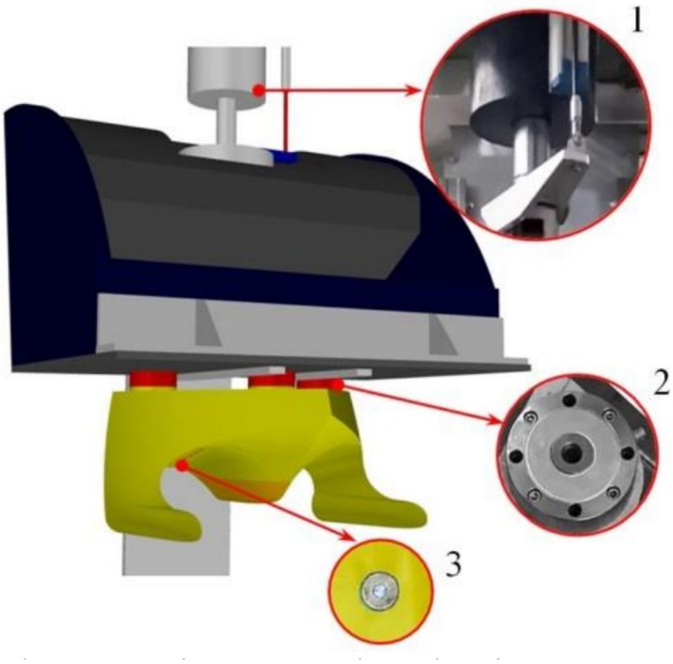

Figure 1.7: *Swidan A.* (2015), sketch of the INCAT WPC free-falling drop test set-up showing (1) LVDT and hydraulic ram cylinder, (2) load cell and (3) pressure transducer and fitting surface.

on the other hand, seems to be more consistent as pressure peaks are averaged over an area.

Numerical methods are generally the most economical option, they are fully deterministic and can offer a greater insight to the slamming phenomena. However, there is still a lack of an accurate and numerically stable method for predicting slamming, specifically for 3D problems. Nevertheless, the methods range from 2D analytic approaches to full 3D CFD approaches, as described next.

Analytical approaches are fairly simple and fast methods to predict slamming. However, due to the complexity of the problem, only simple 2D analysis exists, mainly due to the difficulty in describing the dynamic behaviour of the free surface and moreover, because of the water-air interaction in catamarans' wet deck slamming.

A very well-known model is the Von Karman wedge entry problem, where the added mass is modelled as half the mass of a cylinder with a diameter equal to the submerged wedge beam. Wagner further extended the work by considering the water pile-up effect as the wedge penetrates the free surface, using potential flow theory. *Bisplinghoff* and *Doherty* (1952) [4] performed a validation procedure by comparing both methods (among others) with the results from free-fall tests with various wedges. The maximum acceleration and added mass resulted in fair agreement with Wagners' method when the dead rise angles were between $20° - 30°$ but would predict poorly outside these bounds.

A more sophisticated approach is the Boundary Element Method (BEM) based on potential flow theory. It discretizes the space domain with panels and solves the pressure field by means of Bernoulli's equation at the meshed body surface. This method delivers a higher slamming prediction accuracy than analytical approaches. Moreover, it also allows for broader geometry explorations. However, complex local free surface deformations can be (too) difficult or rather impossible to model, because it would require a dynamic mesh refinement that would systematically increase the local mesh density in order to ensure the length scale of the panel sizes are always smaller than the local water deformation, for instance, of a waterjet, as outlined by *Kapsenberg* [10]. Thus, typical choice is made to neglect local water deformations and just assume atmospheric pressure at the free surface instead.

Therefore, CFD methods are the general choice when research is focused on local slamming loads due to water deformation. There are different discretization methods for both, time and space within CFD to solve the Navier-Stokes equation in order to predict slamming. In the work of *Swidan A.* (2016) [24], a CFD approach for the simulation of a quasi-2D wedge water entry problem was performed, followed by a validation procedure with its counterpart in model tests, as in fig. 1.6. The results were also compared to the same experiment carried by *Shahraki J. et al.* (2011) [22] using Smoothed Particle Hydrodynamic (SPH). SPH, is a mesh-free Lagrangian method to simulate fluid flows, which is represented by defining the particles directly, thus mass conservation or fluid properties such as density are directly represented by the particles distribution in space. And pressure is computed from weighted contributions between the neighbouring particles, thus there is no need to solve a linear system of equations, unlike CFD methods. Moreover, two phase flows are implicitly defined by the existence of the particles themselves as representation of the denser fluid and the empty spaces as the lighter fluid, typically air. Therefore, as long as the inter-particle relations are defined correctly, the particles are free to go anywhere. Regarding the applied CFD method, the program STAR-CCM+ Version 7.06 was used, with a multiphase segregated fluid model (water and air) applied to solve the conservation equations for mass, momentum, and energy for each phase. Pressure-velocity coupling was solved using a Semi-Implicit Method for Pressure-Linked Equations (SIMPLE) algorithm (available in the program). The space domain was discretized with two types of overlapping grids, a stationary background grid that meshes the far-field and an overset grid attached to the moving wedge, which would be remeshed if necessary when cell deformation were no longer acceptable (due to the moving wedge). The interface between water and air was modelled using the Volume of Fluid (VOF) method. Furthermore, in order to preserve the sharpness (i.e. avoid smearing) of the interface, the High-Resolution Interface Capturing (HRIC) scheme is used for the discretisation of the non-linear convective term in the momentum equation of the volume fraction. The comparison resulted in a more positive response by the CFD method, as vertical velocity, acceleration and pressure were in very close agreement with the experimental results, compared to SPH. From the results it was concluded that the inclusion of air in the problem was very important, thus two-phase flows must be included in the flow model.

From the 2D study, an analogous test with a 3D INCAT WPC model was also performed. The space was discretized with the same overlapping mesh technique — background mesh and overset mesh— and the interface described with a VOF method with a HRIC scheme. The fluid was modelled as a multiphase flow with RANS equations and the turbulence approximated by the two-equation SST (Shear Stress Tensor) eddy viscosity model $\kappa - \omega$. The method proved to be in great concordance with the experimental data, for the first slamming peak, as both force and pressure were behaving in the same way, thus successfully capturing 3D effects. However, the model was unable to capture the following transient whipping loads, only the general decaying trend [23].

Another similar CFD approach was taken by *Hang Xie et al.* (2018) [26], who simulated various 2D wedge water entries (at constant speed) for the bow section of a container ship. The simulations were performed with non-symmetrical characteristics by considering combinations of a non-zero heel angle or a non-zero horizontal velocity during the drop. Thus two types of asymmetries are defined, geometrical asymmetry and kinematic asymmetry.

The program used was the commercial CFD package of ANSYS, FLUENT, the Navier-Stokes equation was used to compute a multiphase flow with the VOF method for the interface. The chosen space discretization scheme was FVM, thus a unit width was implemented. The FVM method was coupled with a dynamic mesh that would move with the geometry. The results were validated against previous works and data available in the field. The study proved the importance of considering air effects on slamming. Furthermore, it also determined how horizontal velocities during the drop had a greater effect than heel angle changes on the horizontal slam force thus, kinematic asymmetry is predominant in this case. While the vertical slam force was mainly sensible to changes in heel angles, thus more sensitive to geometric asymmetries.

Therefore, it is inferred that currently CFD approaches with the above mentioned features can correctly assess the magnitude of the maximum slamming forces and the evolution in time for simple scenarios but full simulations of extended periods of time in irregular waves with same methodology are still too costly.

In summary, slamming has been the interest and the topic of many researchers and institutions with the aim to understand it better and acquire enough physical insight for better predictions. Studies had shown the relevance of air inclusion on the fluid models, and how local deformations of the free surface can result in big structural damages. Furthermore, the consequences of slamming on the wetdeck are not limited to the highest peak force, that is, the first perceived load. The following transient load known as whipping can also be of critical importance, which currently CFD methods are not able to accurately predict.

Slamming is a phenomenon that can affect all the vessels sailing around the globe, however studies tend to be either too general and thus, not specific enough for the different particularities of the various hull shapes or too specific, thus making it difficult to extrapolate the knowledge to other cases. Furthermore, the great majority of research in slamming focuses on the consequences to the structure by assessing the magnitude and severity at local areas. But not many focus on the influence of hull forms or the effects of specific hull parts on slamming, especially for the FFCs such as fig. 1.3, which is the aim of the present work. Hence, the pursuit of an understanding on how demihull shapes can influence wet deck slamming on FFCs leads to the following main research question.

1.3 Research question

What are the hull shape properties that enhance the seakeeping performance of a fast ferry catamaran by reducing wet deck slamming given a certain sea state ?

The main goal of the research question is hence, to name the hull characteristic(s) that can lead towards the reduction of wet deck slamming of FFCs or even potentially eliminate it. Furthermore, the trend of such characteristics towards wet deck slamming reduction will also be explored.

The means to carry such research will be numerical methods. In order to address the main research question, the following subquestions are proposed:

- *What is slamming?*
  From the literature review it is inferred that slamming can be defined either statistically or with a physical magnitude. In numerical analysis, the former is commonly used when extensive periods of seakeeping simulation are held, typically with lower accuracy programs that do not capture local effects, whereas the latter is more commonly used in more accurate programs for short periods of time simulation (typically in free fall test experiments) due to its higher computational cost.

  In the present research, the numerical modelling of wet deck slamming is approached with the impulse formulation, defined as the integral of a (slamming) force with respect to time. Such approach, enables to capture the interaction between the free surface and the wet deck through both, time and space. And focuses the analysis of slamming for large periods of sailing simulation.

- *When does slamming occur?*
  Continuing from the previous subquestion, slamming is considered to potentially occur whenever impulse exists, which will only happen when the free surface exceeds the wet deck. Thus, reducing the chances of impulse will also reduce any potential slamming.

- *What physical phenomena are relevant to the present research? And which can be neglected?*
  The present research relies on the prediction of the ship motions in order to model the interaction between the free surface and the wet deck. The ship motions are modelled with the equations of motion, where two main forces are distinguished, the hydrostatic and the hydrodynamic forces. Therefore, the main physical phenomena to account are the dynamic forces that participates in the ship motions.

  Local water deformations leading to waterjets under the wet deck will not be accounted in the research, thus the corresponding viscous effects of such phenomenon will be negelcted.

- *What characteristics should the numerical tool have?*
  The motions of any fast craft sailing in irregular waves are non-linear as outlined by *A. J. Keuning* (1994) [11]. Therefore, to capture them, a time domain based numerical tool has to be used.

- *What criteria or method should be used to find the optimum design(s) ?*
  Various approaches can be taken in order to improve an existing hull design which could experience less wet deck slamming while sailing. In order to ensure a holistic and methodical approach, a Design of Experiment (DOE) study and optimisation algorithm will be used to understand the hull influence on slamming.

1.4 Scope

The FFC *Nina* introduced in section 1.1 will be used as case study to perform the research of the present work. Hence, its operational profile will define the scope of the present work as constraints. As aforementioned, the Sea of Japan will be the environment considered in the research, where *Nina* connects Busan-Tsushima with an operational (cruise) speed of $30kn$.
For the sake of simplicity, only head waves sailing conditions will be considered, which according to the literature review is also the most critical condition due to higher chances

of slamming. Therefore, the six degrees of motion are reduced to heave and pitch only. Furthermore, in order to make the potential new hull designs relatable between each others, same displacement and deck layout as the original hull are imposed. The only allowed degrees of freedom for modifying the hull are the demihull lines, where appendices and varying the wet deck height are forbidden (because they would blur the effect of the hull shapes on slamming and thus, deviate from the true aim of the thesis topic). The aforementioned constraints can be found summarized in table 1.1.

Environment	Sea of Japan
Hull type	Semi-displacement
Speed	30 kn
Displacement	Full load departure condition
Deck layout	Same as the parent hull

Table 1.1: General constraints of the problem

The details concerning the considered numerical tool, hull type and environment are further explained below.

1.4.1 Numerical tool

According to the literature review, satisfactory slamming predictions can be obtained with CFD programs solving for the set of RANS equations. However, such high-fidelity numerical approach demands a relatively long simulation duration, for which the present research lacks the corresponding computational resources and most importantly, time. Thus, lower-fidelity programs are considered. One degree down in the rank would be, for instance, BEM. Potential flow-based programs are a promising choice given their relatively faster computational process and that they are sufficiently physics-based to respect the hull geometry. However, a degree down in program fidelity is preferred for the sake of a faster computational process thus disembarking into analytically based approaches. Amongst the various analytically based programs, the strip theory-based program for non-linear motions of high- speed crafts, FASTSHIP is chosen.

Lastly, in order to explore the influence of the hull shape and its relation with slamming, the multilevel parallel object-oriented framework for design optimisation, parameter estimation, uncertainty quantification, and sensitivity analysis software DAKOTA will be used. With DAKOTA, a ready-to-use platform for the application of Design of Experiments, optimisation and data sampling (amongst others) can be provided.

1.4.2 Hull

The hull types to consider in the research will mainly depend on the geometry requirements of the selected program, namely FASTSHIP as above mentioned, which can only handle hard chined hulls. Thus, FFCs from the FFC catalogue of Damen complying with such requirements will be used in the research. Hence, the FFC known as the 4212 is introduced, which is a hard chine-type FFC of 42 m, further introduced in chapter 3.

The modelling of hull shapes will be carried by a parametric design tool, which will enable for an easy generation of off-springs based on the specified parent hull. Hence, enabling an inexpensive mass production of hull geometries.

1.4.3 Environment

The Sea of Japan will be the environment used to perform the research, specifically the sea conditions along the ferry route of the *Nina*.

The Sea of Japan is enclosed between the Japanese archipelago, the Korean peninsula and the Russian mainland, thus it is isolated from the Pacific Ocean. Therefore, the sea conditions are quite constant over the seasons. Below, the average conditions of the significant wave height of the combined wind-waves and swell, mean wave period and mean wave direction over the winter season are illustrated. The data are obtained from the European Center for Medium-Range Weather Forecast (ECMWF), for the period of 2018, the most recent data available for a year's span. The data was examined across the different seasons, in order to identify the worst case scenario that on average happens between Busan and Tsushima.

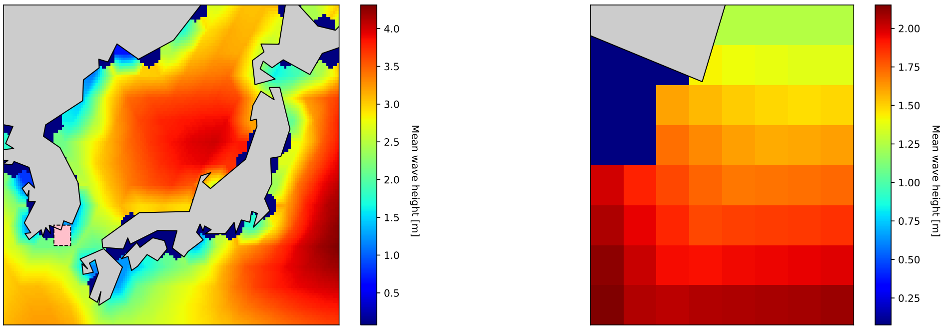

(a) Color map of the significant wave height of the Sea of Japan. **(b)** Color map of the significant wave height of the Busan-Tsushima area

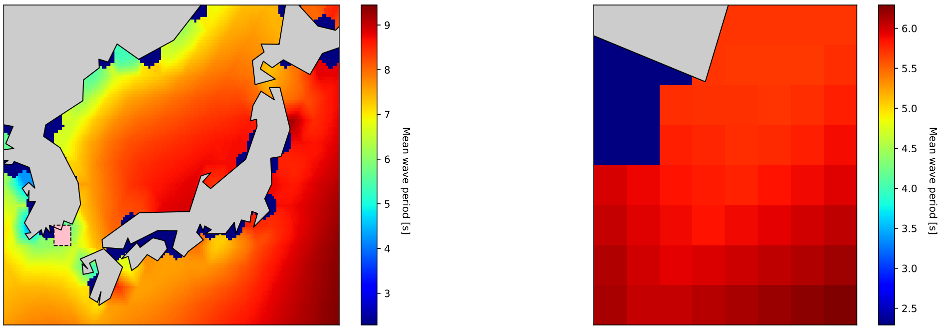

(c) Color map of the mean wave period of the Sea of Japan. **(d)** Color map of the mean wave period of the Busan-Tsushima area

Figure 1.8: Part 1 of 2. Environmental analysis of the Sea of Japan (left column) with the operational area of the *Nina* ferry route highlighted with a pink box (zoomed in right column), illustrating the significant wave height of the combined wind-waves and swell, mean wave period and mean wave direction in Winter.

The local characteristics of the sea for all seasons are summarized in table 1.2.

These sea characteristics do not seem particularly extreme for a vessel of the size of the *Nina*. However, after a more in-depth look it is realized that the reason why *Nina* has been reported to suffer from frequent slamming can be explained by the relative wave

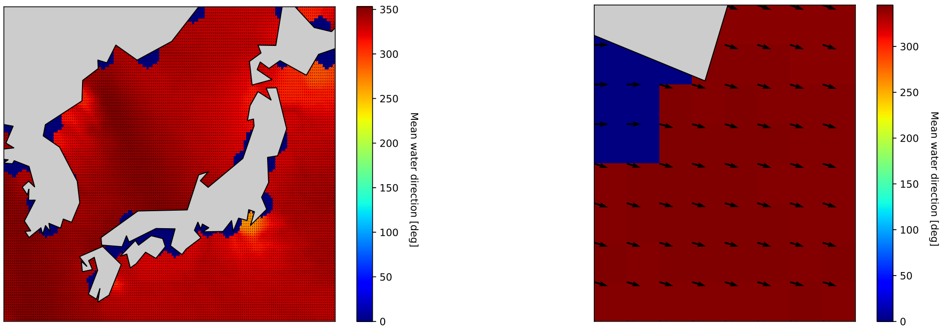

(e) Colormap of the mean wave direction of the Sea of Japan **(f)** Colormap of the mean wave direction of the Busan-Tsushima area

Figure 1.8: Part 2 of 2. Environmental analysis of the Sea of Japan (left column) with the operational area of the *Nina* ferry route highlighted with a pink box (zoomed in right column), illustrating the significant wave height of the combined wind-waves and swell, mean wave period and mean wave direction in Winter.

	Winter	Spring	Summer	Autumn
Hs [m]	2.09	2.06	1.55	1.64
Ts [s]	6.18	6.40	7.27	6.41
θ [deg]	344.28	290.54	216.24	321

Table 1.2: Significant 1/3 means of the wave height, wave period and wave direction at the vicinity between Busan and Tsushima

length λ/LWL, which can be obtained from the wave dispersion relation.

$$\begin{aligned} \omega^2 &= kg \\ \left(\frac{2\pi}{T}\right)^2 &= \frac{2\pi}{\lambda} g \\ \lambda &= \frac{T^2 g}{2\pi} \end{aligned} \tag{1.2}$$

For a mean wave period of 6.18s the relative wavelength becomes approximately 1.5. Therefore, as outlined by *Shabani B. et al.* [21] resonance can happen, especially for the headwaves and bow-quartering waves sailing situations (which is the most frequent sailing condition when sailing from Tsushima to Busan, as it can be appreciated from the mean wave direction colormaps of fig. 1.8e and fig. 1.8f).

To simulate the environment, a Jonswap spectrum with the Winter's sea characteristics; $Hs = 2.09$ m, $Ts = 6.18$ s will be used (as detailed in table 1.2). The reason for using the Jonswap spectrum is because amongst the different seasonal sea characteristics, the worst case scenario is considered, but is not expected to remain as such during the entire season meaning, a developing-sea is expected instead. Furthermore, during winter the significant mean wave direction according to the metocean data, shows that waves goes from north-west to south-east. The combination of such direction with the local geography (where South Korea and Japan are the closest) results in somewhat limited fetch, which complies with the Jonswap spectrum sea modelling assumptions as well.

1.5 Road map

The content of the above introduced thesis' topics will be further developed in the following chapters:

- **chapter 2 — Parametric hull design:** This chapter proposes a parametric design tool for the generation of hull forms based on the Wigley hull. By considering a parametric hull, infinite hulls can be generated inexpensively and ready to be analysed for their seakeeping performance with regards to slamming. Furthermore, the geometrical capabilities of the tool are explored and a special adaptation for FASTSHIP is realised.

- **chapter 3 — Numerical analysis:** In this chapter, the numerical approach to model wet deck slamming is introduced, thus answering the following research subquestions:

    - *What is slamming ?*
    - *When does slamming occur ?*

  Furthermore, the program FASTSHIP is introduced and the corresponding results discussed. By justifying the program choice the following subquestions are answered:

    - *What physical phenomena are relevant to the present research ? And which can be neglected ?*
    - *What characteristics should the numerical tool have ?*

- **chapter 4 — Design of Experiments:** In this chapter, the analysis to understand the effects of the hull forms to wet deck slamming is addressed. To achieve that, first a sensitivity study of the parametric design tool is performed in order to ensure its correct definition. Next, a sampling-based method is applied to populate the design space and use them as training points to build a surrogate model of FASTSHIP, enabling mass evaluation of hull forms, also known as brute force search, and finally, the subsequent results are discussed. This chapter answers the subquestion:

    - *What criteria or method should be used to find the optimum design(s) ?*

- **chapter 5 — Optimisation:** This chapter continues with the Design of Experiments methodology introduced in the previous chapter, consisting in the application of two optimisation methods coupled with a surrogate model. Namely Brute Force (BF) optimisation and Multi-Objective Genetic Algorithm (MOGA). A small discussion comparing the performance of both methods is realised as well.

- **chapter 6 — Conclusions:** The conclusions of the research and additional remarks can be found in this chapter.

Each chapter embodies a main process of the thesis, in order to understand better the relation between them a flow chart displaying the chronological process along with some important subprocesses are displayed, see fig. 1.9.

As it can be appreciated, the process starts with a data sampling method which will arrange the corresponding data for the parametric design tool to produce the corresponding hull shapes. The hulls will be evaluated with FASTSHIP, and the obtained responses used to build a surrogate model. Finally an optimisation process can be performed in order to search for the optimum design space.

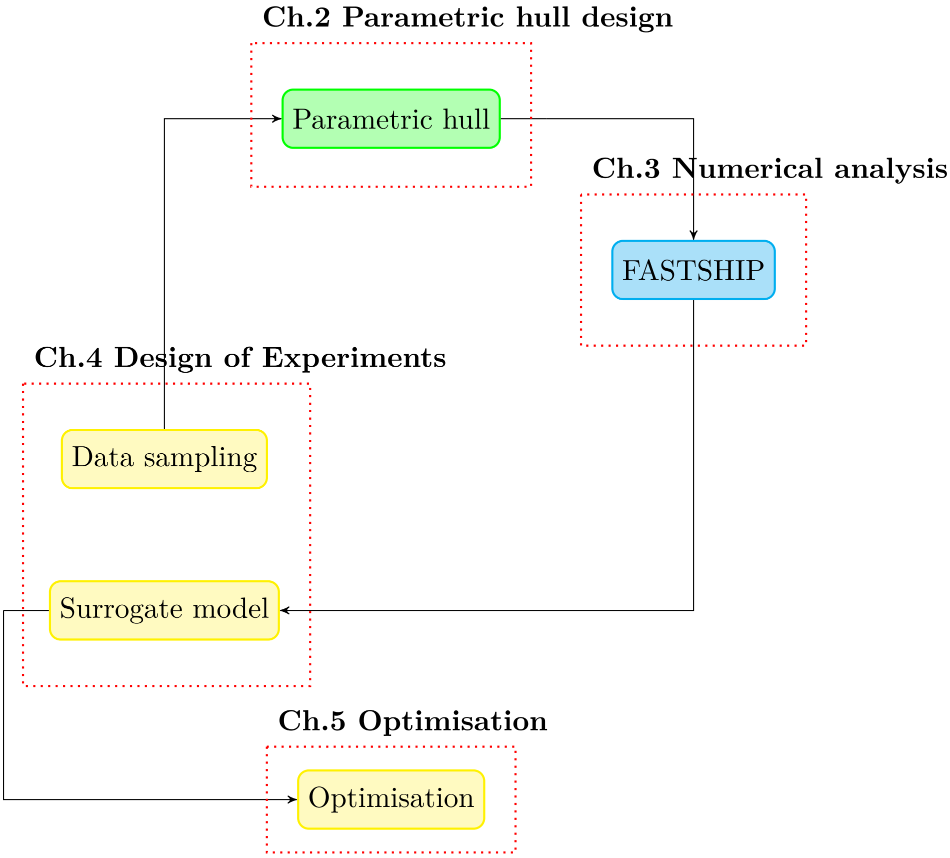

Figure 1.9: Flow chart of the chapter's arrangement

2

Parametric hull design

In order to perform a design exploration in an efficient and inexpensive manner, a parametric design space is established. The goal of setting such design environment is to allow for mass generation of different hull variations in a controlled and methodical way, and moreover, bridge seemingly into the numerical approaches that will evaluate them.

Furthermore, the parametric hull model can be implemented as part of a larger parametric process, where tedious steps such as pre-processing and post-processing can be carried out without any hiatus (otherwise, requiring a user to manually design a new hull, translating it to the correspondent geometry input file and commanding the start of the new evaluating process), as displayed in fig. 2.1. Thus, building a seemingly closed loop that can automatically evaluate a pre-defined population of hulls, and collect the results in an archive for post-processing.

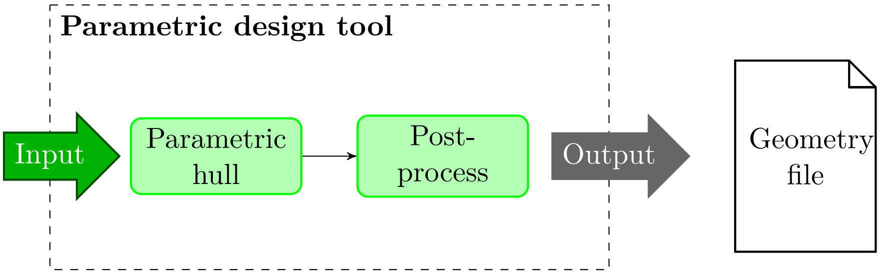

Figure 2.1: Flow chart of the parametric design tool processes

The parametric design tool is based on the Wigley hull, which is a very simple yet well known mathematical hull within the academic field. A modification to the Wigley hull model is proposed in order to expand its design space and include more complex shapes. However, as mentioned in the introduction chapter, due to the geometrical requirements of the program used for the evaluation of wet deck slamming where only hard chined hull forms are supported, the research will mainly focus on the design exploration of hard-chined hull shapes.

In the present chapter, the parametric design tool will be described by first introducing the Wigley hull, and after a thorough analysis, the modifications are proposed. The design capabilities are discussed and tested by modelling cross sections from different hull types, including the *Nina* (introduced in section 1.1). Furthermore, a special adaptation is performed in order to comply with FASTSHIP geometrical requirements.

2.1 Wigley Hull

In the maritime academic field, the Wigley hull is often used as a test hull for the research of certain hydromechanic aspects. Given the parametric feature and the simplicity of its formulation, it is not only very convenient but also very easy to comprehend. The Wigley hull is described by three main parameters, the length overall L, breadth B and height T.

$$y(x,z) = \frac{B}{2}\left[1-\left(\frac{x}{L}\right)^2\right]\left[1-\left(\frac{z}{T}\right)^2\right] \tag{2.1}$$

Where $x \in [-L, L]$, $z \in [-T, T]$ and $y(x,z) \in [0, B/2]$. After a thorough look, one can realize that the above expression describes a surface where the space variables along the hull length and depth x and z respectively, are quadratically related to the space variable along the breadth y. Resulting in a continuous surface, bounded within a domain described by the main parameters L, B and T, that resembles to the port side of a hull. In fig. 2.2, fig. 2.3 and fig. 2.4, illustrations displaying the Wigley hull with different input values are shown.

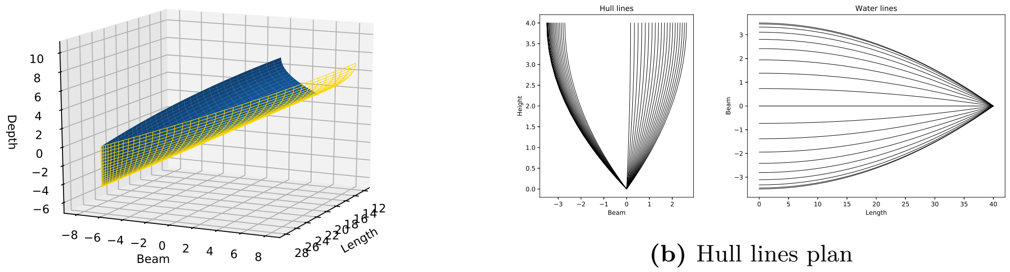

(b) Hull lines plan

(a) 3D view

Figure 2.2: Wigley hull with: $L = 40$, $B = 7$, $T = 4$

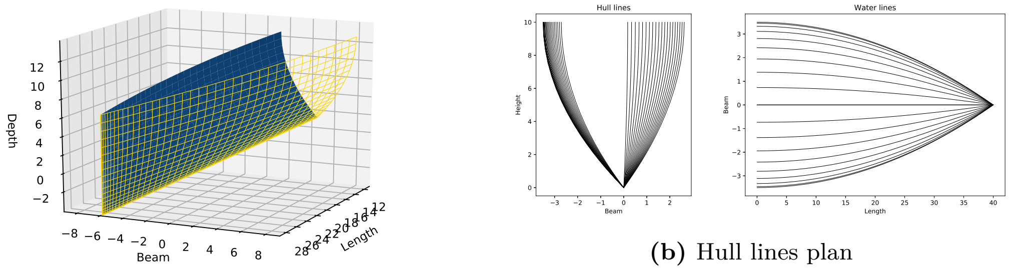

(b) Hull lines plan

(a) 3D view

Figure 2.3: Wigley hull with: $L = 40$, $B = 7$, $T = 10$

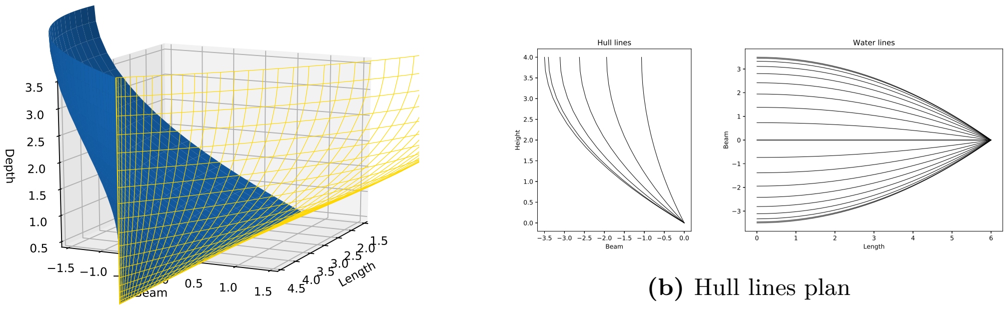

(b) Hull lines plan

(a) 3D view

Figure 2.4: Wigley hull with: $L = 6$, $B = 7$, $T = 4$

As it can be appreciated, although different L, B and T values were considered, there are certain similarities across all the illustrated hulls. The lines plan are somewhat similar to one another, and it is due to the aforementioned quadratic relation between the variables in eq. (2.1), which relates the end points between keel-deck and stern-bow in the same way. Thus, it is not possible to reproduce other shapes; for instance, bulkier forms typical of container ships, would probably require a different relation between the variables.

Disassembling the Wigley hull

In order to understand better the criteria behind the proposed modifications, a closer insight into eq. (2.1) is necessary.

The Wigley hull formulae can be broken down into 3 main parts, explained from right to left. The two rightmost terms, are 'coefficients' that varies from 0 to 1. While the first term is just a constant, which marks the maximum attainable value of $y(x,z)$ when the aforementioned terms are 1. Thus, one could consider $y(x,z)$ as a ratio of $B/2$, dictated by the product of $\left[1-\left(\frac{x}{L}\right)^2\right]$ and $\left[1-\left(\frac{z}{T}\right)^2\right]$.
A detailed description of the mapping mechanisms to describe such surface is explained next.

1. Assuming x and z are contained in the intervals $[0,L]$ and $[0,T]$ respectively, the following is true.

$$\frac{x}{L}, \frac{z}{T} \in [0,1] \quad \forall \quad \{x| \in [0,L]\} \ni \{z| \in [0,T]\} \tag{2.2}$$

2. Squaring the terms will not change the interval's domain (i.e. $([0,1])^2 = [0,1]$) but it will cause a quadratic behavior.

$$\left(\frac{x}{L}\right)^2, \left(\frac{z}{T}\right)^2 \in [0,1] \tag{2.3}$$

3. Subtracting the previous terms from a unit will swap the intervals order. This way, when x and z are 0, the terms becomes 1. And when x and z are L and T respectively, the terms become 0.

$$1-\left(\frac{x}{L}\right)^2, \quad 1-\left(\frac{z}{T}\right)^2 \in [1,0] \tag{2.4}$$

It is worth mentioning that the side view lines plan of the deck, keel and bow are straight with no possibility of alteration. Hence, from a side view the Wigley hull looks like a rectangle of length L and height T.

In summary, the geometries that can be attained by the Wigley hull formulae, from a design point of view, are stiff and unable to describe the desired hulls of interest. Nevertheless, a modification is proposed in order to enhance the design space and expand the design constraints, as explained next.

2.2 Wigley hull modification

The proposed modifications, changes the original quadratic term by the function $m(x)$ and introduces a new one $q(x)$, from now on known as form factors. Furthermore, the breadth and depth terms B and T respectively, which are constants in the original expression, are substituted by the functions $b(x)$ and $T(x)$ respectively. These changes basically replace the constant terms of eq. (2.1) by an analogous varying value along the hull length. The modified expression then becomes

$$y(z(x)) = b(x)\left[1 - \left(\frac{z(x)}{T(x)}\right)^{m(x)}\right]^{q(x)} \tag{2.5}$$

where $z(x) \in [0, T(x)] \quad \forall \quad x \in [0, L]$. The breadth and depth terms $b(x)$ and $T(x)$ respectively will be addressed further below.

The form factors $m(x)$ and $q(x)$ are subjected to certain constraints, otherwise unfeasible shapes can arise. To better understand these functions, fig. 2.5 shows a comparison of the cross sections that can result from different form factor values with respect to the original Wigley hull expression (where $m = 2$ and $q = 1$). The first thing to mention is that m and q cannot be 0, since any nonzero number raised to the 0 power will become 1, resulting in a straight line as it can be appreciated. And neither can they be negative, as the formula is not intended to work with inverse relations.

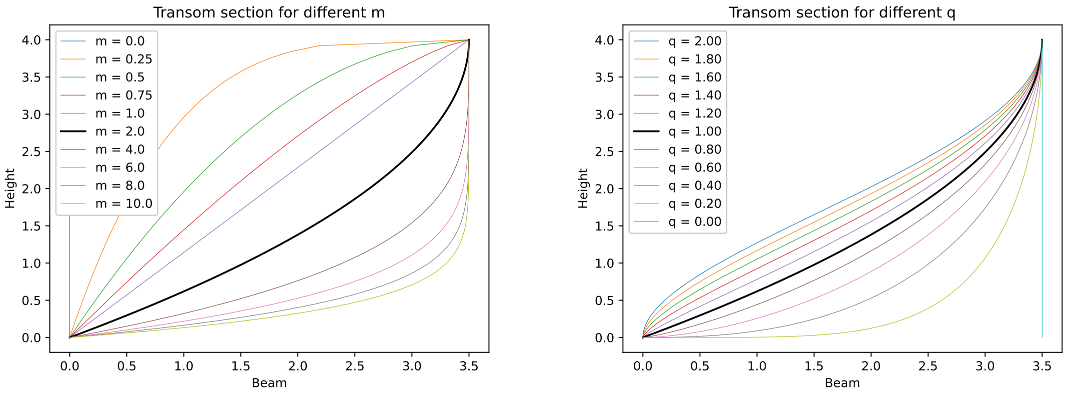

(a) m variations at $x = 0$ and $q = 1$

(b) q variations at $x = 0$ and $m = 2$

Figure 2.5: $m(x)$ and $q(x)$ effect on the transversal shapes

Therefore, the following constraints results

$$m(x) > 0 \quad \forall \quad x \in [0, L]$$
$$q(x) > 0 \quad \forall \quad x \in [0, L]$$

In fig. 2.5a it can be appreciated how for $m = 1$ a straight line is obtained, because a linear relation is imposed. But when $m \neq 1$ the resulting curves tends to hinge around the top right corner, where for $m < 1$ the curves hinges inwards and when $m > 1$, it hinges outwards. Resulting in hull sections that can vary from high-speed-like V-type hull sections to containership-like rounded chine hull sections.
Further sub-variations can be achieved by varying q, which causes a hinging effect around the bottom left corner, as illustrated in fig. 2.5b for a case with $m = 2$. Needless to say, when $q = 1$, no variation will result but when $q < 1$, the curve hinges outwards and when $q > 1$, it hinges inwards.
Further explanations of the effect of the form factors over the resulting cross section are detailed in section 2.2.1.

By specifying a different combination of form factors for every section along the $\hat{x}$ axis, an evolving cross section shape from transom to bow can be attained, thus enhancing the design space of the original Wigley hull. However, in order to ensure surface smoothness, the $m(x)$ and $q(x)$ functions can't have any discontinuities.

Both eq. (2.1) and eq. (2.1) are continuous functions, however in the computational domain a discrete interpretation must be carried out. Thus, once the form factors $m(x)$ and $q(x)$ are set, next is determining what type of point distribution best suits the given shape.

As aforementioned, one of the reasons to demand a parametric hull is the design exploration within a CFD analysis context, where a mesh is required for describing the geometry. Hence, the way to discretise the geometry becomes a factor to account for within the parametric design tool. The most complex type of geometry required among the chosen numerical methods is the surface[3], thus the most complex geometry input file to be accounted will require 3-dimensional points that are contained in the hull surface. In order to efficiently use the computational resources, a discretisation scheme is introduced with the aim of distributing a finite amount of points in the most efficient way possible, so the geometry that results from eq. (2.5) can be fairly described. The cosine point distribution scheme along the transversal and longitudinal directions is used for the matter, respectively shown below.

$$\begin{cases} z(x) = T(x) \cdot \cos\left(\frac{\pi}{2(N-1)} i\right) \\ x = L \cdot \cos\left(\frac{\pi}{2(N-1)} i\right) \end{cases} \qquad \text{for} \quad i = 0, 1, 2, \dots N-1 \tag{2.6}$$

In order to see the effect of the point distribution scheme, in fig. 2.6 two different schemes are applied to the curves introduced in fig. 2.5b, each with a set of $N = 20$ points to describe the corresponding shape. In the left plot an even distribution scheme is applied while in the right plot a cosine distribution scheme is applied. The differences between the two schemes becomes obvious in the lower order curves, where the combination of m and q results in very 'curvy' profiles. For instance, when $q = 0.20$ illustrated by the cyan curve, a 'bulky' rounded hull section is obtained. As it can be appreciated in the right plot, the cosine scheme shows that the bottom portion of the curve (keel area) is flat. While on the left plot, the even distribution scheme shows a certain dead rise angle due to not having enough points in the area, which can lead to the wrong idea of the bottom

---

[3] From the main numerical tools accounted in the present research, namely FASTSHIP and PANSHIP, the former requires 2-dimensional coordinates to describe the hull sections while the latter requires 3-dimensional coordinates to describe a surface. Therefore, the most complex type of geometry in the present research is the surface.

section being just an angled flat wide plate. Therefore, depending on the cross section profile shape, a higher density of points at the bottom part is necessary, or else details might be completely missed.

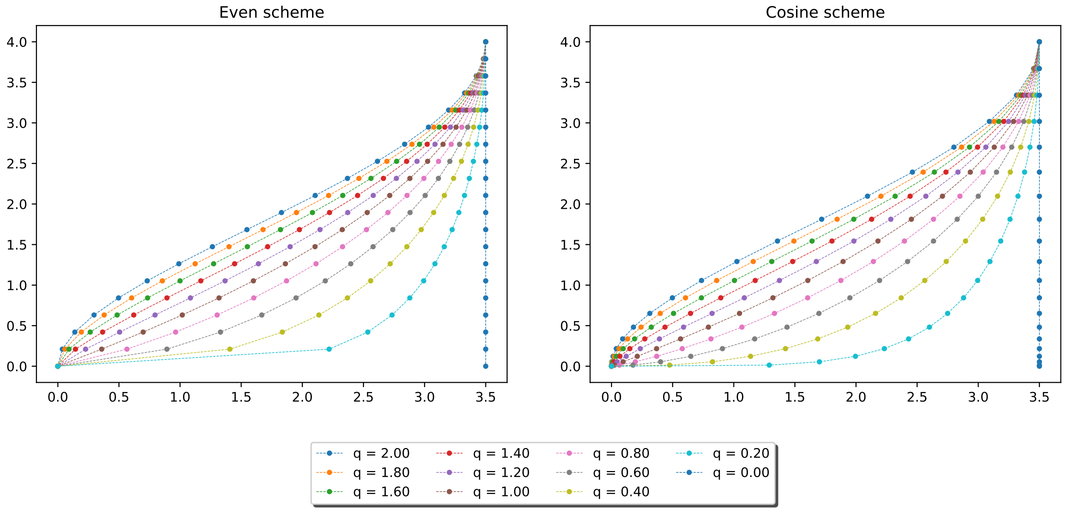

Figure 2.6: Point distribution scheme comparison for various q values and $m = 2$. Left plot has an even distribution of points along the vertical axis. Right plot has a cosine scheme applied along the vertical axis, with the point resources concentrated on the keel area

Breadth term: b(x)

Like in the original Wigley hull, the breadth term specifies the maximum breadth of the hull, which as shown in the first figures occurs at the transom, while the remaining terms specifies the rate at which the local breadth reduces as one moves towards the bow. The breadth function $b(x)$ allows for a different rate of change, thus marking a different local maximum breadth along the longitudinal direction $\hat{x}$. The expression is as follows

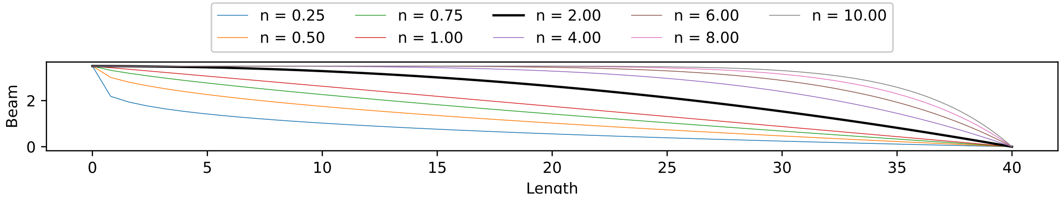

(a) n variations with $p = 1$

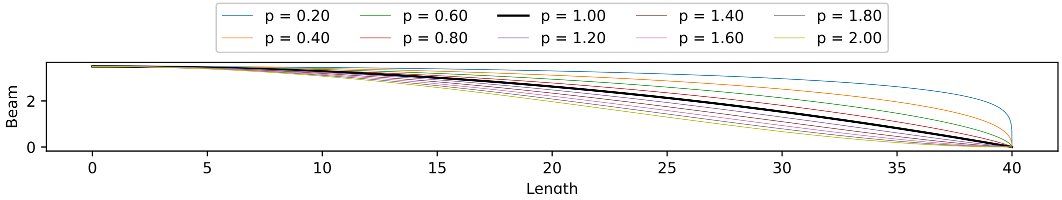

(b) p variations with $n = 2$

Figure 2.7: Different deck profiles with different n and p combinations

$$b(x) = \frac{B}{2}\left[1 - \left(\frac{x}{L}\right)^{n}\right]^{p} \tag{2.7}$$

where, B is the breadth, L is the length overall and n and p are constants, with the same function as the aforementioned form factors. The difference between n – p and $m(x)$ – $q(x)$ is that the former marks the shape of the deck profile while the latter affects the cross sections only. Moreover, for every cross section x_i, a different set of $m(x_i)$ and $q(x_i)$ can exist. In fig. 2.7, the different main deck profiles as a result of the different combinations of n and p are illustrated.

Depth term: T(x)

The depth term marks the local distance from keel to deck. Thus, is a function that describes the keel profile, and it can be described by any mathematical expression that adjusts to the designer vision or idea. A great method is the use of Non-Uniform Rational Basis Spline (NURBS) curves, NURBS is a mathematical model very common in computer-aided design, capable of describing any shape or form provided that the corresponding input variables are the adequate. Thus, offers great design freedom and geometry adaptation. However, the more complex is the desired shape the more input parameters are necessary, thus using NURBS can have certain drawbacks, specially if there is a restriction in the number of input parameters. Nevertheless, keel profiles are generally simple hence, the amount of parameters necessary should be relatively low. Furthermore, other mathematical models can still be perfectly valid, such as the one explained in section 2.2.3.

2.2.1 Design space

The effect of the form factors over the resulting cross section are sketched in fig. 2.8, where the pair m–q are used as an example. Based on the form factor's influence, it can be assumed that m influences the upper portion of the curve while q influences the bottom, and both creates a hinging effect that can turn either clockwise or counterclockwise. Furthermore, the direction is established by the values of m and q by either being bigger than, lower than or equal to one. When $m > 1$ and $q > 1$ the curve hinges counterclockwise around their respective hinging point and vice versa. An illustrative table summarizing these trends can be found in fig. 2.9, where 9 different cases can be distinguished.

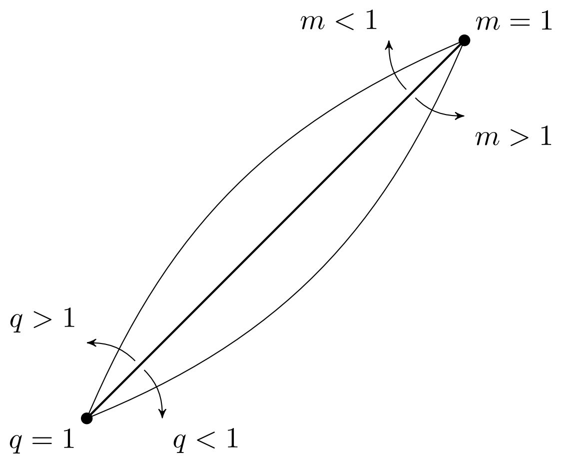

Figure 2.8: Schematic of the influence of the form factors over the resulting cross section depending on their value. The neutral position is when $m = 1$ and $q = 1$, which results in a straight line that would correspond to a V-hull type section.

As it can be appreciated, the central shape is a straight line corresponding to a wedge or V-hull type cross section, attained when $m = 1$ and $q = 1$, at this point the influence of the form factors can be considered to be neutral. When either of the form factors becomes different than 1, the resulting shape will be determined by the value of the non-unit form factor with a rotation direction according to the above explained. Furthermore, when both values are different than 1 the hinge effect can work constructively towards the same side —as in the top left and bottom right subplots— or hinge towards opposite directions —as depicted on the bottom left and top right subplots— resulting in a S-like shape.

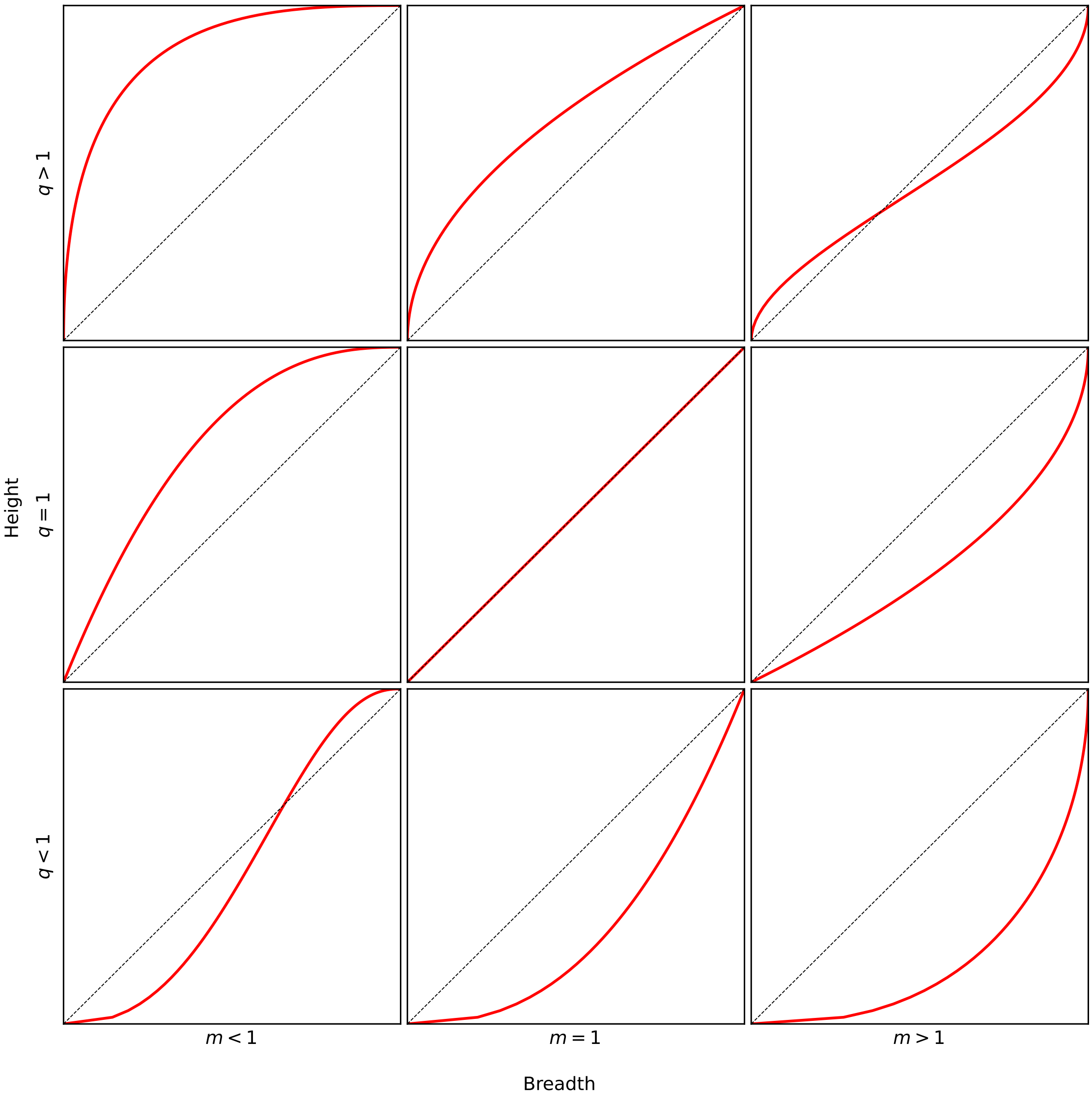

Figure 2.9: Representation of the different types of curves it can result depending on the m—q value combinations. Which are distinguished in $m, q > 1$, $m, q < 1$ and $m, q = 1$

2.2.2 Validation and limitations

In order to test the practicality of the new parametric expression, characteristic cross sections from different ship types are used to check whether it can be reproduced or not. As it can be appreciated in fig. 2.10, the bold black section is the objective and the red line is the approximation[4]made with the introduced concept. As it can be appreciated, for rounded hull shapes typical in sailing yachts, offshore cargo vessels or tugs (fig. 2.10a, fig. 2.10c and fig. 2.10j respectively) satisfactory results are achieved. However, for cross sections with kinks, typical in motor boats, the proposed model fails to reproduce it since hard chined sections cannot be reproduced with curves, as it can be appreciated in fig. 2.10e and fig. 2.10h. Furthermore, sections with special elements such as bulbs or full keels are also not possible to describe.

In summary, the model can reproduce a fairly broad range of rounded cross sections with satisfactory results. Where hull lines such as cargo or navy vessels and equivalents falls completely within the capabilities of the model. However, sections with kinks are completely out of the capabilities, where only a smooth version of the actual section, is the best approximation it can be achieved.

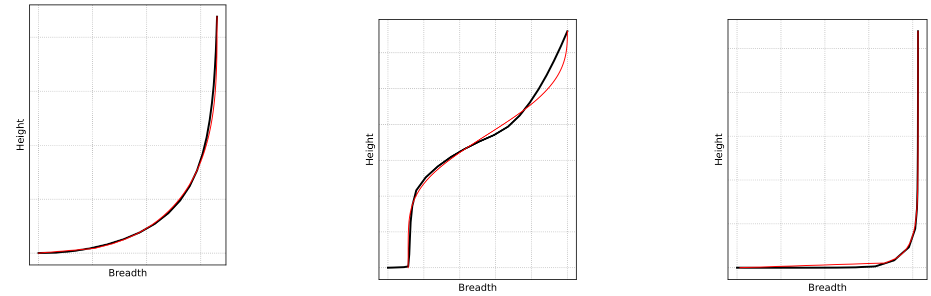

(a) Americas Cup sailing yacht cross section: $m = 3.25$ and $q = 0.42$

(b) Canoe cross section: $m = 2.784$ and $q = 6.64$

(c) Containership cross section: $m = 10.33$ and $q = 0.12$

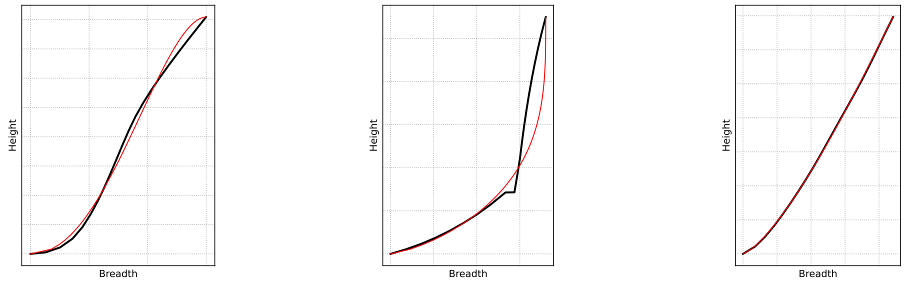

(d) Frigate cross section: $m = 0.52$ and $q = 0.47$

(e) Motor yacht cross section: $m = 3.27$ and $q = 0.75$

(f) Patrol vessel cross section: $m = 0.97$ and $q = 0.74$

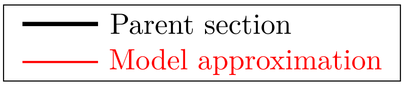

Figure 2.10: Part 1 of 2. Comparison between various characteristic cross sections from different vessel types, represented in bold black and their respective model by the modified Wigley hull expression.

---

[4] In order to ensure that all combinations of m—q are explored, a Genetic Algorithm (GA) based optimization code is applied. GA is a random-based global search algorithm, meaning it can explore a broad range m—q combinations and stick with the best fitting one. The application of optimization in the present context is not considered relevant for the thesis thus, no further developments will be made.

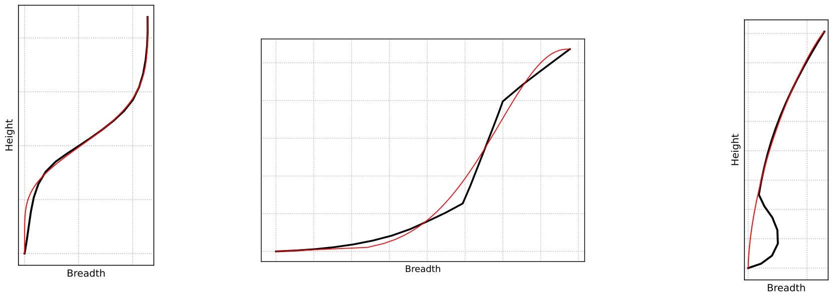

(g) Typical full-keel sailing yacht cross section: $m = 3.86$ and $q = 7.82$

(h) 14ft Skiff cross section: $m = 0.39$ and $q = 0.24$

(i) Trawler cross section: $m = 0.89$ and $q = 1.63$

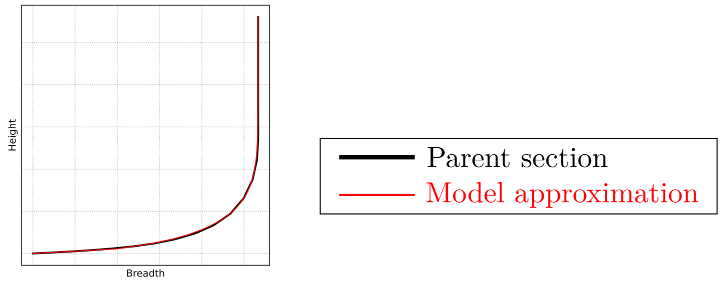

(j) Typical tug cross section: $m = 7.93$ and $q = 1.63$

Figure 2.10: Part 2 of 2. Comparison between various characteristic cross sections from different vessel types, represented in bold black and their respective model by the modified Wigley hull expression.

2.2.3 Adaptation for FASTSHIP

Because the main program of the thesis has certain geometry limitations, further described in chapter 3, an adaptation of eq. (2.5) is performed.

FASTSHIP can only work with simple hard chined hulls (with only one kink), which section can be described with 3 points, corresponding to the keel, chine and deck. The adaptation is realized by reducing the dimensions down to 2-dimension, however still representing a three dimensional shape, thus instead of modelling surfaces, curves are modelled. Furthermore, the chine and deck profiles are represented by two curves each, corresponding to the top and side view, while the keel is represented with one curve only, corresponding to the side view. See fig. 2.11 for an illustration of both views and the annotation used for the corresponding distances, for the equation shown below.

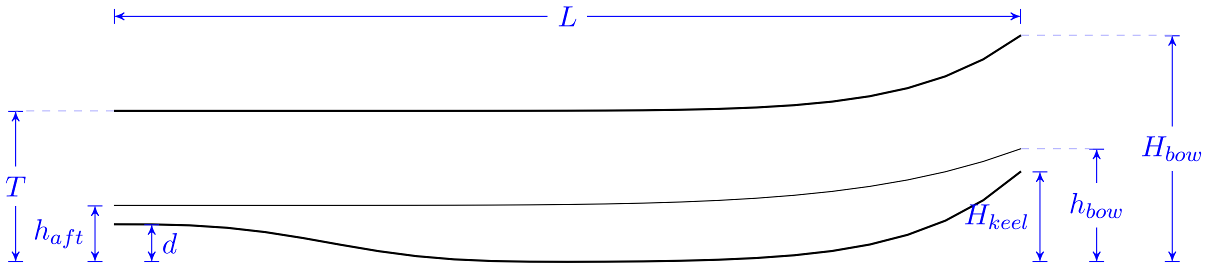

(a) Side view of the deck, chine and keel (from top to bottom) hull lines.

Figure 2.11: Part 1 of 2. Sketch showing the annotation of the distances involved for the use of FASTSHIP parametric hull

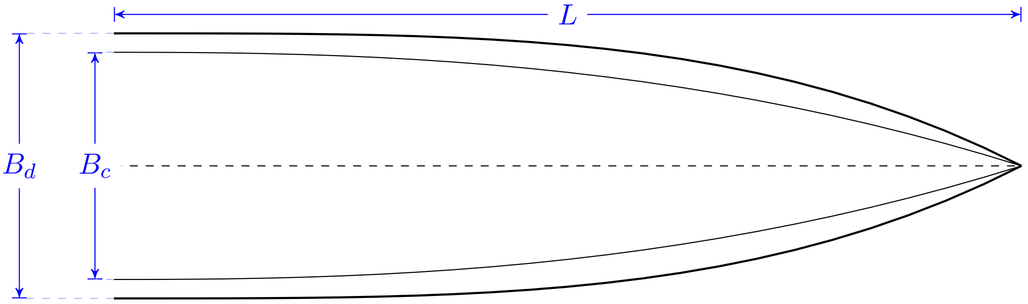

(b) Top view of the deck (thicker line) and chine hull lines

Figure 2.11: Part 2 of 2. Sketch showing the annotation of the distances involved for the use of FASTSHIP parametric hull

$$\begin{aligned}
&\text{Keel:} \quad z(x) = \left(\frac{x}{L}\right)^{m_{keel}} \cdot H_{keel} + d\exp\left(-\lambda\left(\frac{x}{L}\right)^{\alpha}\right)\\
&\text{Chine:} \quad \begin{cases} y(x) & = \frac{B_c}{2}\left[1-\left(\frac{x}{L}\right)^{n_{chine}}\right] \\ z(x) & = \left(\frac{x}{L}\right)^{m_{chine}}\left(h_{bow-h_{aft}}\right) + h_{aft} \end{cases}\\
&\text{Deck:} \quad \begin{cases} y(x) & = \frac{B_d}{2}\left[1-\left(\frac{x}{L}\right)^{n_{deck}}\right] \\ z(x) & = \left(\frac{x}{L}\right)^{m_{deck}}\left(H_{bow}-T\right) + T \end{cases}\\
&\text{where} \quad x \in [0, L]
\end{aligned} \tag{2.8}$$

The variables that takes part in the above equation are distances and form factors. The former are formed by 9 variables —L, B_d, B_c, T, H_{bow}, H_{keel}, h_{aft}, h_{bow} and d— illustrated in fig. 2.11, while the latter is the same concept as explained in section 2.2, formed by 5 variables —m_{keel}, m_{chine}, m_{deck}, n_{chine} and n_{deck}—. Two additional parameters determines the hull bottom clearance at the transom for the propulsion unit —λ and α—, which basically dictates the decaying rate of an exponential decaying function, seen in the last half of the keel function of eq. (2.8).

In total, 16 variables are involved in the parametrization of the hard chined hull model. However, it can already be advanced that due to the constraints mentioned in section 1.4, the parameters that influences the length, the deck profile and the maximum propulsion clearance —L, T, H_{bow}, d and m_{deck}— will be kept fix, reducing the variables to 11. Further analysis of the input space of the parametric model is performed in section 4.1.

2.3 Reproducing the *NINA*

The demihull of *Nina* is modelled using the explained parametric hull model, where the form factors are fine tuned in order to reproduce the cross sections at discrete points x_i along the hull's length. In fig. 2.13, three random cross sections from the *Nina* are selected, in order to illustrate the approximation accuracy of the method. By connecting the resulting $m(x_i)$ and $q(x_i)$ discrete points, the form factor functions $m(x)$ and $q(x)$ can be obtained, depicted in fig. 2.12a and fig. 2.12b respectively. The chosen methodology to connect the points is the NURBS curve, due to its great interpolating features enabling the conversion of discrete points into a continuous curve. Nonetheless, any other interpolating method could also be used.

Modifying the profile of $m(x)$ and $q(x)$ will result in a different hull shape, thus enabling the exploration of different hull designs. Applying this functions into eq. (2.5) results in the parametric approximation depicted in fig. 2.14.

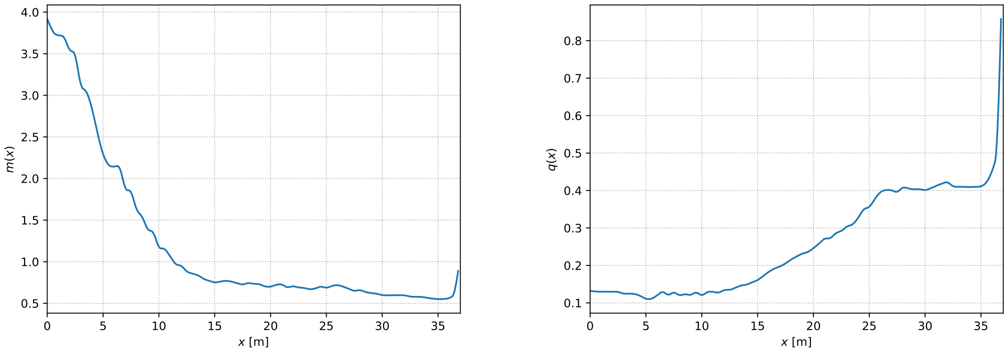

(a) Evolution of the form factor m values along the hull length that reproduces *Nina*

(b) Evolution of the form factor q values along the hull length that reproduces *Nina*

Figure 2.12: NURBS curve of $m(x)$ (left) and $q(x)$ (right)

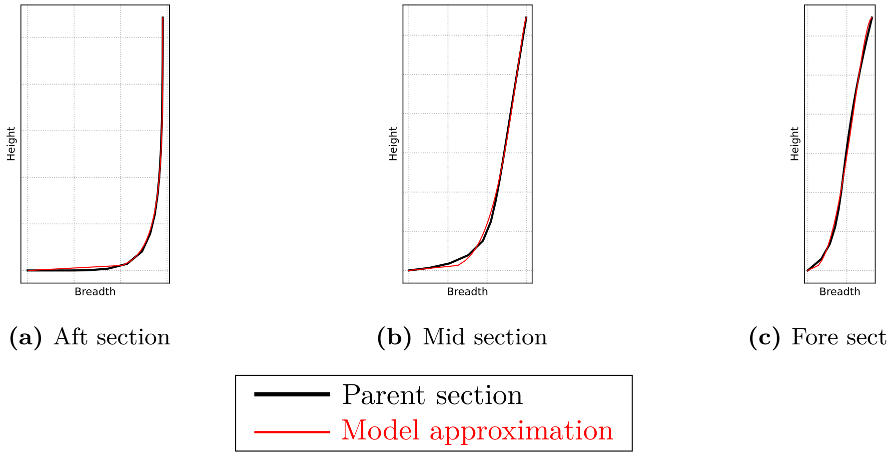
(a) Aft section

(b) Mid section

(c) Fore section

Figure 2.13: Three random sections from three different locations of *Nina's* demihull are displayed for comparison between the parent section and its approximation

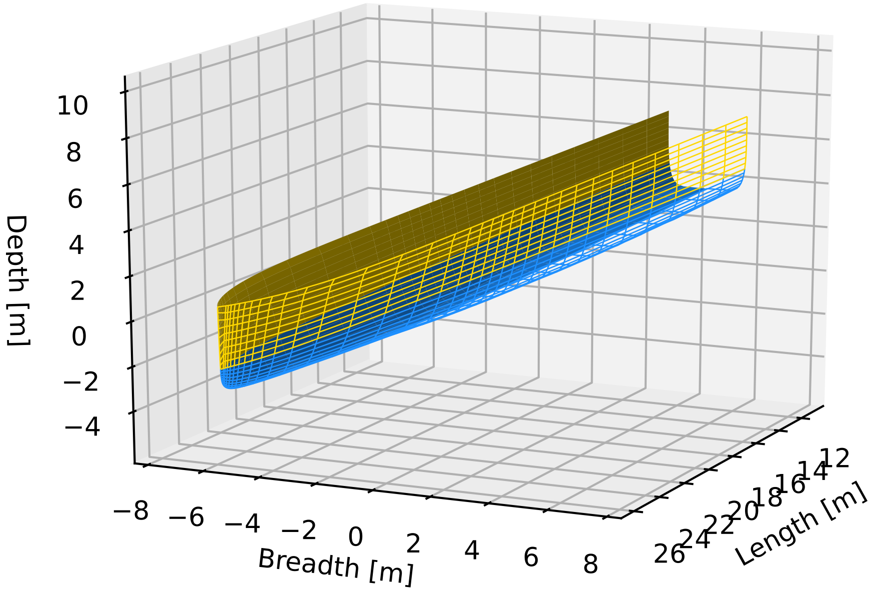

Figure 2.14: Parametric hull version of *Nina*

3

Numerical Analysis

Numerical tools are a very convenient way to explore the particularities of a problem at a relatively low cost, especially at the initial stage of a project. In the case of wet deck slamming, capturing the motions of the catamaran sailing in an irregular sea is of the utmost importance, since the interaction between the hull and the waves is what leads to potential slamming. As outlined by *J. A. Keuning* [11], high speed crafts sailing in irregular seas often have an uneven underwater geometry along the length that changes over time, which results in non-linear upright forces leading to non-linear motions. Therefore, in order to capture them, a non-linear mathematical model needs to be used. Non-linear models are generally captured in the time-domain.

As outlined in section 1.4, only head waves sailing conditions will be considered, hence, the motions of a FFC sailing can be reduced to surge, heave and pitch. Furthermore, since changes in the forward velocity are assumed to be considerably small compared to the actual forward speed, surge can be neglected.
The consideration of head waves allows for the simplification of the hull geometry as well, where the seakeeping analysis of FFCs can be simplified to its demihulls. Such simplification will treat the geometry as a 'conceptual demihull', because on practice, a monohull will be evaluated in the seakeeping program. However, during post-processing the main deck of the monohull will correspond to the wet deck of the demihull.

The program to carry on such purpose will be FASTSHIP, a strip theory-based numerical model for high speed crafts sailing in irregular head waves.
It is important to mention that FASTSHIP only supports hard chined hulls, and the hull is meshed by frames which can only be described with 3 points, obviously narrowing the hull design exploration to only hard chined hulls. However, being FASTSHIP a highly convenient solver with relatively inexpensive simulations, a special consideration has been given. In fig. 3.1, the RAO of heave and pitch between different experimental data of similar FFCs sailing in irregular head waves are compared with FASTSHIP. The models are part of Damen's FFC catalogue, and the corresponding experimental data provided by Damen as well. Within the selected catamarans, a hard chined-type known as the 4212 (see fig. 3.2) is used as a "test hull" for FASTSHIP. The rest of the considered FFCs are namely, the DFFe 3810 and the DFFe 5215, catamarans of 38 m and 52 m length respectively. In order to compare the RAO performances, the various experimental data

are scaled to the same length as the 4212 by means of the Froude Correlation Law[5],

$$\frac{V_s}{\sqrt{L_s}} = \frac{V_m}{\sqrt{L_m}} \tag{3.1}$$

in order to evaluate FASTSHIP level of accuracy. The comparison allows to create a context or rather, an orientative operational range, in which FASTSHIP is able to fall within the same window. As it can be appreciated, the heave RAO (fig. 3.1a) tends to be slightly overpredicted, while the pitch RAO (fig. 3.1b) is slightly more centred amongst the data.

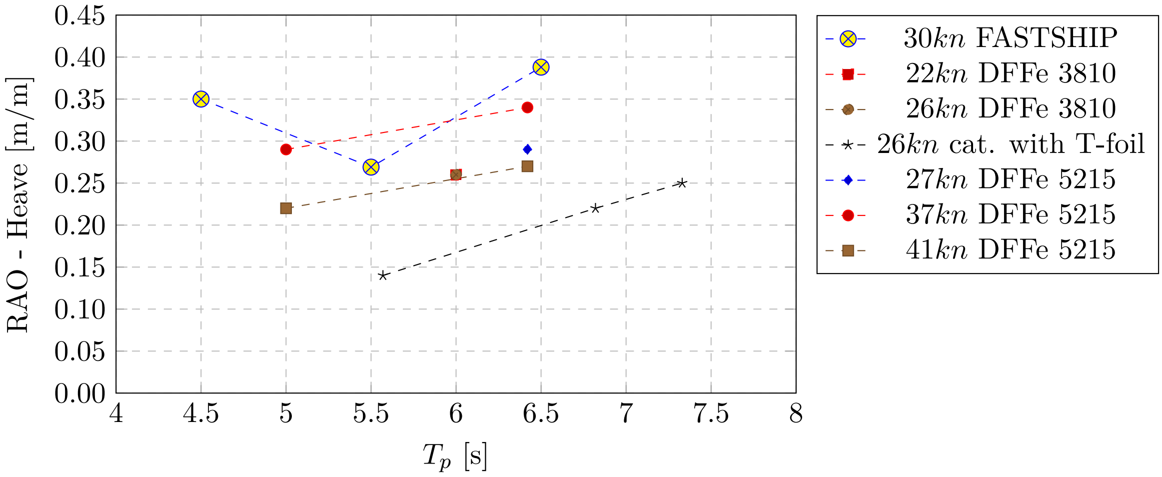

(a) RMS Heave / Significant wave height

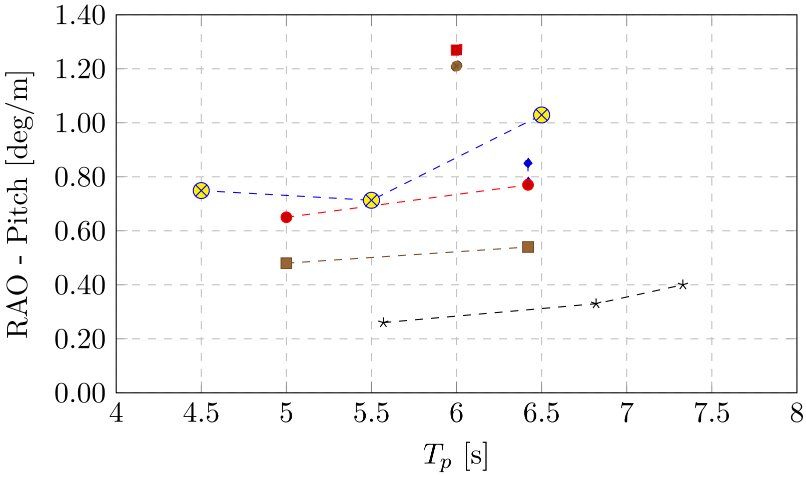

(b) RMS Pitch / Significant wave height

Figure 3.1: RAO comparison of the heave and pitch amongst experimental data of different catamaran and FASTSHIP results. The RAOs are computed as the ratio between the RMS of the corresponding motion and the significant wave height. The data are provided by Damen.

Overall, it is considered that FASTSHIP is a valuable tool for an orientative assessment of monohull seakeeping performance at the initial stages of a project. Furthermore, as

---

[5] Froude Correlation Law: eq. (3.1) for equal wave patterns of similar hull geometries. Subscript “s” denotes the ship full scale and “m” denotes model scale. The involved parameters are the velocity V and length L.

explained by *A.F.J. van Deyzen* [25] and *J. A. Keuning* [11], the overall magnitudes of the responses are not accurately predicted within FASTSHIP, given the simplifications applied in its mathematical model. However, the trend responses were fairly well predicted and the non-linear behaviors are successfully captured. Therefore, it is deemed accurate enough for the present work, specially considering the amount of simulations necessary for the DOE methods explained in chapter 4.

Figure 3.2: Damen 42 m FFC.

In the present chapter, first, a numerical approach to model wet deck slamming is proposed, detailed in section 3.1. Secondly, the program FASTSHIP is described in detail in section 3.2, where a sensitivity analysis is performed in order to ensure the simulations consistency and output robustness. Finally, the corresponding results are discussed.

3.1 Modelling wet deck slamming

From the literature review (section 1.2), it is inferred that the great majority of the research that used numerical approaches, focused on the structural response, where quite satisfactory results were achieved. The used methods were able to predict the slamming magnitudes fairly accurately. However, relatively expensive solvers were required. Albeit the studies focused only on single wet deck slamming events (mainly free fall tests), it leads to think that performing the same studies with longer fluid interactions or furthermore, with more than one wave interaction, is currently not worth the effort, mainly because of the exponential increase in computational cost. Therefore, a trade-off between the slamming magnitude accuracy and the simulation time exists. The present research gives more weight to the latter, because wet deck slamming is considered to be an intrinsically recurrent phenomenon that needs to be evaluated over multiple occurrences rather than just one single slamming encounter. Thus, wet deck slamming will be measured from a statistical point of view.

The approach of assessing slamming from a statistical perspective, takes one step back from the common approach, above explained, and addresses it as the potential chance of wet deck slamming. Prediction details are sacrificed in the wake of stretching the (slamming) evaluation for longer durations, thus singular slammings will not be accurately predicted, but will still assess the overall seakeeping performance of the FFC in regards of it. Furthermore, the simplicity of the approach allows for a fast and straightforward wet deck slamming evaluation, thus reducing the computational load and complexity. Moreover, calculations can be realised in the post-processing phase.

Since the seakeeping simulation of a FFC is reduced to the analysis of a monohull considered as a demihull, no wet deck is considered in the geometry definition. Thus, wet deck exceedance is computed at a conceptual level by considering the monohull's main deck as the demihull's wet deck, illustrated with a thick bold line in the following figures. Whenever the free surface passes through the wet deck profile, an exceedance is counted and a potential wet deck slam is identified.

The wet deck exceedance is computed in time and space by keeping track of the relative wet deck clearance $d(x, z, t)$ throughout the entire length. As depicted in fig. 3.3, wet deck clearance is the difference between the absolute coordinates of any point contained in the wet deck and the local free surface height at the same longitudinal position, at a given time t.

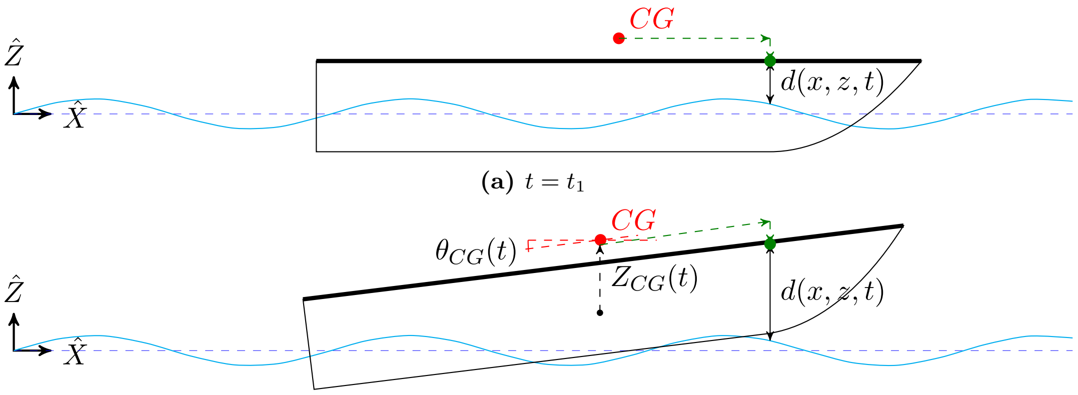

(a) $t = t_1$

(b) $t = t_2$

Figure 3.3: Schematic of the relative wet deck clearance evaluation along two different time steps.

By considering the heave $Z_{CG}(t)$ and pitch $\theta_{CG}(t)$ timetraces, defined with respect to the vessel's center of gravity (CG) the absolute coordinates of any point contained in the wet deck (X_{WD}, Z_{WD}) can be computed, by means of the rotation matrix

$$\begin{pmatrix} X_{WD} \\ Z_{WD} \end{pmatrix} = \begin{bmatrix} \cos\theta_{CG}(t) & -\sin\theta_{CG}(t) \\ \sin\theta_{CG}(t) & \cos\theta_{CG}(t) \end{bmatrix} \cdot \begin{pmatrix} x \\ z \end{pmatrix} + \begin{pmatrix} 0 \\ Z_{CG}(t) \end{pmatrix}$$

where x and z are coordinates contained within the wet deck, thus $x \in [0, L]$ and $z \in [Z_{WD}(x = 0), Z_{WD}(x = L)]$. Therefore, the deck clearance can be computed as

$$d(x, z, t) = Z_{WD} - \eta(x, t) \tag{3.2}$$

where $\eta(x, t)$ is the wave elevation timetrace. Both terms in eq. (3.2) are formulated with respect to the absolute frame of reference, positioned at calm water level.

Plotting the timetrace of the deck clearance, for instance, at the position marked with a green dot in fig. 3.3, would result in a signal such as fig. 3.4. Where positive values means the local wet deck is dry and negative values means it is wet.

Furthermore, the derivative of the deck clearance timetrace $d(x, z, t)$ shall yield the relative deck clearance velocity. Filtering out the dry moments and keeping only the wet

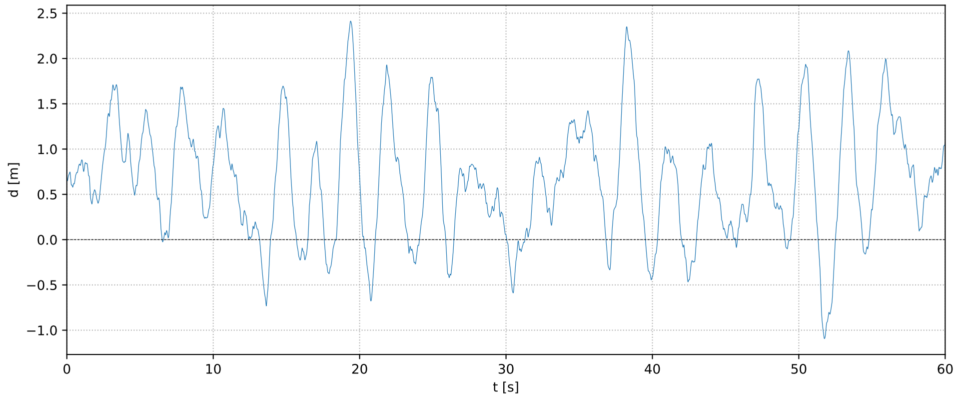

Figure 3.4: Example of a deck clearance timetrace at a particular location.

ones will result in a timetrace such as fig. 3.5. The positive values corresponds to the first part of the wetting instants, where the free surface would actively push against the local wet deck. The negative values correspond to the second part of the wetting instants, where both objects are moving away from each other. The relevant instants occur at the positive side of the signal, because these are the instants where the relative directional vector of the free surface points upwards, against the wet deck.

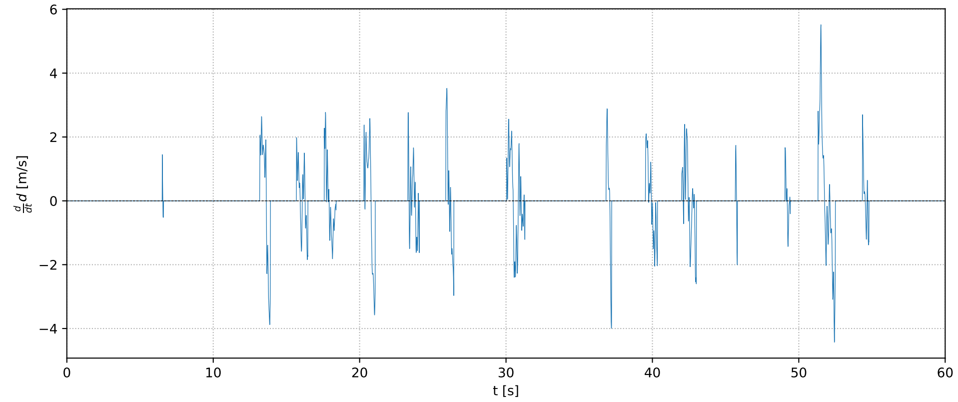

Figure 3.5: Example of a relative wave exceedance velocity timetrace at a particular location.

The above example only analyses the wet deck exceedance at one particular point. However, as depicted in 3.6, the exceedance is continuous and happens over a finite length. Furthermore, it actively changes throughout time, so that more than one location along the wet deck can be exceeded simultaneously.

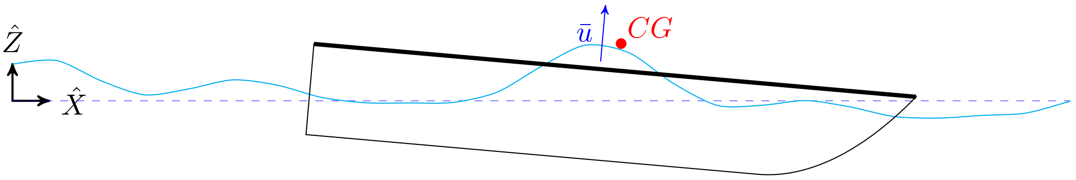

Figure 3.6: Schematic of a FFC viewed from the side sailing in irregular waves. The free surface has exceeded the wet deck, highlighted with a thick bold line.

Therefore, the use of the impulse formulation is introduced. Impulse (J), is defined as the integral of force (F) over time

$$J = \int F dt \tag{3.3}$$

and force is a vectorial quantity integrated over space. Hence, using the impulse formulation allows for quantifying the interaction between the free surface and the wet deck in both time and space into a representative value. Which can be used to compare with other hulls, and the hull that yields an overall lower impulse quantity shall translate into a lower potential slamming, thus, yielding a better seakeeping performance.
Such impulse is computed by actively monitoring the force, as depicted in fig. 3.7, resulting in a timetrace. The details for modelling the force and the subsequent impulse will be further explained below.

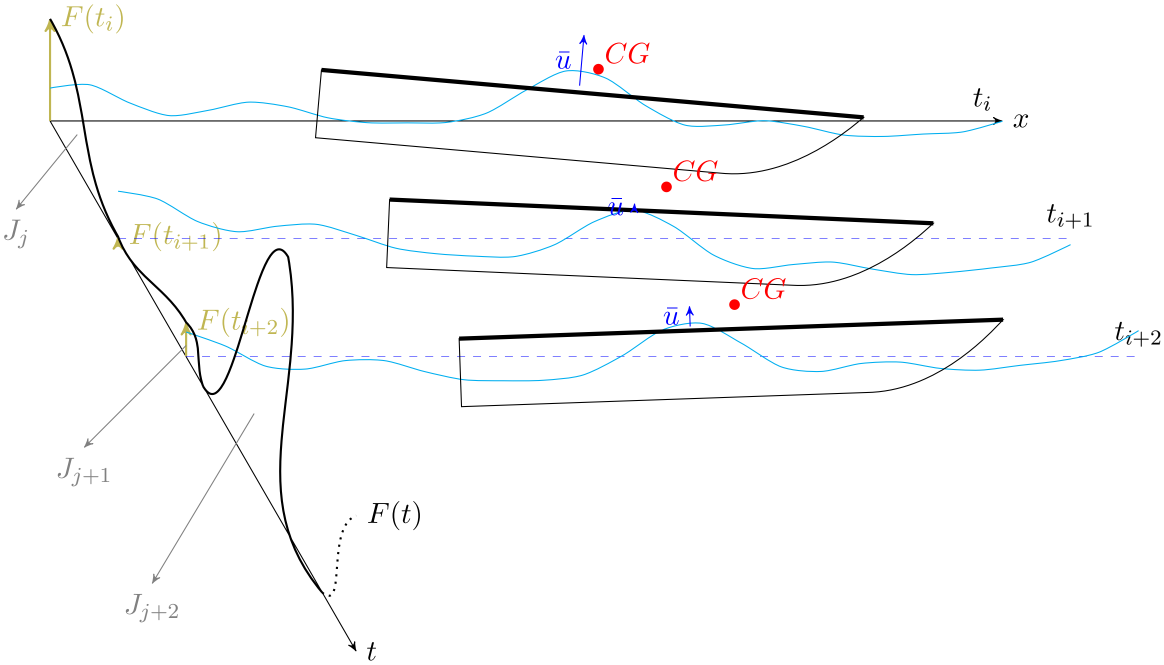

Figure 3.7: Schematic of the procedure to calculate the impulse. The wet deck exceedance and the relative velocity of exceedance is measured in order to compute the force at every time step. Resulting in a force timetrace $F(t)$, that can finally be integrated over each peak width, yielding the impulses.

The force is modelled as the rate of change of momentum of the fluid passing through the wet deck with an upward vertical velocity v. The velocity v is obtained from the interaction between the free surface and the wet deck as above explained (illustrated in fig. 3.5), which does not obey the Dirichlet boundary condition (no penetration) since the free surface is free to pass through the wet deck. Such counter-physical behaviour is accepted and considered as a modelling assumption. Thus,

$$v = \left\{ \frac{d}{dt} d(x, z, t) \in \mathbb{R} \quad | \quad \frac{d}{dt} d(x, z, t) > 0 \right\} \tag{3.4}$$

Since the problem is 2-dimensional, the wet deck is normalised to a unit width. Thus, the final integral form of the force, derived below, can be expressed as function of the longitudinal variable x.

$$
\begin{aligned}
F &= \frac{d}{dt}(mv) \\
&= \dot{m}v \\
&= \int_A \rho(\bar{u}\cdot\hat{n})v dA \\
&= \int \rho v^2 dx
\end{aligned}
\tag{3.5}
$$

Where $\bar{u}\cdot\hat{n}$ is the normal component of the fluid velocity relative to the local wet deck. Substituting the above expression into eq. (3.3) yields the final form of impulse.

$$
J = \int_{t_{wet}} \int_{x_{wet}} \rho v^2 dx dt \qquad \forall \quad dx \in x_{wet} \quad \text{and} \quad dt \in t_{wet} \tag{3.6}
$$

It should be clarified that the above expression is applied only at the moments of wet deck exceedance with positive realtive deck clearance velocity. Meaning, the integral over the differential space dx is only applied at the wetted areas contained in the wetted domain denoted as x_{wet} and the integral over the differential time dt is applied only at the wetted periods contained in the wetted domain denoted as t_{wet}, both existing in the positive relative deck clearance velocity instants, $v > 0$.
Moreover, as depicted in fig. 3.7, there can be many wetted periods, leading to many impulses.

In summary, in order to capture the interaction between the free surface and wet deck along a given sailing period, use is made of the impulse formulation as a mean to encapsulate such interaction into a significant quantity. Where the modelling assumption of using the relative deck clearance velocity (eq. (3.4)), during the wet-wet deck moments as the impact velocity is adopted.

3.2 FASTSHIP

FASTSHIP is a strip theory-based program that is able to model non-linear motions of high speed crafts sailing in irregular head waves. The use of strip theory allows to simplify a 3-dimensional hydrodynamical problem to two coupled 2-dimensional models, defined from two different perspectives, side view (like in fig. 3.9) and front view (like in fig. 3.10). Using the Wagner analytical formulation of a wedge penetrating a fluid surface as its basis in combination with an empirical approach for the hydrodynamic coefficients involved, it covers the necessary ingredients for describing the main physical phenomena of planing hulls. These phenomena are bounded together by the equation of motions.
In order to capture the non-linear effects, the model is written in the time domain where the sinkage, wetted length and trim are updated at every time step.

The original model started with *E. E. Zarnick* (1978) [27], later *J. A. Keuning* (1994) [11] relayed the work and further explored the concept. On 2009 the work was again further improved by *A.F.J. van Deyzen* [25]. Although there are more updated versions of FASTSHIP, for the present work the version from *A.F.J. van Deyzen* is used[6].

The FASTSHIP 2009 version features the simulation of 3 degrees of freedom, — surge, heave and pitch — and the possibility to define a constant thrust, in addition to the already constant forward speed feature. FASTSHIP only supports hulls with V-bottom sections

---

[6] Due to burocratic reasons, only the FASTSHIP version from 2009 was accessible for the present research.

because the majority of the high speed crafts are, if not practically, very close to hard chined hull types. Its original intention was to create a platform that would allow for a "fast" insight into the seakeeping behaviour of such ships during the early stages of design.

Since FASTSHIP can only work with hard chined monohulls, the afore-introduced catamaran 4212 (fig. 3.2) demihull will be used as "test hull" for the design exploration whenever FASTSHIP is involved in the research.
In fig. 3.8, the geometry of the 4212 demihull for FASTSHIP is shown.

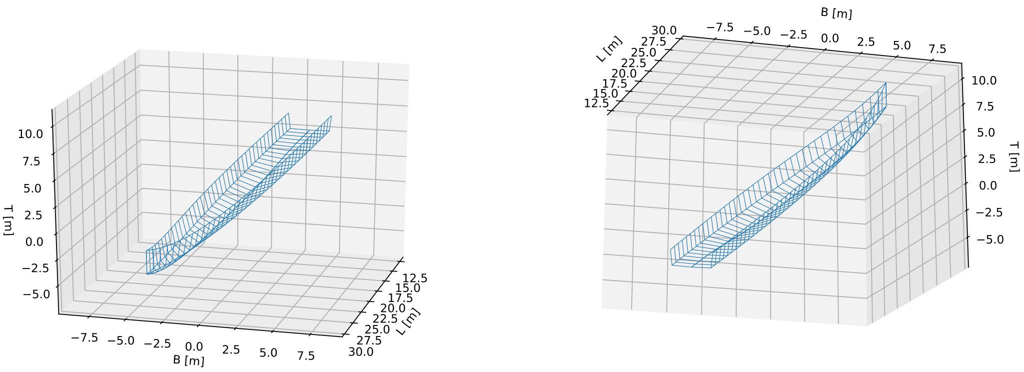

(a) Bird view **(b)** Fish view

Figure 3.8: 4212 demihull modelled according to FASTSHIP specifications.

3.2.1 Mathematical model

The mathematical model of FASTSHIP is build upon the equation of motion, where the main forces are defined as depicted in fig. 3.9. These forces are, thrust T, drag D and fluid dynamic forces, the latter differentiated into hydrostatic F_{sta} and hydrodynamic F_{dyn} forces.

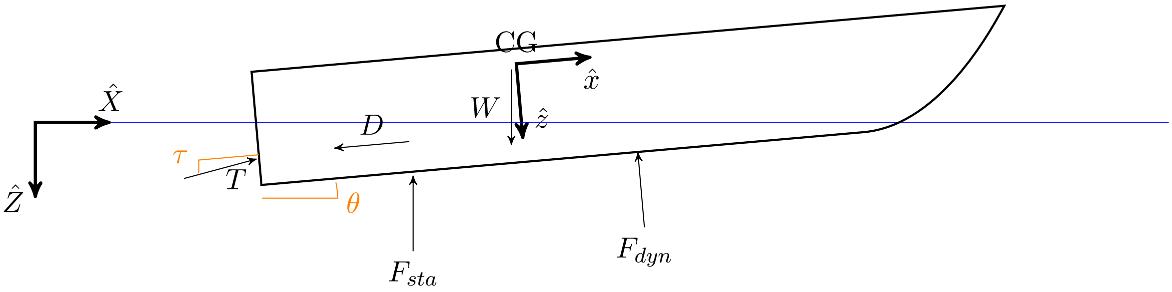

Figure 3.9: Schematic of the hull forces at longitudinal view.

As it can be appreciated, there are 2 frames of reference, an earth fixed ($\bar{X}$) and a body fixed ($\bar{x}$) frame of reference. On both, relative to their systems, the horizontal positive direction points to the direction that the vessel is heading whereas the vertical positive direction points downwards.

In order to account for the changes of the underwater geometry of the hull while sailing, the aforementioned forces are evaluated per strip, in the $\bar{x}$ reference. Where each strip is treated as a wedge water entry problem dropping at a velocity V as depicted in fig. 3.10. Furthermore, the water deformation known as water the pile-up effect at both sides of the waterline is accounted analytically based on Wagner's approach, which will be detailed further below.

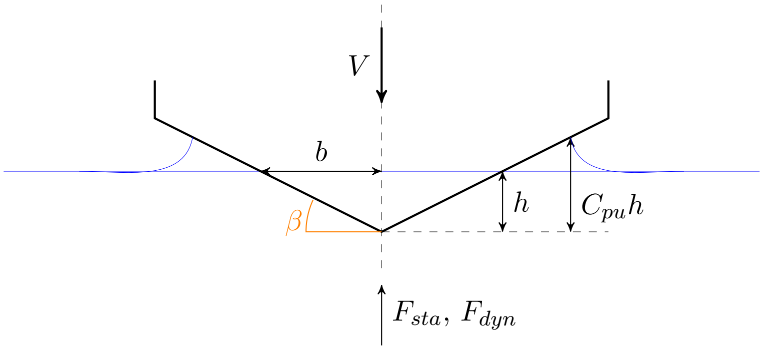

Figure 3.10: Schematics of the cross sectional hull forces.

The main assumptions which FASTSHIP model is built upon are namely:

- There is no interaction of forces between strips. Meaning, the flow around the hull is assumed to be such that discretizing it into strips does not have any remarkable negative impact on its continuity along the ship length.
- The flow is assumed to be quasi-steady, so performing a force equilibrium at every time step is appropriate.
- The waves dimensions are assumed to be larger than the hull dimensions. And the wave slope is assumed to be relatively smaller. Therefore, diffraction forces are negligible and only Froude-Krilov forces are relevant.
- The horizontal wave orbital velocity component is considered to be very small compared to the ship speed. Therefore, its impact on the ships motions is considered negligible.

- Planing mode of approximately $Fn_\nabla \geq 1.5$ is assumed, thus wave making resistance and viscous-induced pressure resistance are neglected from the resistance analytical model.

Next, the main concepts and components of the mathematical model are introduced.

3.2.1.1 Basic equations of motion

The general form of the equations of motion is

$$\begin{cases} M\ddot{X}_{CG} &= T\cos(\theta+\tau) - F_{dyn}\sin(\theta) - D\cos(\theta) \\ M\ddot{Z}_{CG} &= -T\sin(\theta+\tau) - F_{dyn}\cos(\theta) - F_{sta}\cos(\theta) + D\sin(\theta) + W \\ I\ddot{\theta} &= Tl_T + F_{dyn}l_{dyn} + F_{sta}l_{sta} - Dl_D \end{cases} \tag{3.7}$$

Where:

M: Mass of ship

W: Weight of the ship

I: Pitch moment of inertia

θ: Pitch angle

τ: Propulsor shaft's angle

$\ddot{X}_{CG}$: Acceleration of CG in x direction.

$\ddot{Z}_{CG}$: Acceleration of CG in z direction.

l_T, l_{dyn}, l_{sta}, l_D: lever arms of T, F_{dyn}, F_{sta} and D with respect to CG, respectively.

As aforementioned, the main forces in eq. (3.7) will be discretised into strips and further derived according to the wedge water entry problem. Integrating these forces along the length and assembling them back into eq. (3.7) will yield the actual equation of motion.

3.2.1.2 Force breakdown

The main forces to consider are explained next.

Drag

The drag is computed as

$$D = \frac{1}{2} C_F \rho U^2 A_w \tag{3.8}$$

Where U is the flow velocity parallel to the keel modelled as $U = \dot{X}_{CG}\cos(\theta) - \dot{Z}_{CG}\sin(\theta)$. In this expression the orbital velocity influence is omitted as it is considered negligible.
The friction coefficient C_F is obtained by means of the ITTC formula, with the particularity that the Reynolds number is updated at each time step by computing the mean of the wetted keel and wetted chine lengths, L_m.

$$\begin{aligned} L_m &= \frac{L_k + L_c}{2} \\ R_n &= \frac{U L_m}{\nu} \\ C_F &= \frac{0.075}{(log(R_n) - 2)^2} \end{aligned} \tag{3.9}$$

Hydrostatic force

The hydrostatic force is computed by identifying the volume underwater of each strip. However, at planing regime an under-pressure surrounding the hull arises, resulting in a lower effective hydrostatic force. Therefore, the buoyancy is corrected with the buoyancy correction factor a_{bf} and a_{bm} for the transversal and longitudinal planes respectively, both determined empirically. The latter is mainly meant for the righting moment correction of the pitch motion.

$$\begin{aligned} f_b &= a_{bf} \rho g A \\ a_{bf} &\in [0, 1] \end{aligned} \tag{3.10}$$

Hydrodynamic force

The hydrodynamic forces accounted in the model are reduced to a pressure and viscous-based source of resistance, f_{fm} and f_{cdf} respectively. *E.E. Zarnick* [27] modelled f_{fm} as the rate of change of momentum in terms of added mass of the flow under the cross section considered. That was both maintained by *J. A. Keuning* [11] and *A.F.J. van Deyzen* [25].

Therefore, a total derivative is applied to the momentum, which is expressed in terms of the added mass.

$$f_{fm} = \frac{D}{Dt}(m_a V) \tag{3.11}$$

For the modelling of the added mass m_a, two cases are distinguished, the dry chine and wet chine mode. The main difference between the two lies into the water pile-up effect, represented by the pile up factor C_{pu} as depicted in fig. 3.10.
Generally, the aft-most strips are the ones submerged beyond the chine, whereas close to the flow stagnation point the chines tend to be dry(er).

Therefore, the added mass expression will vary depending on the mode considered. The general form of m_a (for the present approach) is the Wagner formulation, as shown next, along with its time derivative.

$$\begin{aligned} m_a &= C_m \frac{\pi}{2} \rho b^2 \\ \frac{dm_a}{dt} &= C_m \pi \rho b \frac{db}{dt} \end{aligned} \tag{3.12}$$

Where C_m is the added mass coefficient, determined empirically. Upon the general expression, differentiation is made based on how the local breadth changes as the cross section sinks, which can either be:

- **Dry chine**
  In this case the breadth depends on the instantaneous draught h.

$$b = h \cdot \cot(\beta) \tag{3.13}$$

- **Wetted chine**
  In this case the water pile up factor C_{pu} is introduced, depicted in fig. 3.10. The application of this factor follows from *P.R. Payne* [18, 19, 20], who realized that using Wagner's pile up factor of $\pi/2$ resulted in too high impact loads compared to analogous experimental values, and thus added a dead rise angle dependency that improved the accuracy.

$$\begin{aligned} b &= C_{pu} h \cdot \cot(\beta) \\ C_{pu} &= \frac{\pi}{2} - \beta \left(1 - \frac{2}{\pi}\right) \end{aligned} \tag{3.14}$$

Finally, the cross flow drag force is formulated as follows, where $C_{D,c}$ is the cross flow drag coefficient, determined empirically.

$$f_{cdf} = C_{D,c} \cos(\beta) \rho b V^2 \tag{3.15}$$

Combining eq. (3.11) and eq. (3.15) together yields the hydrodynamic force.

$$f_{dyn} = f_{fm} + f_{cfd} \tag{3.16}$$

Transom flow correction

At planing speeds, transom ventilation starts to occur which translates to an underpressure on the transom area. Furthermore, flat transom crafts at sufficient speeds will even achieve dry transoms. In order to simulate such phenomenon, a transom flow correction is applied that forces the longitudinal pressure profile along the hull to decay as evaluation gets closer to the transom, until it is completely zero at the transom, as depicted in fig. 3.11.

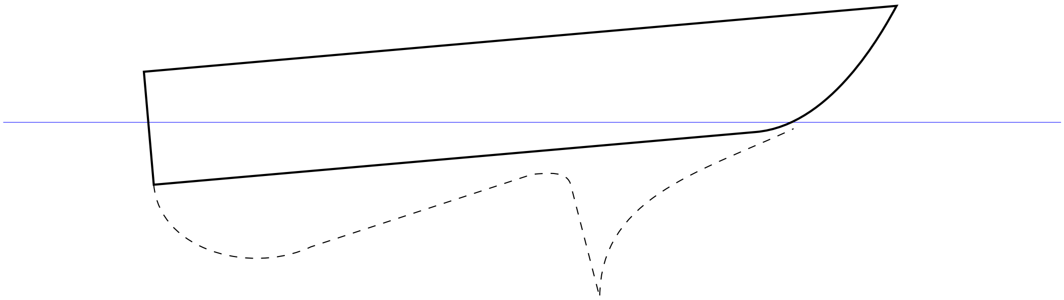

Figure 3.11: Schematic of the longitudinal lift profile correction.

The shape function that forces the computed forces to follow the above profile is

$$C_{tr}(x) = \tanh\left(\frac{2.5}{a}(x - x_{TR})\right) \tag{3.17}$$

where a is a reduction length and x_{TR} is the longitudinal transom coordinate. The determination of a is achieved by a non-dimensional analysis approach done by *K. Garme* (2004) [8], who determined a value for the non-dimensional reduction length $\tilde{a}$ by means of a systematic model experiment.

3.2.1.3 Final equations of motion

The integral forms of the above-introduced forces along the 3 main degrees of freedom are

$$\begin{aligned}
F_x &= -\int_L C_{tr} f_{dyn} \sin(\theta) dx \\
F_z &= -\int_L C_{tr} f_{dyn} \cos(\theta) dx - \int_L C_{tr} f_b dx \\
F_\theta &= \int_L C_{tr} f_{dyn} x dx + \int_L C_{tr} f_b \cos(\theta) x dx
\end{aligned} \tag{3.18}$$

By properly developing the integrals along with the full term of its components and assembling them back in to eq. (3.7), a linear system of equations is obtained, which can be expressed as

$$\begin{gathered}
\begin{bmatrix} M + M_a \sin^2(\theta) & M_a \sin(\theta)\cos(\theta) & -Q_a \sin(\theta) \\ M_a \sin(\theta)\cos(\theta) & M + M_a \cos^2(\theta) & -Q_a \cos(\theta) \\ -Q_a \sin(\theta) & -Q_a \cos(\theta) & I + I_a \end{bmatrix} \cdot \begin{pmatrix} \ddot{X}_{CG} \\ \ddot{Z}_{CG} \\ \ddot{\theta} \end{pmatrix} = \begin{pmatrix} T\cos(\theta + \tau) + F'_x - D\cos(\theta) \\ -T\sin(\theta + \tau) + F'_z + D\sin(\theta) + W \\ Tl_T + F'_\theta - Dl_D \end{pmatrix} \\
\bar{\bar{M}} \cdot \ddot{\bar{X}} = \bar{F}
\end{gathered} \tag{3.19}$$

where

$$\begin{aligned}
M_a &= \int_L C_{tr} m_a dx \\
Q_a &= \int_L C_{tr} m_a x dx
\end{aligned}$$

To solve eq. (3.19), a Runge-Merson iteration scheme is applied in order to solve for the accelarations.

$$\ddot{\bar{X}} = \bar{\bar{M}}^{-1} \cdot \bar{F} \tag{3.20}$$

The full derivation of the mathematical model can be found in Appendix A.1

3.2.2 Program setup

FASTSHIP setup is no different than any standard CFD programs. A flow chart summarizing the various steps involved in the simulation is displayed in fig. 3.12.

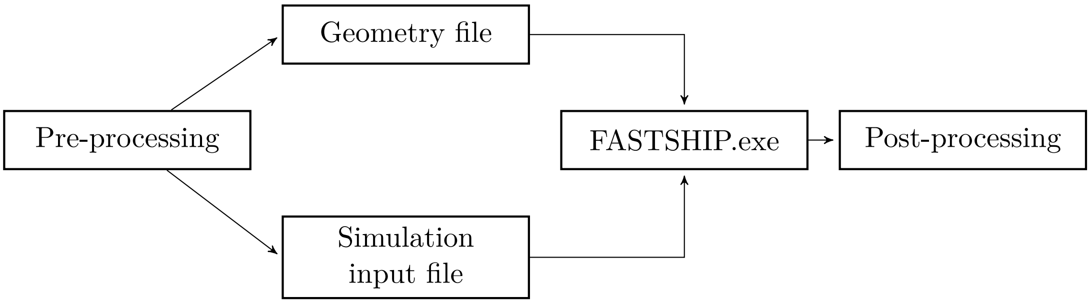

Figure 3.12: Flow chart of FATSHIP setup.

In order to ensure consistency between the simulations a sensibility study on FASTSHIP parameters is performed (namely, on the number of sections that describes the hull, the simulation duration, and the wave parameters). The analysis is differentiated in two parts, geometry analysis and wave analysis, shown next. The main response parameter used for the analysis will be the number of wet deck exceedances along the wet deck length. Identifying the wet deck exceedances is the first step in the modelling of impulse to assess slamming, explained in section 3.1, thus there is less post-processing involved in such quantity, allowing for a better assessment.

3.2.2.1 Geometry analysis

The geometry description in FASTSHIP is realised by (transversal) frames, and each frame is described with 3 coordinates namely the keel, chine and deck, see fig. 3.8. In order to ensure result independence from the mesh, various mesh sizes were tested, namely 20, 40, 60, 80, 100 and 120 sections. The heave and pitch RAOs were compared along with the number of wet deck exceedances in an irregular wave with a Jonswap spectrum in the winter conditions (see table 1.2).

Based on the RAO data displayed in fig. 3.13, no significant influence by the mesh size can be appreciated. Nevertheless, small discrepancies exist in the low frequencies, where convergence starts at 80 sections. The differences among 80, 100 and 120 sections are minimal. Hence, it is deemed counterproductive to increase the number of sections any further, as it would just increase the computational time for a marginal increase in accuracy. The same is inferred from the wet deck exceedance along the hull length. See fig. 3.14.

Therefore, the standard mesh of 80 stations will be considered for the rest of the study.

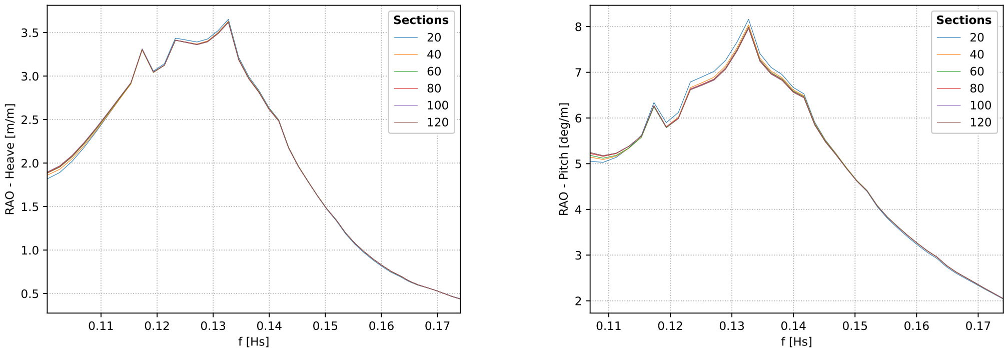

(a) Heave **(b)** Pitch

Figure 3.13: RAO comparison of different mesh sizes.

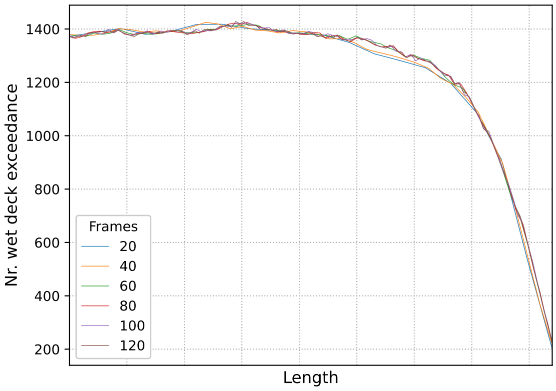

Figure 3.14: Wet deck exceedance distribution along the length comparison of different mesh sizes for a simulation of 50 min.

3.2.2.2 Analysis of simulation in irregular waves

An irregular wave in FASTSHIP is modelled with the random phase-amplitude model as,

$$\eta(x,t) = \sum_{i=1}^{N_f-1} a_i \sin\left(\omega_e t + \alpha_i + k(x - LCG) + \varphi_i\right) \tag{3.21}$$

where

a_i: wave amplitude

α_i: random phase

ω_e: encounter frequency

k: wave number

φ_i: additional phase shift that results from letting the waves develop for a user-specified amount of time before the actual (seakeeping) simulation starts.

N_f: number of frequency discretisations of the Jonswap spectrum.

The waves are defined with respect to the boat center of gravity, hence the term $(x - LCG)$ in eq. (3.21). The amplitudes and frequencies are obtained from the Jonswap spectrum [5], with a peak enhancement factor $\gamma = 1.33$.

$$\begin{aligned} E_{Jon}(\mathsf{f}) &= \alpha g^2 (2\pi)^{-4} \mathsf{f}^{-5} \exp\left[-\frac{5}{4}\left(\frac{\mathsf{f}}{\mathsf{f}_p}\right)^{-4}\right] \gamma^{\exp\left[-\frac{1}{2}\left(\frac{\mathsf{f}-\mathsf{f}_p}{\sigma \mathsf{f}_p}\right)^2\right]} \\ \alpha &= 5.061 \mathsf{f}_p^4 H_s^2 (1 - 0.287 log\gamma) \end{aligned} \tag{3.22}$$

The variables that influences the environmental aspect of the analysis are:

- The simulation duration, t_D. Since the analysis of wet deck slamming is formulated from a statistical approach, the amount of wet deck slamming encounters are important. The selected duration should ensure stationary conditions, meaning that it should be long enough to account for a wide variety of waves but short enough to maintain a certain singularity, otherwise extreme events could be masked during the post-processing.

- The number of frequency discretizations of the Jonswap spectrum N_f. Varying N_f will produce a different wave elevation timetrace, thus the consequential output will also (to a certain extent) differ. Therefore, an assessment of the influence of N_f is required in order to ensure the consistency of the output.

- The number of sets of random phases, N_α. The key component for generating irregular waves in eq. (3.21) is the random phase term α. Given an irregular wave modelled with N_f number of frequencies, an array $\bar{\alpha}$ containing an identical amount of random phases is assigned: $\alpha_1, \alpha_2, ..., \alpha_{N_f}$. Considering only one $\bar{\alpha}$, has the risk of obtaining results biased to that particular random irregular wave profile. In order to ensure robustness against random effects an N_α amount of different $\bar{\alpha}_k$ arrays are considered, referred as sets of random phases. The premise is to average the output (number of exceedances) over n_α number of sets of random phases, where $n_\alpha \leq N_\alpha$. The study aims to determine the value of n_α necessary, in order to ensure data consistency at an optimal computational cost.

Linear combinations of the following values of the above mentioned parameters are assembled for the sensitivity study.

$\bar{t}_D = \{20, 30, 40, 50, 60\}$ min.

$\bar{N}_f = \{30, 40, 50, 60, 70, 80, 90, 100\}$

$N_\alpha = 50$. This means that 50 different sets of random phases —$\bar{\alpha}_1, \bar{\alpha}_2, ..., \bar{\alpha}_k, ..., \bar{\alpha}_{50}$— are considered for every combination of the above parameters, and the average across a systematically increasing set of random phases ($n_\alpha = 2, 3, ..., N_\alpha$) is performed. The whole compendium of sets actually results in a quasi-random approach, because every case would be simulated over the same sets of random phases $\bar{\alpha}_k$.

The number of wet deck exceedances N_{exc}, measured at discrete points along the wet deck length will be the response that indicates whether data robustness have been achieved or not. Furthermore, followed from the previous section, same number of discrete points as the mesh size are chosen.
In order to compare the exceedances across the different durations, the exceedance per minute is computed.

$$N_{exc,t_D} = \frac{N_{exc}(x)}{t_{D,i}}$$

And the averaging process over the different sets of random phases is carried out progressively, until the mean is performed over all N_α sets, as follows.

$$\mathbf{avg}_{n_\alpha}(N_{exc,t_D}) = \frac{1}{n_\alpha}\sum_{k=1}^{n_\alpha} N_{exc,t_D,k} \qquad \text{where:} \quad n_\alpha = 2, 3, 4, ..., N_\alpha$$

For the sake of explanation, the analysis of N_{exc} is compared at three different locations, illustrated in the figures figs. 3.15 to 3.17. Namely, at 12%, 50% and 75% of the LOA from the transom. Where different plotting perspectives are adopted, in order to highlight the effect of a particular parameter.

In the figures fig. 3.15a—fig. 3.15h, the response is laid out in eight different samples, corresponding to the different N_f considered. In each of the subplots, the number of exceedances per minute are compared at the above mentioned locations. Where the horizontal axis corresponds to the number of sets of random phases included in the average. As it can be appreciated, each curve (corresponding to a specific simulation duration t_D) clearly stabilises as the data is averaged over more sets of random phases thus, decreasing data uncertainty due to random effects. Moreover, the curves does not show any signs of further convergence as the average is performed over more sets of random phases until $N_\alpha = 50$ is reached. However, the differences between the curves in the stable parts are marginal.
Based on the results, it is concluded that considering $N_\alpha = 20$ ensures a fair robustness against the stochasticity of the environment.

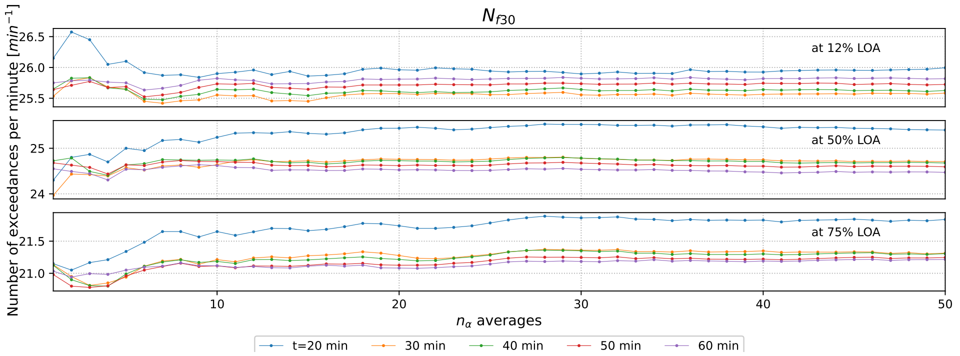

(a) Sensitivity study of the parameters t_D and n_α at $N_f = 30$

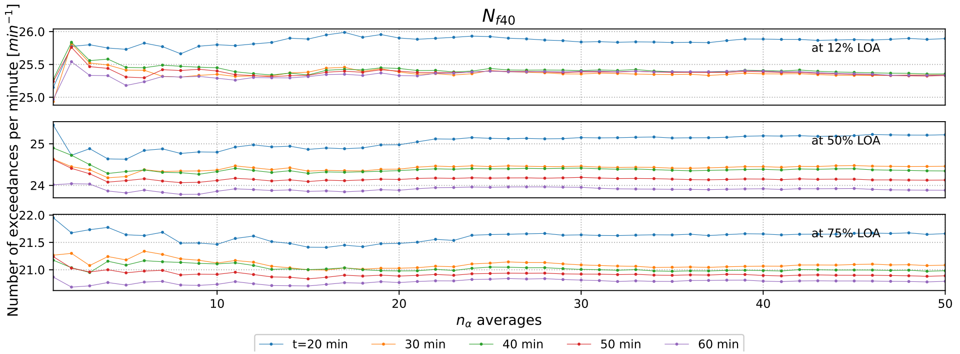

(b) Sensitivity study of the parameters t_D and n_α at $N_f = 40$

Figure 3.15: Part 1 of 3. Analysis of the influence of the simulation duration t_D, number of Jonswap frequency discretisations N_f and number of $\bar{\alpha}$ sets n_α on the number of exceedances N_{exc}. At a three different positions along the wet deck length, namely 12%, 50% and 75% of the LOA with respect to the transom.

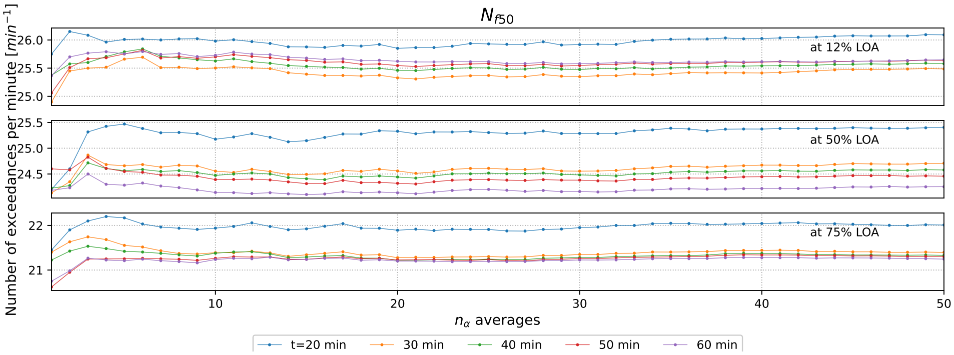

(c) Sensitivity study of the parameters t_D and n_α at $N_f = 50$

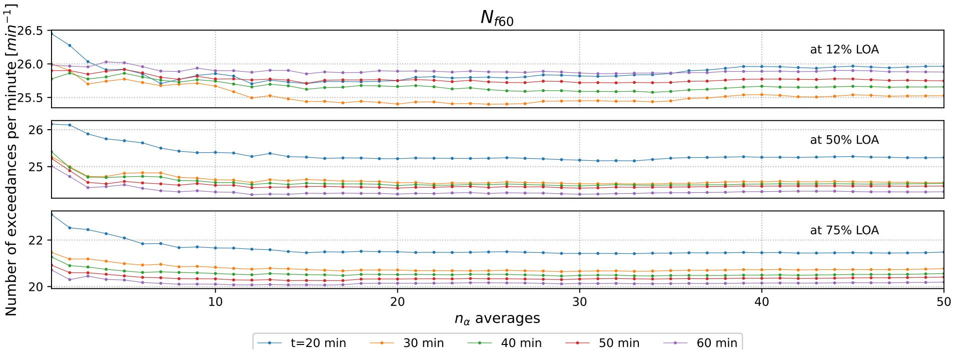

(d) Sensitivity study of the parameters t_D and n_α at $N_f = 60$

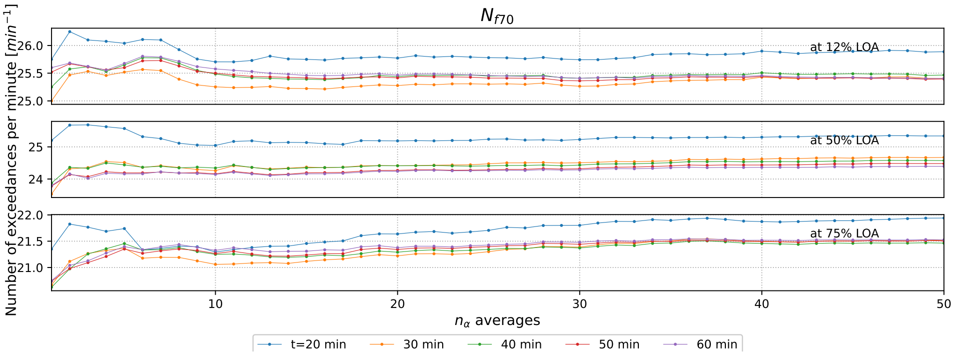

(e) Sensitivity study of the parameters t_D and n_α at $N_f = 70$

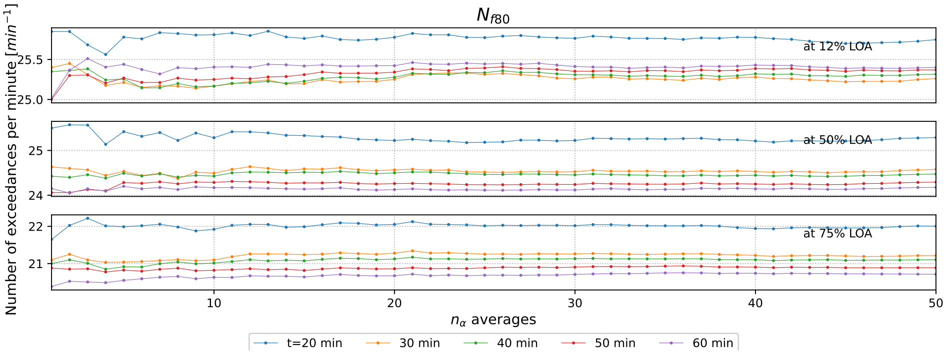

(f) Sensitivity study of the parameters t_D and n_α at $N_f = 80$

Figure 3.15: Part 2 of 3. Analysis of the influence of the simulation duration t_D, number of Jonswap frequency discretisations N_f and number of $\bar{\alpha}$ sets n_α on the number of exceedances N_{exc}. At a three different positions along the wet deck length, namely 12%, 50% and 75% of the LOA with respect to the transom.

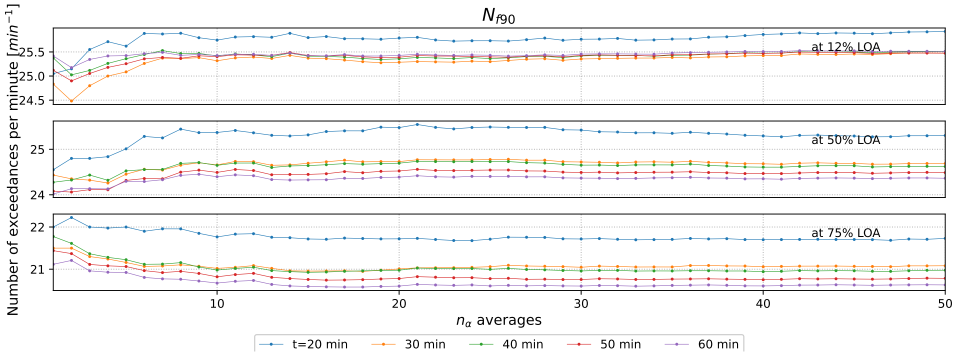

(g) Sensitivity study of the parameters t_D and n_α at $N_f = 90$

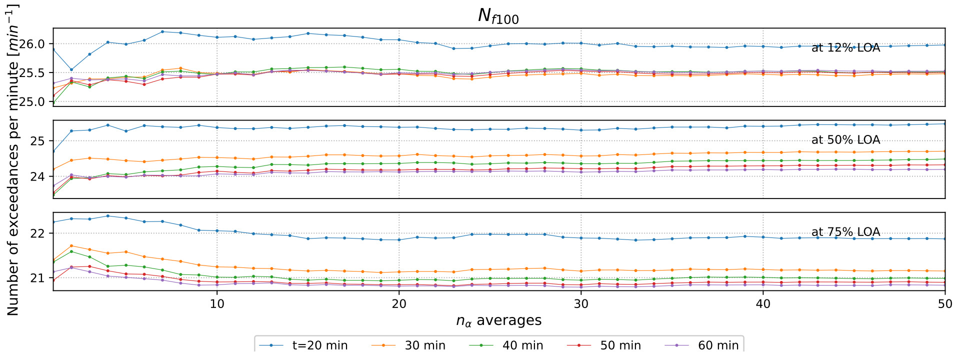

(h) Sensitivity study of the parameters t_D and n_α at $N_f = 100$

Figure 3.15: Part 3 of 3. Analysis of the influence of the simulation duration t_D, number of Jonswap frequency discretisations N_f and number of $\bar{\alpha}$ sets n_α on the number of exceedances N_{exc}. At a three different positions along the wet deck length, namely 12%, 50% and 75% of the LOA with respect to the transom.

With the parameter N_α fixed, in fig. 3.16 the averaged response denoted as $\mathbf{avg}_{20}(N_{exc,t_D})$ is illustrated across the different frequency discretisations N_f, corresponding to the horizontal axis. As it can be appreciated, the results are quite similar and no clear abnormality can be spotted. However, a slightly steadier behaviour is found at higher number of frequency discretisations, starting from 80 frequency discretisations onward. Therefore, $N_f = 80$ is chosen to be the number of frequencies to discretize the Jonswap spectrum.

Finally, a plot with the data obtained from irregular waves composed of $N_f = 80$ discrete frequencies and averaged over $N_\alpha = 20$ sets of random phases are illustrated in fig. 3.17, where the wet deck exceedances is plotted over 80 discrete points along the wet deck length.

Five different simulation duration can be distinguished, where clearly the curve corresponding to the shortest duration ($t_D = 20min$) deviates from the rest. Furthermore, the remaining curves tends to diverge only at the range from 30 to 65 frames while fairly good concordance is obtained elsewhere.
Since the difference amongst the longer duration are small, it is concluded that enough data consistency is obtained with 50 min of duration. Moreover, considering a longer duration would only increase the computational load for just a marginal increase in accuracy.

In summary, it is concluded that response consistency can be attained by performing the average over 20 different simulations, each one with an irregular wave described with a different set of random phase but with the fix number of 80 frequencies, obtained from the Jonswap spectrum. Moreover, each simulation duration is set at 50 minutes.

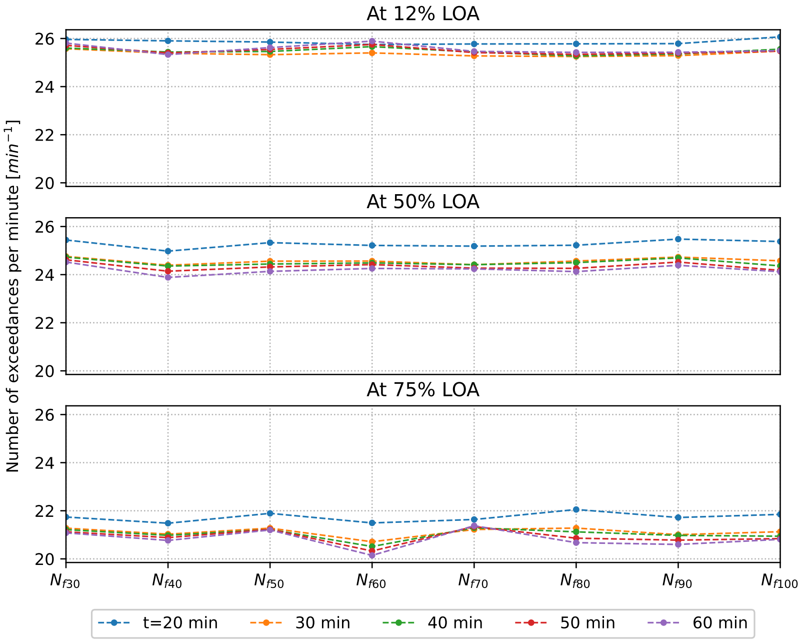

Figure 3.16: Analysis of the influence of the simulation duration t_D and the number of Jonswap frequency discretisations N_f on the number of exceedances N_{exc}. At a position 3 different positions. Data is averaged over $N_\alpha = 20$ samples.

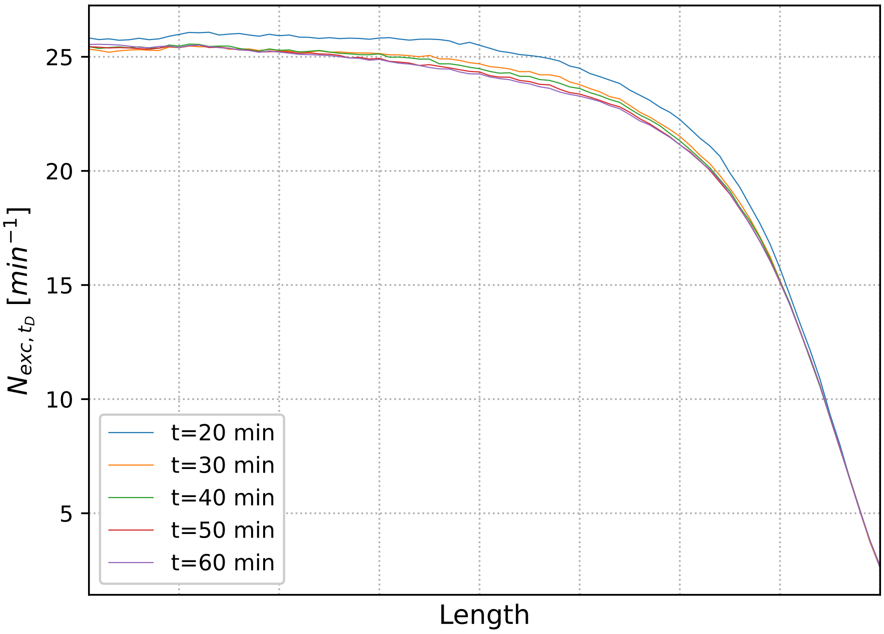

Figure 3.17: Analysis of the influence of the simulation duration t_D on the number of exceedances N_{exc} along the wet deck length, discretised into 80 frames as concluded in the geometry analysis. The data corresponds to a case with the Jonswap spectrum discretised over $N_f = 80$ frequencies and tested over $N_\alpha = 20$ different sets of random phases, to which the averages are computed.

3.2.3 Results

Once the corresponding simulation parameters influencing the output quality are properly set, simulations can be run with confidence. In this section the results of FASTSHIP with the ‘test hull’, the 4212 are shown, with the concluded values for the various parameters introduced in the sensitivity study of the previous section.
In fig. 3.18 and fig. 3.19, a visualisation of the computed hull-wave interaction of the 4212 FFC sailing in regular and irregular waves respectively, is shown (both performed with the same wave characteristics, of significant wave height $H_s = 2m$ and wave period $T_p = 6.18s$, which corresponds to the winter conditions, shown in table 1.2).

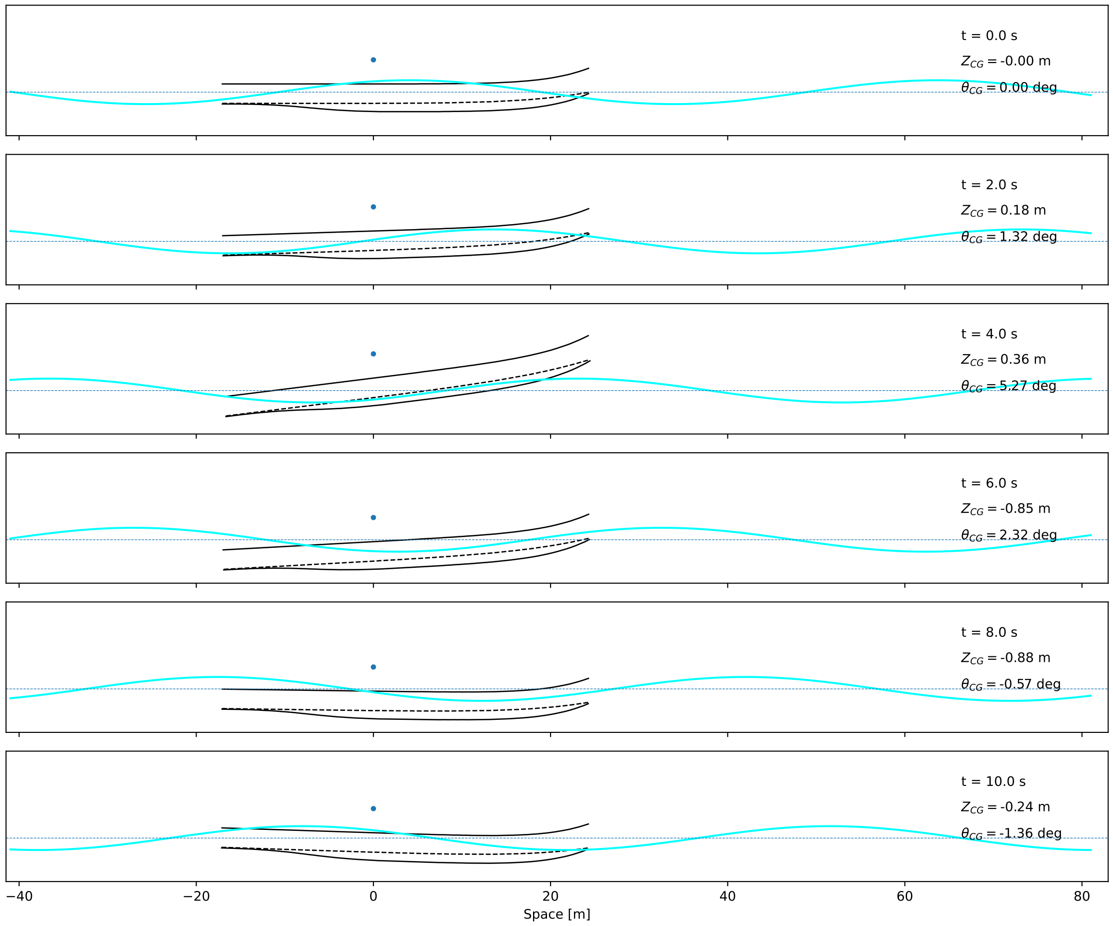

Figure 3.18: Lagrangian view of a short sequence of the 4212 FFC sailing in regular wave at 30 kn. The fragment corresponds to a simulation with a wave of $H_s = 2$ m and $T_p = 6.18$ s.

From a qualitative point of view, the hull motions are fairly well captured, as the hull nose rises and falls accordingly to the incoming wave, as specially appreciable in fig. 3.18. Furthermore, it can be appreciated how generally the aft-most part of the wet deck is exceeded most of the times (although this only indicates the amount of times the local wet deck has been wetted).
Plotting the number of wet deck exceedances N_{exc} along the wet deck will typically result in a distribution like fig. 3.17, confirming that the aft-most sections touches the free surface more frequently than the fore-most parts. However, it is known from experience that generally wet deck slamming occurs at approximately 75% of the hull length from transom, moreover, this can be further confirmed from the reports about the *Nina* (pictured

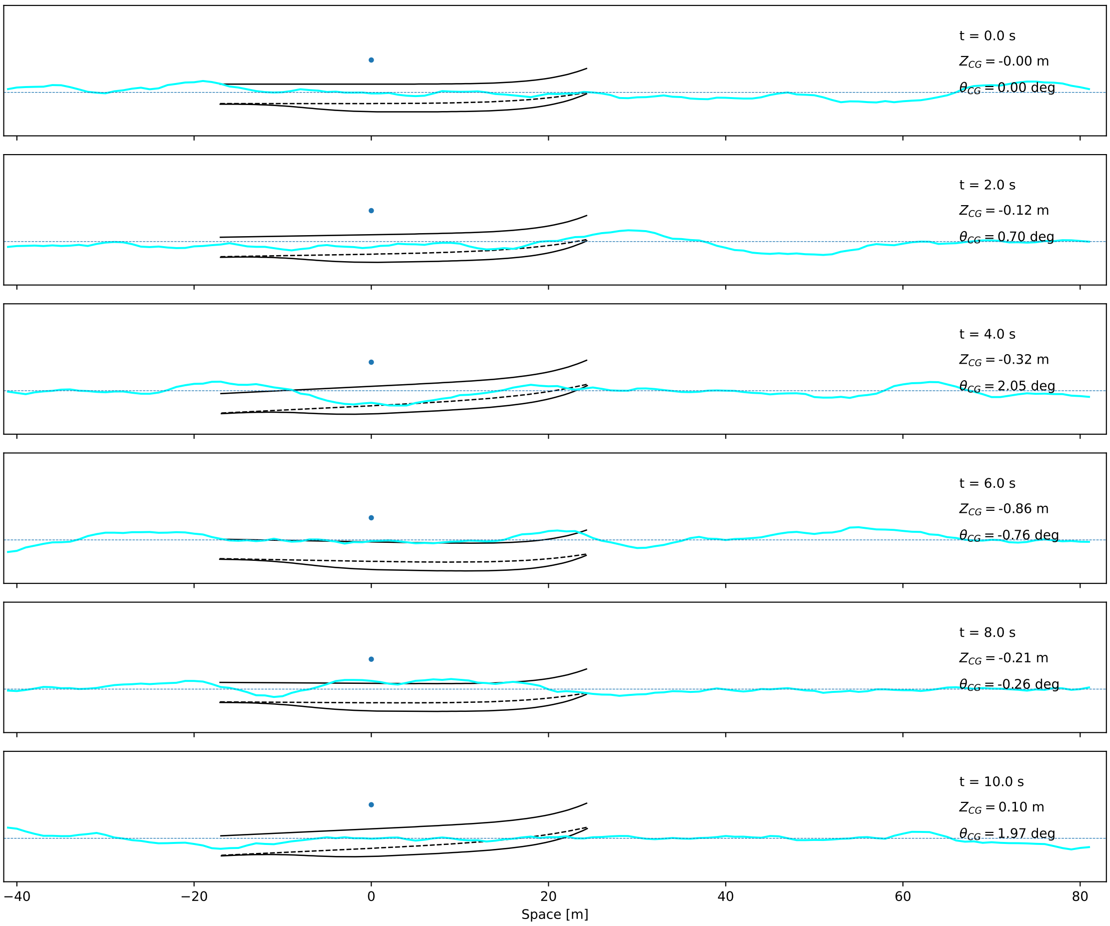

Figure 3.19: Lagrangian view of a short sequence of the 4212 FFC sailing in an irregular waves at 30 kn. The fragment corresponds to a simulation with a Jonswap spectrum of $H_s = 2$ m and $T_p = 6.18$ s.

in section 1.1).

In order to have a better insight, the slamming velocity, considered as the velocity in which the local wet deck and free surface makes first contact, is examined. The reason follows from the experiments performed by *Swiedan A.* [24] (see section 1.2) who determined an existing linear relation between the slamming force and the square of the impact velocity. In fig. 3.20, the mean and the maximum of the slamming velocities over the entire simulation duration computed at various discrete points along the wet deck length (same discrete points as the mesh size) denoted as V_{mean} and V_{max} respectively, are shown. As it can be appreciated, the larger mean slamming velocities occurs at the fore-most parts, where wet deck exceedance is lower thus, slamming forces are more severe but less frequent. The combination of such mean slamming velocity profile and the wet deck exceedance profile somewhat counter acts, as the opposite happens on the rear part, with higher wet deck exceedance but lower mean slamming velocities. Regarding the maximum recorded slamming velocities, an irregular profile is obtained, where the highest velocities happens at the aft-most parts.

In order to display all the impulses occurred during the entire simulation, a frequency distribution plot is used, shown in fig. 3.21a, where impulses are divided in slots of different magnitudes. The overall number of impulses N_{imp} recorded over the simulation are 1071. Furthermore, an analogous plot with the impulses duration is also displayed, shown

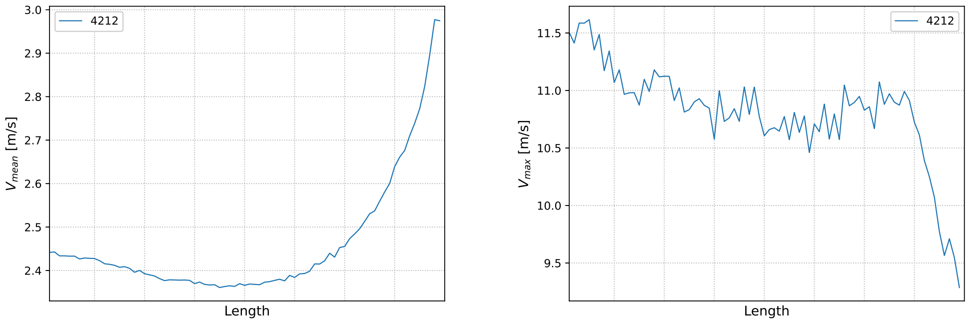

(a) V_{mean} distribution over the wet deck length **(b)** V_{max} distribution over the wet deck length

Figure 3.20: Mean (left) and maximum (right) wet deck slamming velocity distribution over the wet deck length. For $t_D = 50$ min in irregular waves of $H_s = 2$ m and $T_p = 6.18$ s.

in fig. 3.21b.
According to them, the lowest impulses have higher chances of occurrence (around 10%) while the most severe impulses have lower chances. As a matter of fact, in absolute numbers, the most severe impulse happens on the order of once or twice over the entire course of the simulation. Meanwhile, the mid-range follows a somewhat Rayleigh-like distribution.

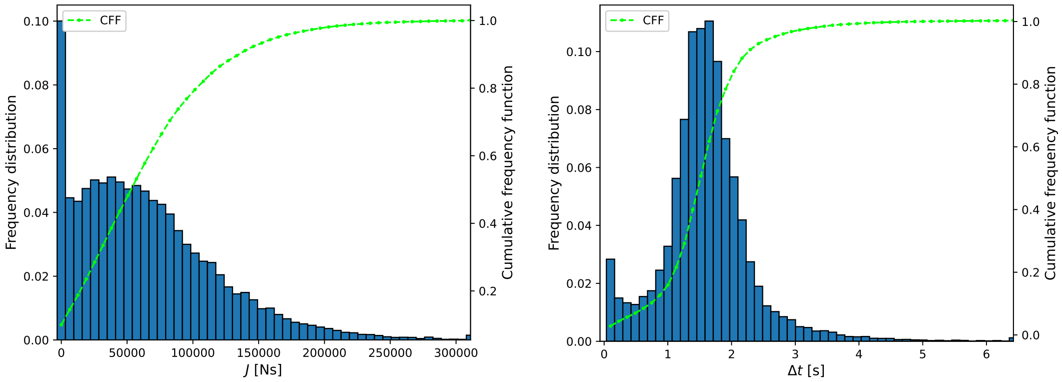

(a) Frequency distribution and CDF of the impulses recorded along the simulation. **(b)** Frequency distribution and CDF of the impulse duration recorded along the simulation

Figure 3.21: Frequency distribution and the Cumulative Distribution Function (CDF) of the impulse (left) and its time span Δt (left).

Further details regarding FASTSHIP set-up for the obtainment of the present outputs can are explained in Appendix A.2.

4

Design of Experiments

Design of Experiments (DOE) is the study that seeks to extract as much information or as many data trends as possible from an experiment from a limited number of sample points. DOE procedures allow the user to strategically manage the computational resources in order to explore the input(s) and the consequential output(s) domain of the experimental set-up. Furthermore, it analyses their relation and the possible limitations.

Experiments can be distinguished between physically based, such as the ones set in a laboratory and computationally based, such as numerical methods. The main difference lies on the nature of their output, where the former can be non-deterministic and the latter is fully deterministic.

Thus, Design and Analysis of Computer Experiments (DACE) is introduced, DACE is a branch within DOE intended for computational based experiments. Unlike physical experiments, which are subjected to stochastic processes (that is, the same inputs might produce different outputs), computer experiments are the opposite, because they are based on repeatable processes. Therefore, DACE can focus the computational resources on performing large distribution of samples throughout the input domain in order to cover as much space as possible. Unlike physical experiments, where part of the computational resources have to be aimed at ensuring data consistency.

The means to carry-on such study is with DAKOTA, a program aimed for the aid, assessment and management of any kind of experiment or simulation set-up, within the scientific or engineering community [1].

In the present chapter, a design exploration of the input space of the parametric hull for FASTSHIP, introduced in chapter 2, is performed. The analysis first starts with an exploration of the input variables and their influence on wet deck slamming, according to the methodology explained in section 3.1. From this step, a proper understanding of the input space is extracted, and with the obtained knowledge a reformulation of the input space can be done if necessary.

Once the input space is consolidated, a sampling method is applied in order to populate the input space in the most homogeneous way possible, thus eventually performing the actual input space exploration. However, this kind of studies requires a large amount of samples, of the order of thousands, which for the present case supposes an unfeasible computational load. Therefore, a surrogate model is built from a computationally feasible sample size, which will allow for mass production of hull individuals that can spread across the input space at an inexpensive cost.

From the hull population, generated by the surrogate model, the best performing hulls can be filtered aside for posterior analysis, thus eventually carrying out the goal of the study, the identification of the demihull geometrical characteristics that can potentially lead to reduction of wet deck slamming [1].

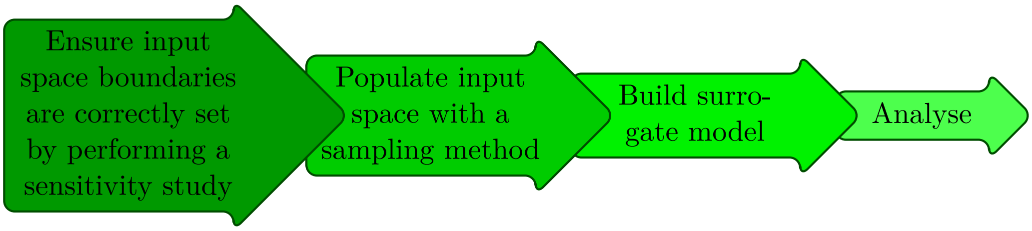

Figure 4.1: Flow chart illustrating the process and content of the chapter

4.1 Parametric hull design analysis

The DOE procedures applied to the parametric hard chine hull for FASTSHIP is presented in this section. All the simulations are held with the correspondent FASTSHIP parameter values tuned according to the parameter analysis described in section 3.2.2.

Sensitivity study of the input space

A sensitivity study is performed on the input space of the parametric hull in order to assess the correct magnitudes each input variable should adopt, by defining the upper and lower boundaries. Hence, reducing any impractical hull shape that could arise from an odd combination of the input variables, and ensuring all hulls within the design space are of interest.

As introduced in section 2.2.3, the parametric hull is defined by a total of 11 input variables. For the first step, the initial set of boundaries are defined in a rather coarse way, based on the author's criteria (to avoid extreme and unreaslistic shapes, with no physical intention behind whatsoever), and eventually redefine it based on posterior results. Moreover, the set of input values corresponding to the 4212 will be used as reference during the study, shown in table 4.1.
Each variable will be varied in a Morris One-At-A-Time (MOAT) fashion, where the variables are varied one by one while the rest are kept to the original reference values. Furthermore, an evenly distribution within the initial defined boundaries will be performed. Although the current application of the MOAT analysis slightly varies from the original procedure, as outlined by *M. D. Morris* (199) [15], the approach allows for the analysis of the influence of each variable within the space to the output in an isolated manner.
A typical rule of thumb in sampling methods is to generate a sample size between five and ten times the number of input variables. The rule is actually meant for stochastic sampling methods, however, it is deemed reasonable to extrapolate this rule into the current case. Therefore, ten evenly distributed values within the user defined boundaries are sampled for each variable.

These results in 110 different hulls plus the reference hull.

Variables	**Dimension**	**Tag**	**4212**	**Lower-Upper boundaries**
x_1	$[-]$	nchine	2.5	2 — 10
x_2	$[-]$	ndeck	3.5	2 — 10
x_3	$[-]$	mchine	6	0.5 — 20
x_4	$[-]$	imkeel	0.21428	0 — 1
x_5	$[m]$	Bchine	3	2 — 4
x_6	$[m]$	Bdeck	3.28	2 — 4
x_7	$[m]$	chineHa	0.7	0.7 — 1.5
x_8	$[m]$	chineHb	1.7	0.5 — 2
x_9	$[-]$	ikeelH	0	0 — 1
x_{10}	$[-]$	Lambda	50	10 — 100
x_{11}	$[-]$	Alpha	3	1.5 — 3.5

Table 4.1: Parametric hull input variables

The results of all 110 hulls and the comparison with respect to the reference hull, will be next shown.

In fig. 4.2a, all the impulse frequency distributions are shown together with the reference hull. As it can be appreciated, all curves maintain roughly the same shape, moreover, the reference hull represented by the thick bold line is somewhat at the center of the extreme distributions, which given the chosen boundaries it is expected. The hulls with better performance against wet deck slamming should have frequency distributions with fewer and lower extreme impulses.

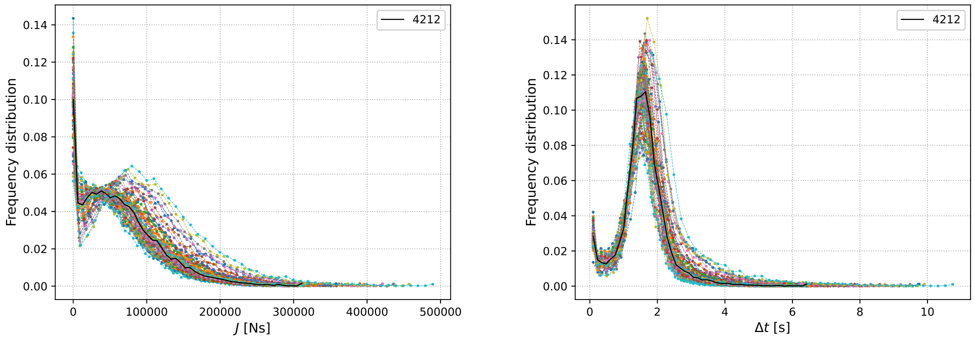

(a) Comparison of the impulse frequency distribution amongst 110 hulls generated from a MOAT scheme with the 4212 as reference hull

(b) Comparison of the impulse Δt frequency distribution amongst 110 hulls generated from a MOAT scheme with the 4212 as reference hull

Figure 4.2: Frequency distribution comparison amongst 110 hulls generated from a MOAT scheme. Showing the impulse frequency (left) and the impulse Δt frequency (right) distributions.

A further analysis on the impulse frequency distribution is realized by considering some typical characteristics such as the mean impulse J_{mean}, the maximum recorded impulse J_{max} and the 95-percentile J_{95}. The first value (as it will next explained) roughly describes the whole distribution, while the latter focuses on the extreme impulse occurrences. As illustrated in fig. 4.3a and fig. 4.3b, by plotting the worst impulse occurrences with the

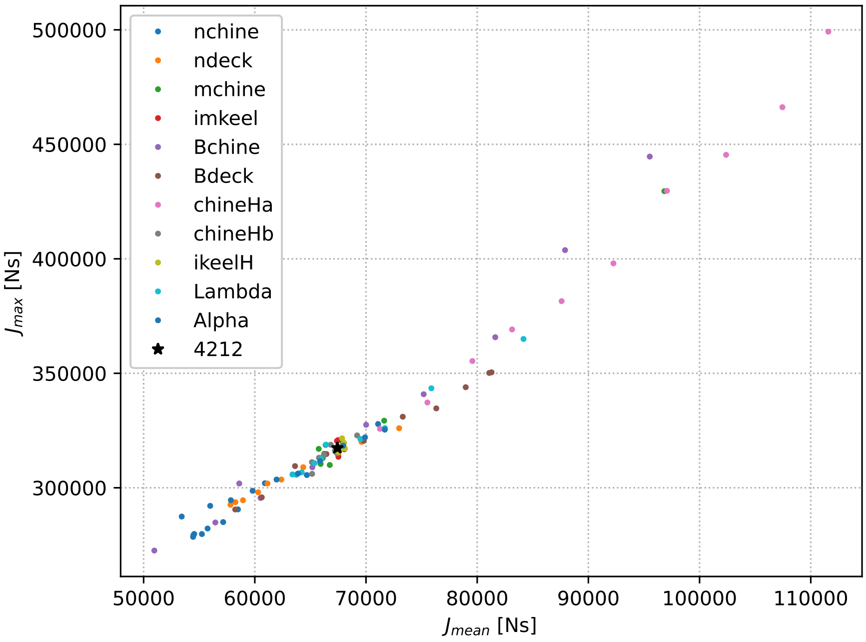

(a) Comparison of the mean impulse and the maximum impulse of every hull in table 4.1. The data are differentiated by the varied input variable with different colors.

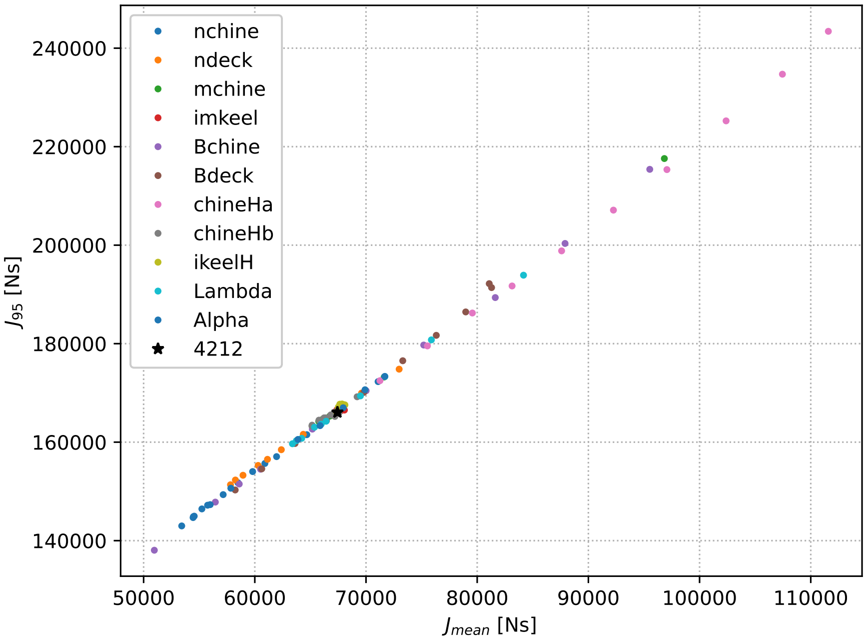

(b) Comparison of the mean impulse and the 95-percentile impulse of every hull in table 4.1. The data are differentiated by the varied input variable with different colors.

Figure 4.3: Impulse analysis between the hulls generated for the sensitivity study of the input space

mean impulse, a linear relation is obtained (especially for the J_{mean} vs. J_{95} plot). Therefore, according to these relations it can be inferred that lower mean impulses will result into lower extreme magnitudes. Thus, the mean impulse can be considered a fair repre-

sentative of the whole impulse frequency distribution that will implicitly result in lower worst impulse occurrences.
Reducing the amount of impulse-related variables to one, will prove to be convenient and necessary for later stages of the study, as it simplifies the optimisation procedure and the overall computational load.

In order to analyse the influence of each input variable over the different responses, for instance the aforementioned mean impulse or the number of impulses recorded over the simulation or the maximum number of wet deck exceedances, or the mean slamming velocities, a normalisation of the inputs and their corresponding output is performed by dividing them over the analogous value of the reference hull, as follows

$$\begin{aligned} \text{Input:} \quad & \frac{x_i}{x_{4212}} \\ \text{Output:} \quad & \frac{f(x_i)}{f(x_{4212})} \end{aligned}$$

where x_i are the input variables presented in table 4.1, $f(x_i)$ is the corresponding response function, and where the sub-index 4212 denotes for the reference hull.

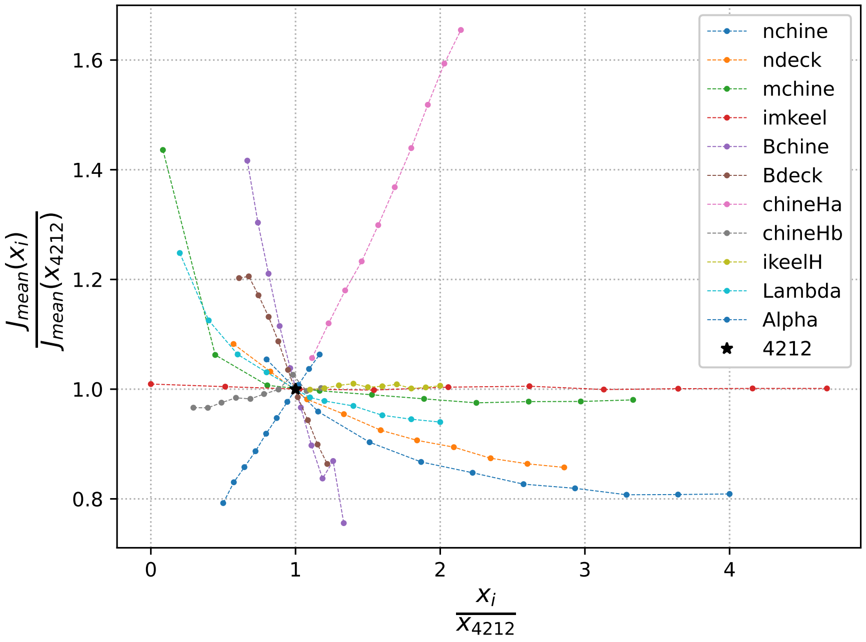

(a) Influence analysis of the input parameters to J_{mean}

Figure 4.4: Part 1 of 3. Influence analysis of the input parameters to the various considered responses: the mean impulse J_{mean}, the number of impulses N_{imp}, the maximum number of wet deck exceedances N_{exc} and the mean slamming velocity V_{mean}.

The influence of the various input variables over some of the (normalised) responses introduced in section 3.2.3 are analysed next. Namely the J_{mean}, the number of impulses N_{imp}, the maximum number of exceedances N_{exc} and the mean slamming velocity V_{mean}, illustrated in figs. 4.4a to 4.4d respectively. Where the abscissas are the normalised input variables and the ordinates the normalised responses.
The resultant plots have a characteristic spider shape with the reference hull at its centroid. When the normalised response is > 1, a worst performance with respect to the

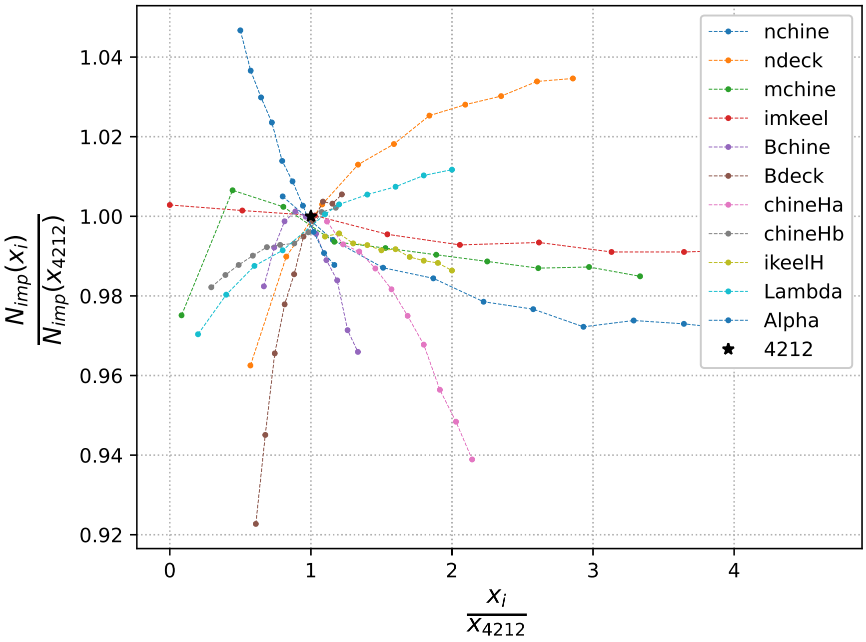

(b) Influence analysis of the input parameters to N_{imp}

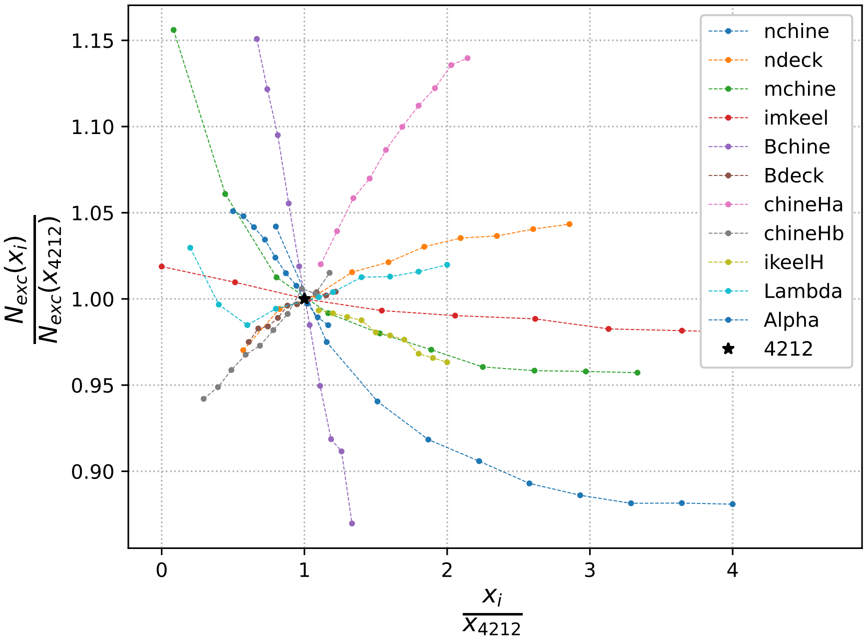

(c) Influence analysis of the input parameters to N_{exc}

Figure 4.4: Part 2 of 3. Influence analysis of the input parameters to the various considered responses: the mean impulse J_{mean}, the number of impulses N_{imp}, the maximum number of wet deck exceedances N_{exc} and the mean slamming velocity V_{mean}.

reference hull is obtained and viceversa. As it can be appreciated, there are certain lines that are more horizontal, thus unveiling a lower influence on the responses, such as imkeel (represented by the red curve). On the contrary, curves that are simply less horizontal or oblique denotes a higher influence on the response. Within these types, curves that eventually displays horizontal trends shows that a certain threshold can exist where no

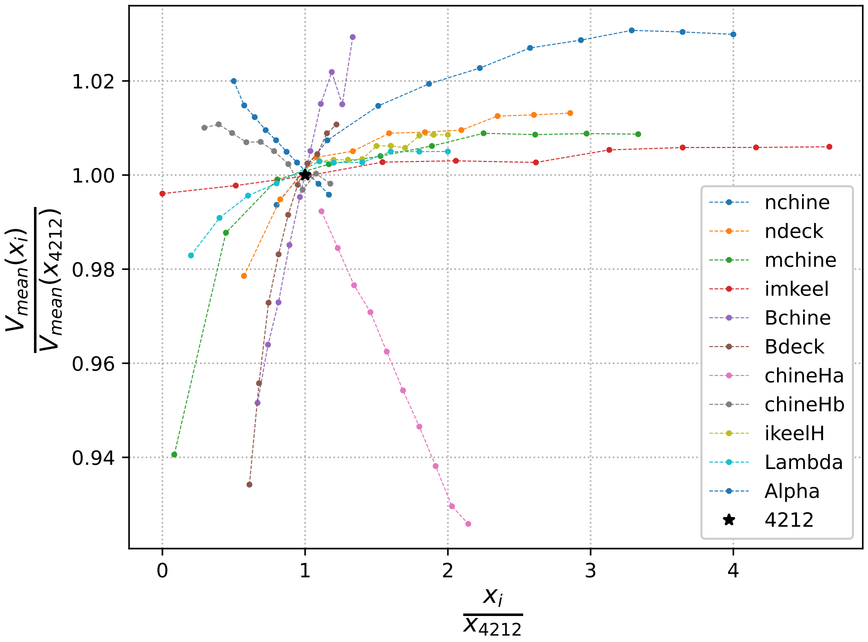

(d) Influence analysis of the input parameters to V_{mean}

Figure 4.4: Part 3 of 3. Influence analysis of the input parameters to the various considered responses: the mean impulse J_{mean}, the number of impulses N_{imp}, the maximum number of wet deck exceedances N_{exc} and the mean slamming velocity V_{mean}.

further signs of improvements can be achieved, such as in the case of `nchine` (represented by the blue curve).

It is worth mentioning that among the displayed influences, the resultant response deviations from the reference hull for N_{imp} and V_{mean} are quite narrow compared to the rest. In table table 4.2, the standard deviation of the presented responses with respect to the reference hull are displayed (in percentage). Where N_{imp} and V_{mean} have a deviation of approximately 2%, thus the actual impact is not as big as it may seem.

Response parameter	**Standard deviation** [%]
J_{mean}	16.28
N_{imp}	2.06
N_{exc}	5.56
V_{mean}	2.12

Table 4.2: Standard deviation of the considered responses with respect to the reference hull, the 4212.

The MOAT analysis approach only shows the influence of the input variables in isolation. In order to check whether the interaction between the input parameters is constructive or not, the combination of the values that lead to an improved response is carried out, and the corresponding relative deviations with respect to the reference hull shown in table 4.3. The relative deviation is computed as follows

$$\frac{f(\bar{x}_{new}) - f(\bar{x}_{4212})}{f(\bar{x}_{4212})} \cdot 100 \tag{4.1}$$

where the subscript new denotes for the point containing the above mentioned input parameters. A positive relative deviation translates into worst performance and vice versa. The outcome turned to be positive, as it can be appreciated, where J_{mean}, N_{imp} and N_{exc} where substantially reduced compared to the results from the MOAT analysis. However, the V_{mean} response resulted in a slightly worse performance.

Response parameter	**Improvement** [%]
J_{mean}	-54.87
N_{imp}	-12.64
N_{exc}	-23.04
V_{mean}	5.81

Table 4.3: Table displaying the performance of a hull with $\bar{x}_{new}$ containing all the input values that showcased a positive influence on the response according to figs. 4.4a to 4.4d with respect to the reference hull, computed as eq. (4.1)

Based on the results presented in this study, a redefinition of the upper-lower boundaries of the input parameters is carried out. By correcting the boundaries of each input parameter, the input space domain is redefined and the chances of producing hulls with a negative performance reduced. Thus, computational resources can be directed towards a (more) meaningful response surface.

In the DOE studies, reducing the number of input parameters not only reduces the computational load but also simplifies the evaluation of the corresponding results. Thus, it is common practice to try to simplify the problem by attempting such reduction. Some of the typical techniques are outlined in [9]. For the present case, a reduction from 11 to 10 input parameters is conducted, by removing the input variable Lambda, one of the two variables that affects the hull aft-bottom clearance, a space intended for propulsion devices (namely waterjets). The main reason is due to the high influence on the hull geometry, deemed too big, leading to unreasonable hull bottoms. Furthermore, the control of such part of the hull can be relayed to the remaining variable, which effects on the hull geometry are less extreme.

Once the input space domain is properly defined, a sampling-based method can be applied in order to populate it. The sampling-based methods are next discussed.

4.2 Sampling methods

In the present section, sampling-based methods for populating the input space domain, evaluated in the previous section, is explored.

Sampling-based methods are mathematical models aimed for the selection or generation of subset(s) of data contained within the parameter space of a system, for its analysis. Such methods can be valuable data managers, that are independent of the scientific disciplines involved in the analysis and furthermore, relatively easy to implement. There are many sampling-based methods, each one producing set of samples with a specific probability distribution of the uncertain variables, but all intended for mapping the response space by producing the corresponding sets of response functions.

The sampling methods considered in the present work are within the DOE context,

where a proper sampling is expected to generate a finite number of points according to the user's necessities, which can either be focused towards large homogeneous spread of points covering the parameter space of dimension p or focused towards an heterogeneous spread with higher density of points in specific area(s).
Determining which type to choose will mainly depend on the analysis objective but also on the level of understanding of the problem. Since the current analysis wishes to explore the input space of the parametric design tool, studied in the previous section, a large cloud of points is preferable.

Various sampling-based methods were considered for the study, which will be next introduced. A extensier description can be found in Appendix B.1, nevertheless a small description will be provided.
The methods are distinguished between two main groups, classic DOE sampling methods and stochastic-based sampling methods, as outline in [1]. The latter, (as the name infers) are based on random sampling mechanisms while the former are based on repeatable mechanisms that obey a certain strategy or criterion for generating the subset of points.

Classic DOE sampling methods

The classical non-stochastic-based methods tested are namely: Box-Wilson Central Composite Design (CCD), Box-Behnken Design (BBD), Orthogonal Array Designs (OA), Grid Design (GD), Central Voronoi Tesselation (CVT) and Morris One-At-A-Time method (MOAT).

Non-stochastic-based sampling methods applies specific sampling mechanisms inspired by a certain pattern or structure. For instance, the CCD and the BBD are methods that builds m number of points around a central one, which is the evaluation point. Although, the position with respect to the central point is specific to the method, it will generally fall either at an user specified upper-lower boundary or at the middle, as depicted in fig. 4.5. Thus the method will involve m^p number of points, where p is the number of parameters [16].

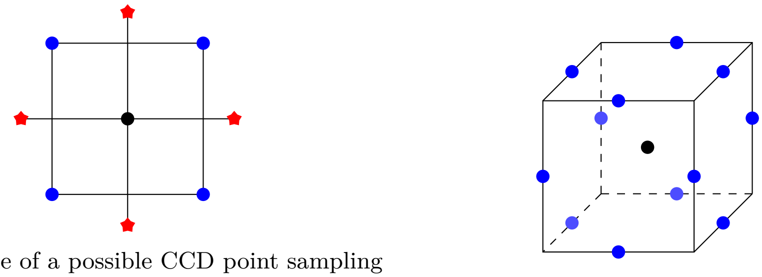

(a) Example of a possible CCD point sampling arrangement known as two factor CCD, where $p = 2$. Therefore, the blue dots denotes for the pair of upper-lower limits. Additionally, star points illustrated in red are set to screen for surface response curvature.

(b) Example of a possible BBD point sampling arrangement with $p = 3$. The method mainly screens the response at the mid-points of the space limits.

Figure 4.5: Schematic of a typical Box-Wilson Central Composite Design (CCD) and Box-Behnken Design (BBD) sampling method point arrangement.

Other types of sampling methods assumes that all the input parameters are independent from each other, such as the OA, thus, it exploits the array orthogonality concept. Given an array based on user specified p number of values for each of the m input parameters, orthogonality is achieved by arranging the p^m amount of data in unique tuples (meaning, non-repeated combinations of values within an array of input parameters). The

aim is to perform pairwise comparison of tuples in an isolated manner.
Another method that works towards isolating the input parameters for posterior analysis is the MOAT method, where the input parameters are varied one-by-one. Thus, trying to assess the influence of the particular input parameter to the output.

There are also classic DOE sampling models that are directed towards wider spread of points, such as GD or CVT. The former is basically a mesh of dimension p, that can be structured or with an added random perturbation. The latter is identified to be the most suitable amongst the mentioned so far for the current study. CVT is a special type of Voronoi tessellation where the points of each Voronoi cell are also its centroids [7], as depicted in fig. 4.6. Moreover, it provides satisfactory sampling homogeneity, specially for high dimensional domains (>2)

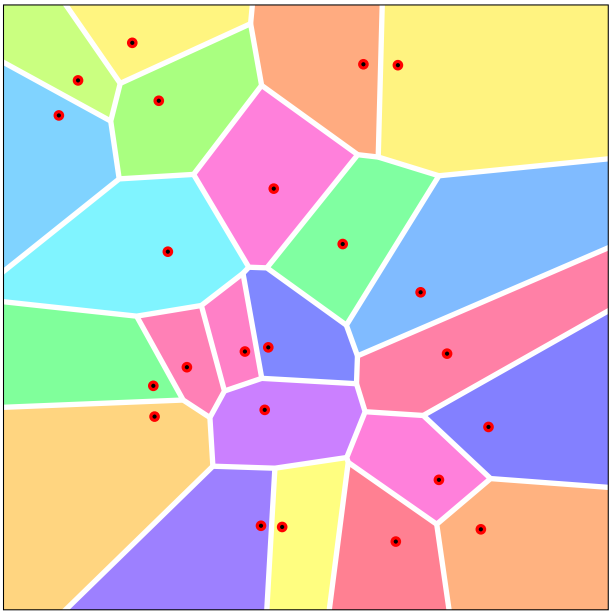

Figure 4.6: Example of a CVT point distribution. The limits of each Voronoi cell denotes for the boundaries upon which any point within it is equally distanced to the neighbouring points. Thus, CVT locates m number of points in representative areas within the system domain.

Stochastic-based sampling methods

Stochastic-based sampling methods relies on random processes to generate m samples. The methods considered are namely Monte-Carlo sampling (MC) and Latin Hypercube Sampling (LHS). MC sampling method is a purely stochastic method that applies an uniform distribution to generate the samples. LHS is actually a near-random sampling method, because it only allows one sample per crossing hyperplane in a multi-dimensional domain. The chosen point distribution for the LHS may vary according to the user's necessities. Furthermore, LHS keeps record of the pseudo-random samples, meaning that for every new point, a considerations of the existing points are taken beforehand [1].

In fig. 4.7 a comparison between MC and LHS is illustrated for 5 and 10 samples, in a 2-dimensional domain. As it can be appreciated, LHS keeps the points more spaced between each other, unlike MC. Furthermore, it achieves a greater spread across the domain.

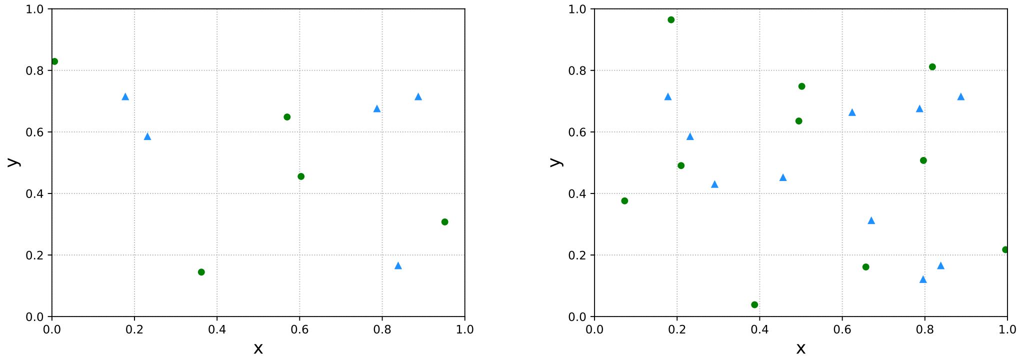

(a) Comparison with 5 samples **(b)** Comparison with 10 samples

Figure 4.7: Distribution of input sample points for MC (triangles) and LHS (circles) sampling for $m = 5$ and $m = 10$. Same seed was used for both methods.

From the various mentioned sampling-based methods, it is concluded that stochastic methods resonate better with the project necessities. Mainly because a wider spread of points across the parameter space can be achieved, and the point-generating mechanisms are much simpler, which results in a faster and more inexpensive procedures. Within them, LHS is deemed to be the best choice because it maintains a better homogeneous distribution of points, unlike MC methods. Moreover, LHS is also the recommended according to the literature in regards to design space exploration involving a surrogate model.

Once the sampling-based method is chosen, the input parameter space can be properly populated, ready for the generation of the surrogate model, explained next.

4.3 Surrogate model

In the engineering fields, numerical procedures involving multiple simulations often struggle with undesired handicaps such as too long simulations or too large amount of simulation procedures. This translates into unfeasible duration or costs for the companies to assume. Surrogate models are inexpensive approximate models that are intended to capture the salient features of an expensive high-fidelity model. Thus, it uses data from the input and (consequential) output space of the high-fidelity program, known as the 'truth model' to build an approximate model. The data used for learning, are called the 'training data', and once the surrogate model is built, responses from unsampled locations can be inferred. Surrogate models can be used to explore the variations in response quantities over regions of the parameter space, or they can serve as inexpensive stand-ins for optimization, uncertainty quantification studies or calibration [1].

There are many surrogate models, following the categorisation described in [2], two main groups can be distinguished, data fit surrogate models and multifidelity surrogate models, next explained.

Data Fit Surrogate Models
Data fit-based surrogate models are non-physics-based approximation methods which typically involves interpolation or regression of a set of data —response values, gradients, and Hessians— generated from the truth model. These type of models, are usually only practical for problems where there are a small number of parameters (according to [2], approximately between 30 to 50 design parameters).

Data fit methods can be further categorized based on the number of points used in generating the data fit, namely local, multipoint and global approximation techniques.

- **Local approximation:** The training data for this kind of models are a single point in the parameter space, plus gradient and Hessian information. The approximation is performed by means of the (first or second-order) Taylor series expansion.
- **Multipoint approximation:** The training data are formed by two or more points in the parameter space. This type of models uses data (typically) from previous iterations to improve the current local approximation accuracy. Thus, it is a model most suitable for problems involving iterative processes.
  Similar to local approximation models, Taylor series is also used as an interpolator.
- **Global approximation:** When a considerable number of training data are available, practically mapping the entire parameter space of interest (often generated with DOE methods), global approximation models works best. Also, known as surface fitting models.

Mutlifidelity surrogate models
Multifidelity surrogate models are a hierarchical type of models that involves the use of a high-fidelity model as its main true model and a low-fidelity model as the secondary, used as the surrogate in place of the high-fidelity model. The latter is still physics-based but with somewhat poorer assumptions such as coarser mesh, looser convergence tolerances, reduced element order or omitted physics. Thus, it is computationally inexpensive compared to the main model. For instance, an inviscid, incompressible Euler CFD model on a coarse discretization could be used as a low-fidelity surrogate for a high-fidelity Navier-Stokes model on a fine discretisation.

Since the study only involves the program FASTSHIP as the truth model, data fit surrogate models are the natural choice. Within them, global approximation types are deemed the most suitable option because they are oriented for global surface mapping (which matches with the study objective) unlike local and multipoint approximations. Furthermore, the necessary requirements can be easily met and it avoids computing information such as gradients and Hessians.

Interpolation techniques (for data relation) within global approximation-based surrogate models can be based on polynomial models (linear, quadratic or higher orders), Taylor series-based, Gaussian process-based (Kriging), artificial neural network, Multivariate Adaptive Regression Splines (MARS) and more. As outlined by *Haftka R. T.* et al. (2010) [9], after comparing the performance of various surrogate models, it was concluded that there was not such thing as ‘the best’ surrogate model. Such choice will depend on the nature of the problem and the sampled points.

For the present work, a popular state of the art surrogate model for computer experiments known as Kriging is chosen, also know as Gaussian Process regression, explained next. The reason to choose Kriging over other methods is due to the large amount of literature available, which not only ensures information but also makes it easy for the DOE community to relate, and last but not least, because it is the recommended by the Damen (expert) sources[7].

---

[7] Assessment from the R&D department of Damen was obtained regarding to the various DOE topics

4.3.1 Kriging

Kriging, also referred to as Gaussian Process regression, is a statistical approach for interpolating functional relationships that relies on covariances and linear weights, which in turn, accounts for spatial continuity, data closeness and data redundancy (these concepts will be further addressed below) [13].
As previously introduced, Kriging corresponds to the data-fit type of surrogate model, meaning that its level of performance solely depends on the training data, does not require pre-assumptions on the relation between input(s) and output(s) and is physical-based process independent. However, if the differences in magnitude of the variables in the training data are big, scaling pre-processing[8]might be necessary.

A valuable property of Kriging that can suppose an advantage compared to other surrogates is that the measure of uncertainty estimation of the predicted data is implicit in its formulation. Furthermore, it is an exact interpolator and a surface "smootherer", meaning that it will return the same exact response as the training data at the same spatial coordinates, and provides the best estimate of the response(s) possible elsewhere based on given data, respectively.

Let $Z(\bar{x})$ be the truth model evaluated at the input domain $\bar{x}$, which is an array formed by p number of inputs $x_1, x_2, ..., x_p$, thus $\bar{x} \in \mathbb{R}^p$. And let $\hat{Z}(\bar{x})$ be the Kriging model, an approximation of $Z(\bar{x}) \in \mathbb{R}$. Moreover, given m number of observations (training data), the corresponding responses (by the truth model) are obtained, $Z(\bar{x}_1), Z(\bar{x}_2), ..., Z(\bar{x}_m)$, each assumed to result from a Gaussian distribution process, and linear combinations of these observations are performed in order to predict the response at new points. Such combinations are determined by some weight factors. The Gaussian Process and the weight factors will be next explained, combining both concepts shall yield the Kriging.

Gaussian Process

A Gaussian process is defined by a mean function $m(\bar{x})$ and a random function $g(\bar{x}) \in \mathbb{R}$, which has a zero mean and standard deviation $\sigma(\bar{x}) \in \mathbb{R}$ [12]. The mean function describes the trend of the local mean and it can be further expressed as

$$m(\bar{x}) = f(\bar{x})^T \bar{\beta} \tag{4.2}$$

where the $\bar{f}(\bar{x})^T$ term is a basis functions and the $\bar{\beta}$ term an array containing regression coefficients. As aforementioned, the observations $Z(\bar{x})$ are assumed to follow from a Gaussian process, thus the following is true

$$Z(\bar{x}) = f(\bar{x})^T \bar{\beta} + g(\bar{x}) \tag{4.3}$$

Three types of Kriging models can be distinguished based on the behaviour of the mean in the data set, which will in turn determine the mean function. When the mean is known the Kriging model is referred as Simple Kriging (SK) and the mean function is often treated as $f(\bar{x})^T \bar{\beta} = 0$, when the mean is unknown but assumed constant anywhere in the domain, the model is referred as Ordinary Kriging (OK) and $f(\bar{x})^T = 1$. And finally, when the mean is assumed to have a trend, the term Universal Kriging (UK) is used, which is a generalisation of SK and OK [3, 14].

---

involved in this thesis, but specific to the present section, the selection of the surrogate model.

[8] Typical scaling processes ca be: root mean squares, log, normalisation, and so on.

Weight factors

As aforementioned, Kriging performs an estimation response $\hat{Z}(\bar{x}_o)$ at a new point $\bar{x}_o \in \mathbb{R}^p$ by realizing a linear combination of the training data $\bar{x}$ with respect to $\bar{x}_o$. Thus

$$\hat{Z}(\bar{x}_0) = \sum_{i=1}^{m} \lambda_i Z(\bar{x}_i) + \left(1 - \sum_{i=1}^{m} \lambda_i\right) m_z \tag{4.4}$$

where the first term represents the linear combinations of the training data with an associated weight λ_i. The second term is simply a correction that ensures the model is unbiased by forcing the estimation to the overall mean m_z if the sum of all weights is below 1. Recasting the above expression as residuals $(\hat{Y}(\bar{x}))$ will ensure the model is able to handle non-stationary[9]data sets. The residual is defined as the difference between the estimated response and the local mean $m(\bar{x})$ as

$$\hat{Y}(\bar{x_o}) = \hat{Z}(\bar{x}_o) - m(\bar{x}_0) \tag{4.5}$$

By reformulating eq. (4.4) with eq. (4.5), the following linear relation is obtained, where the correction term of eq. (4.4) is no longer necessary because it becomes implicit in the residual formulation.

$$\hat{Y}(x_o) = \sum_{i=1}^{m} \lambda_i Y(\bar{x}_i) \tag{4.6}$$

There are three properties that λ should consider, namely the closeness of the training data to $\bar{x}_o$, the consideration of the local density of training data also referred as redundancy and finally, the spatial continuity that accounts for the overall data arrangement in the space domain. In summary, it ensure the weights can offer unbiased predictions and minimise the prediction variance.

In order to derive weight factors with the aforementioned properties, the expected estimated variance is performed. The estimated variance is defined as the square of the estimated response minus the true response at the unknown location (for instance $\bar{x}_o$), as shown in the left hand side of the following expression. Furthermore, deriving the quadratic relation results in the right hand side, where eq. (4.6) is eventually fit in as the derivation goes on.

$$\begin{aligned}\mathbf{E}\{[\hat{Y}(\bar{x}_o) - Y(\bar{x}_o)]^2\} &= \mathbf{E}\{[\hat{Y}(\bar{x}_o)]^2\} - 2\mathbf{E}\{[\hat{Y}(\bar{x}_o)Y(\bar{x}_o)]\} + \mathbf{E}\{[Y(\bar{x}_o)]^2\} \\ &= \underbrace{\sum_{i}^{m}\sum_{j}^{m} \lambda_i\lambda_j \mathbf{E}\{Y(\bar{x}_i)Y(\bar{x}_j)\}}_{\text{Redundancy}} \underbrace{- 2\sum_{i}^{m} \lambda_i \mathbf{E}\{Y(\bar{x}_o)Y(\bar{x}_i)\}}_{\text{Closeness}} + \underbrace{\mathbf{E}\{[Y(\bar{x}_o)]^2\}}_{\text{Variance}}\end{aligned}$$

As it can be appreciated, three main terms can be distinguished labeled with underbraces. The first term involves a pairwise comparison of the training data with itself which basically screens for data redundancy, the second term involves a comparison between the training data with the new point. And finally, the third term is basically the variance of the estimated response (in residual form).

---

[9] In analytical statistics, stationary data is referred when the overall properties of the data set does not change when zooming into a subset of it, i.e. the mean of a small portion of the data does not change with respect to the overall mean.

Such pairwise comparisons are the same as performing the covariance [13], thus further simplifying the expression into

$$\begin{aligned}\mathbf{E}\{[\hat{Y}(\bar{x}_o) - Y(\bar{x}_o)]^2\} = &\sum_i^m \sum_j^m \lambda_i \lambda_j \mathbf{Cov}(Y(\bar{x}_i), Y(\bar{x}_j)) - 2\sum_i^m \lambda_i \mathbf{Cov}(Y(\bar{x}_o), Y(\bar{x}_i)) \\ &+ \mathbf{Cov}(Y(\bar{x}_o), Y(\bar{x}_o))\end{aligned} \tag{4.7}$$

The optimal weights are computed by performing the partial derivative with respect to the weight factor

$$\frac{\partial \mathbf{E}\{[\hat{Y}(\bar{x}_o) - Y(\bar{x}_o)]^2\}}{\partial \lambda_i} \qquad i = 1, 2, 3, ..., m$$

leading to a system of linear equations that expressed in matrix notation shall result in the following arrangement.

$$\begin{aligned}[C]\{\lambda\} &= \{C\} \\ \{\lambda\} &= [C]^{-1}\{C\}\end{aligned} \tag{4.8}$$

Where the matrix $[C]$ has entries $C_{ij} = \mathbf{Cov}(Y(\bar{x}_i), Y(\bar{x}_j))$ and the array $\{C\}$ has entries $C_i = \mathbf{Cov}(Y(\bar{x}_o), Y(\bar{x}_j))$. And $\{\lambda\}$ is the array of weights.

It should be clarified, that this kind of surrogate models becomes very expensive when large amount of training data are involved (order of thousands) basically due to the fact that the operations to compute the weights are realized for every point in the training data. Nevertheless, the current study does not suffer from such problem.

4.3.2 Sample size

The number of training points necessary for building the surrogate model is often, subject of study. Many authors attempted to draw a reasonable rule of thumb, however, with no positive results. Reality, showed that the amount of training data necessary to train the surrogate model are specific to the truth model's particularities. For instance, the level of noise in the response domain.

Nevertheless, many procedures have been explored in order to quickly learn the specifics of the problem. For the present case, the rudimentary but classic 'trial and error' approach is deemed enough. The initial size of training points obeyed from a sampling-based method rule of thumb, that recommends a sample size between 5 to 10 times the number of input variables, where the upper limit is chosen. The outcome resulted in 100 training points generated with the LHS method. After identifying the Pareto fronts, a second (and final) iteration was performed by inputting the hull members in the Pareto fronts into FAST-SHIP, in order to increase the local accuracy. The outcome of such step resulted in 85 additional points, thus, totalling 185 points as the final training data size.

Details concerning the Pareto fronts are further explained below.

4.3.3 Cross-validation

In order to ensure the surrogate model is correctly behaved, cross-validation procedures are typically performed as sanity checks. A standard cross-validation procedure for the surrogate models is to use only 80% of the training points to build the surrogate model and have it estimate the remaining 20%. The resulting predictions are then compared to the true data.

In this study, all the responses presented in section 3.2.3 are accounted. Namely the mean impulse J_{mean}, the maximum impulse J_{mean}, the 95-percentile impulse J_{95}, the maximum number of exceedances N_{exc}, the overall number of impulses simulated N_{imp}, the mean slamming velocity V_{mean} and the mean maximum slamming velocity V_{max}.
The error density distribution of the various responses along with its mean errors are computed, displayed in fig. 4.8. The mean error is computed as

$$\mathbf{Avg}(e) = \frac{1}{m}\sum_{i=1}^{m}\left(\hat{Y}(\bar{x}_i) - Y(\bar{x}_i)\right) \tag{4.9}$$

where m is the number of observations performed (20% of the training points). Furthermore, the the root mean square (RMS) errors are also computed, as applied by [9] in this kind of studies, formulated as

$$e_{RMS} = \sqrt{\frac{1}{m}\sum_{i=1}^{m}(\hat{Y}(\bar{x}_i) - Y(\bar{x}_i))^2} \tag{4.10}$$

Such error indicators can be found tabulated in table 4.4.

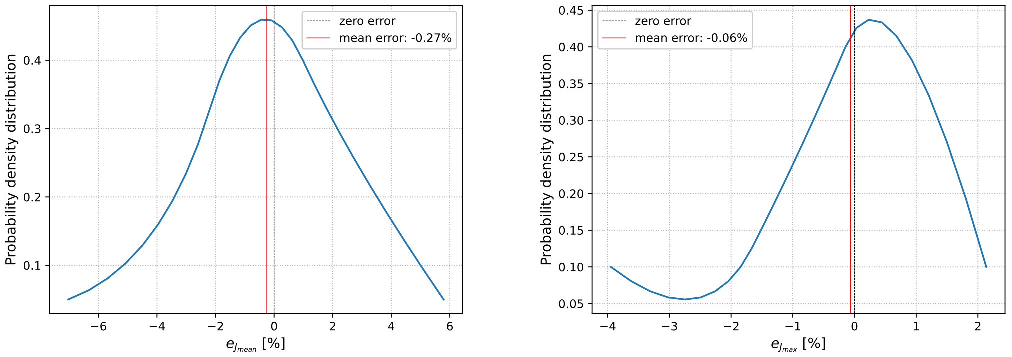

(a) Error density distribution of the mean impulse J_{mean} **(b)** Error density distribution of the maximum impulse J_{max}

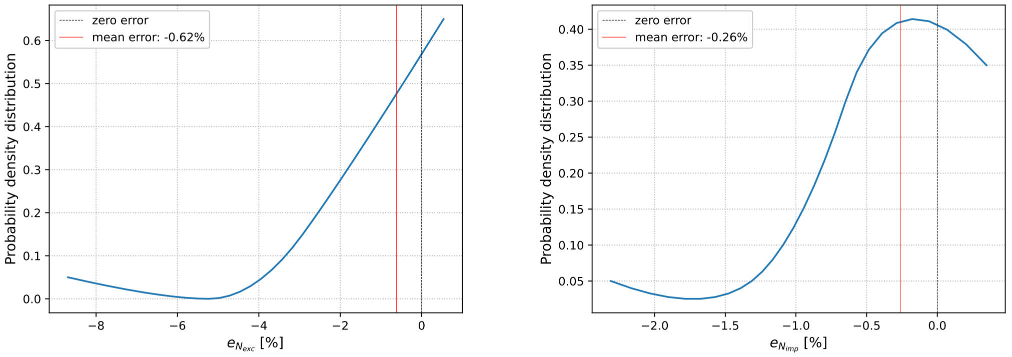

(c) Error density distribution of the maximum number of exceedances N_{exc} **(d)** Error density distribution of the overall number of impulses simulated N_{imp}

Figure 4.8: Part 1 of 2. Error density distribution of the various responses involved in the study.

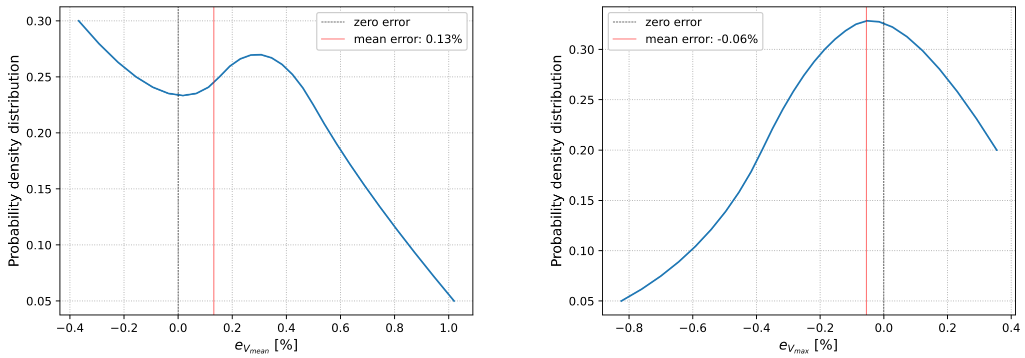

(e) Error density distribution of the mean slamming velocity V_{mean}

(f) Error density distribution of the maximum mean slamming velocity V_{max}

Figure 4.8: Part 2 of 2. Error density distribution of the various responses involved in the study.

Response parameter	**Mean e** [%]	$\mathbf{e_{RMS}}$ [%]
J_{mean}	-0.27	3.00
J_{95}	-0.32	2.00
J_{max}	-0.06	1.76
N_{exc}	-0.62	2.34
N_{imp}	-0.26	0.72
V_{mean}	0.13	0.44
V_{max}	-0.06	0.35

Table 4.4: Surrogate model cross-validation by computing the mean error and the root mean square error of the predicted responses with respected to the true model, expressed in percentage

As it can be appreciated, the error density distributions have different shapes, all of them displaying a mean error slightly shifted from the absolute zero error. Revealing the existence of a mean absolute 'miss-prediction' with respect to the true response within the surrogate model, where the majority of the responses are underpredicted, except for V_{mean}, which is slightly overpredicted. However, the magnitude of these errors are considered rather negligible since it systematically stays under 1%, thus the surrogate model predictions can be deemed acceptable on this regard.
Considering the various error density distributions, except for N_{exc} and V_{mean} (figs. 4.8c and 4.8e respectively), the rest follows a Gaussian-like distribution (figs. 4.8a, 4.8b, 4.8d and 4.8f), which is expected and deemed positive. Regarding the non-Gaussian-like distributions, the N_{exc} error distribution can be actually seen as a half Gaussian-like distribution and the error deviations (horizontal axis) of the V_{mean} error distribution are very small. Thus, no alarming behaviours are discerned.
Focusing on the RMS errors, as it can be appreciated in table 4.4 the largest error recorded has a 3% deviation, corresponding to J_{mean}. Thus, no alarming behaviours are discerned neither.

In conclusion, the estimations of the surrogate model are considered to be close enough to the true responses and thus, satisfactory. Therefore, the surrogate model is deemed trustworthy enough.

4.3.4 Pareto fronts

Once the surrogate model is validated, mass production of hull forms can be generated with the sampling method chosen in section 4.2 (LHS) and evaluated inexpensively by the surrogate model, populating every corner of the response domain.

In multi-objective procedures, often a trade-off may arise between the involved objective functions because a non-linear correlation[10]amongst the various pairwise comparisons exist, quantified as $\neq 1$. When such one-on-one objective comparisons does not display a clearly dominant point (no single point simultaneously optimizing all objectives), the objective functions are said to be conflicting, creating a multi-level space known as the Pareto front. Hulls within the Pareto front will thus, show singular properties that cannot be outperformed by each other.

From the responses considered in the research, the main response is the mean impulse J_{mean}, thus only pairwise comparisons with J_{mean} are relevant. As concluded in section 4.1, a linear relation with J_{max} and J_{95} was obtained, therefore, such relations are deemed irrelevant. Furthermore, the relation of J_{mean} with the mean maximum slamming velocity V_{max} is also deemed linear fig. 4.9, hence also insubstantial and thus, ignored as well.

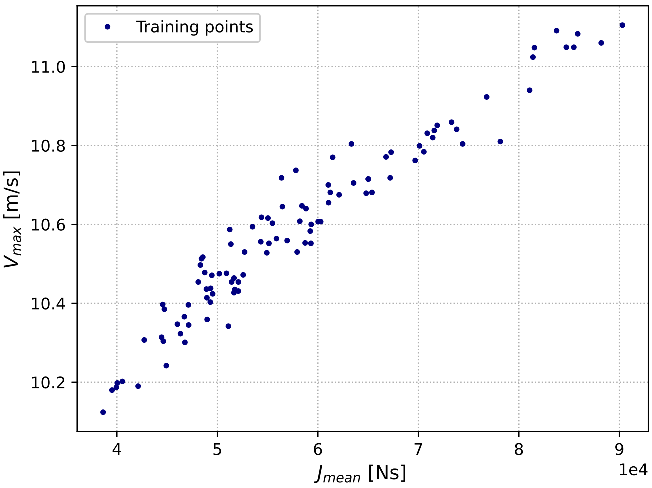

Figure 4.9: Correlation plot between two responses, J_{mean} and V_{max}. The correlation coefficient is $\rho = 0.97$, revealing a practically linear relation between the two responses.

The relations that resulted in a discernible competition are: J_{mean} vs. N_{exc}, J_{mean} vs. N_{imp} and J_{mean} vs. V_{mean} (shown below). Therefore, main focus will be considered for these relations. Before going any further with the research, a Pareto front validation procedure is carried out in order to ensure result consistency, explained next.

Pareto front convergence study

To ensure the Pareto fronts are independent from the sample size, a Pareto front convergence study is performed, by systematically increasing the population size until the Pareto fronts consistently stayed at the same location in the domain.

---

[10] Such correlation refers to the Pearson correlation coefficient ρ, defined as the covariance of the two involved variables divided by the product of their standard deviations. The correlation can range from -1 to +1, where 0 means the relation is completely non-linear. Thus, a correlation of $|\pm 1|$ denotes a linear correlation with either positive or negative slope.

The considered population sizes were 20, 40, 80 and 120 thousand. Depicted in fig. 4.10, the Pareto fronts of the considered relationships are displayed for the different population sizes, along with the training points.

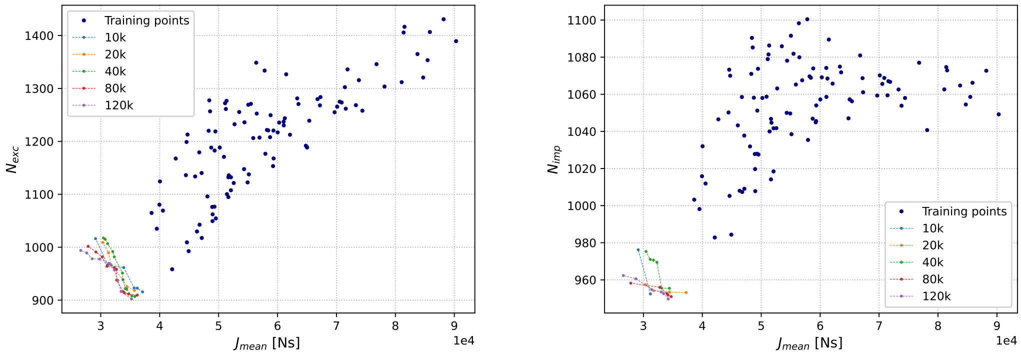

(a) Correlation plot between two responses, J_{mean} and N_{exc}. The correlation coefficient is $\rho = 0.79$

(b) Correlation plot between two responses, J_{mean} and N_{imp}. The correlation coefficient is $\rho = 0.42$

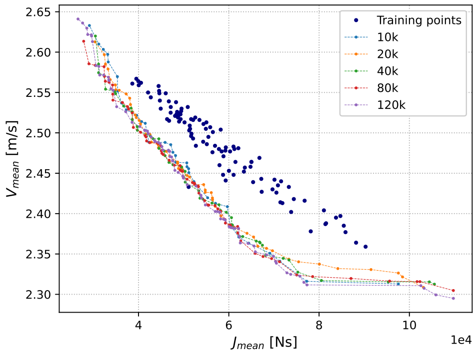

(c) Correlation plot between two responses, J_{mean} and V_{mean}. The correlation coefficient is $\rho = -0.96$

Figure 4.10: Pareto front convergence analysis based on the surrogate model predictions, which training points are shown. The tested populations sized are 10, 20, 40, 80 and 120 thousand.

Convergence was appreciated at 120 thousand hulls, thus no further population size was considered.

4.4 Results

Once the surrogate model is properly validated and the required hull population size to ensure a consistent Pareto front established, the surrogate model can be used with confidence. In this section the hulls contained in the Pareto fronts will be analysed. Furthermore, the trend of the hull characteristics from the sub-optimal regions towards the Pareto-optimal regions will also be discussed.

In fig. 4.11, the final population size generated by the surrogate model for the concluded multi-objective comparisons presented in the previous section are displayed. The Pareto fronts of each correlation are highlighted in red, and next to them, an analogous plot highlighting the Pareto front of the other correlations, thus exhibiting the relation of the various Pareto fronts amongst each other. Moreover, the training points are represented by the blue dot markers and the reference hull, the 4212, with a yellow star marker.

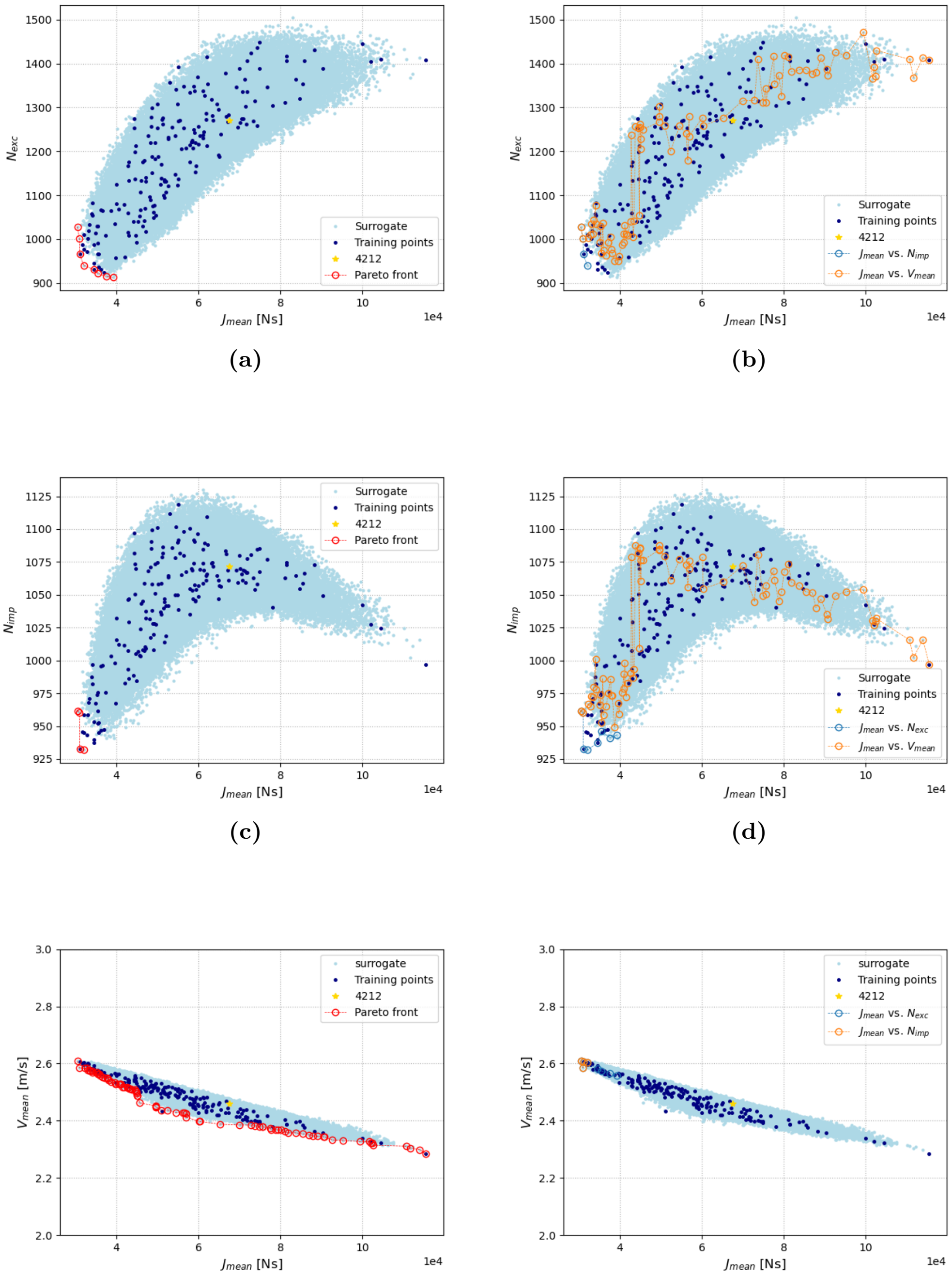

(a) (b)

(c) (d)

(e) (f)

Figure 4.11: Illustration of the hull population generated by the surrogate model, with the various Pareto fronts correspondingly highlighted. On the left column of plots, their own Pareto fronts and on the right column the Pareto fronts of the others.

As it can be appreciated, the J_{mean}—V_{mean} plot has the largest Pareto front, practically covering the entire J_{mean}-space domain, which seen from the other correlations, the majority of the hulls falls into the sub-optimal performance regions (where hulls are dominated by the neighbouring). Furthermore, the V_{mean} range is actually quite small ($V_{mean}^{max} - V_{mean}^{min} = 0.32$ m/s), see fig. 4.11e. Thus, according to the plot, the hulls at

the left-most side and right-most side of the J_{mean} axis have fairly similar V_{mean} values. However, since the hulls within the upper-left region of such Pareto front are quite close to the Pareto region of the other correlations, it is considered pertinent to keep such front, because it shines more light to the region and can add a better insight of the hull seakeeping performances.
Meanwhile, the Pareto fronts of the J_{mean}—N_{exc} and J_{mean}—N_{imp} plots are fairly close to each other, thus both objectives tends to converge towards the same region. Furthermore, they even share some hull members.

In order to understand the geometrical characteristics of the hulls contained in the Pareto front, the classical parameters used in the naval architecture field to describe the hull shape are utilized. Furthermore, in order to visualize the performance trend based on such parameters, an analysis from the hulls located in a sub-optimal region to the hulls contained in the Pareto-optimal region are explored. Upon the consideration of different ways of performing such endeavor, it is finally decided to perform the analysis to the hulls contained in the contour of all three correlations of fig. 4.11, as illustrated in fig. 4.12. The contours are identified by computing all four Pareto fronts of each correlation, corresponding to the four respective corners of the plots. The reason of such choice is due to the singularity each individual hull in the contour has, which in some way, outstands from hulls contained in the middle of the cloud of points, for instance.

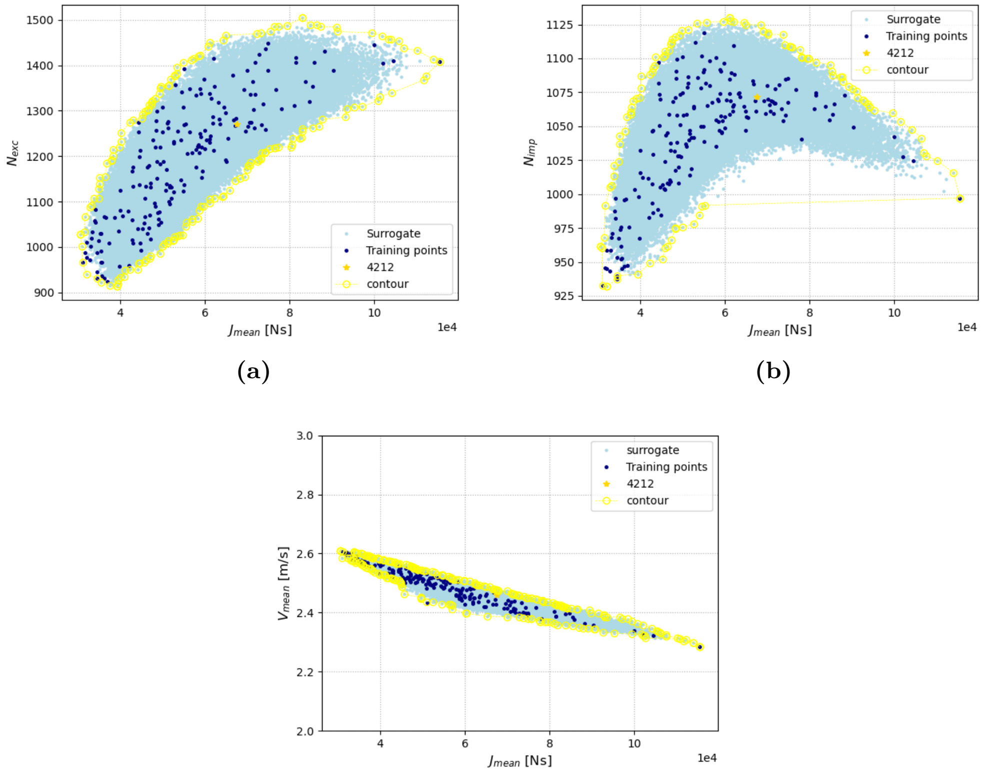

(a) **(b)**

(c)

Figure 4.12: Illustration of the contours obtained by identifying the Pareto fronts of the four quadrants of the various considered correlations build by the surrogate model.

To display the various hull characteristics, the contours are 'flattened' along an horizontal axis, similar to an equirectangular projection (i.e. a cartesian 2D map with the latitudes and longitudes parallel to the corresponding rectangular edges). In fig. 4.13, an illustration of the procedure can be found for better understanding. By applying such post-processing step, the hulls contained in the contours are ordered in an identical fashion. The evaluation system starts at the right-most point of the contour and moves in counter-clockwise direction until reaching the initial position again.

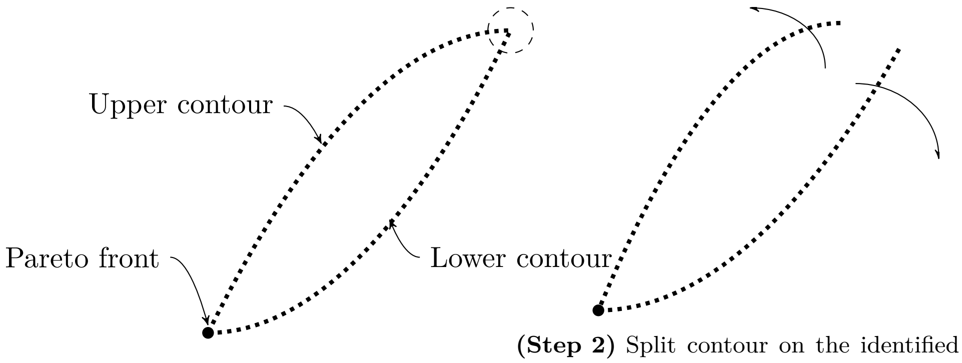

(Step 1) Identify the right-most points of the upper and lower contour

(Step 2) Split contour on the identified point from previous step and spread it. Upper contour to the left, lower contour to the right

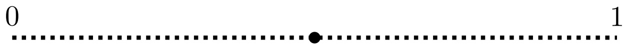

(Step 3) Flatten the contour and normalize it from 0 to 1. The right-most point of the upper contour becomes the 0 (starting) position and the right-most point of the lower contour becomes the (final) position 1

Figure 4.13: Illustration of the plotting procedure of the contours identified in the surrogate model produced correlation plots.

For instance, considering the contour of fig. 4.12c, once applied the process explained in fig. 4.13, any hull characteristic can be measured and displayed in a secondary (vertical) axis, where the first measured quantity shall correspond to the hull in the normalised position 0, and systematically proceding until reaching the last hull, corresponding to the normalised position 1.

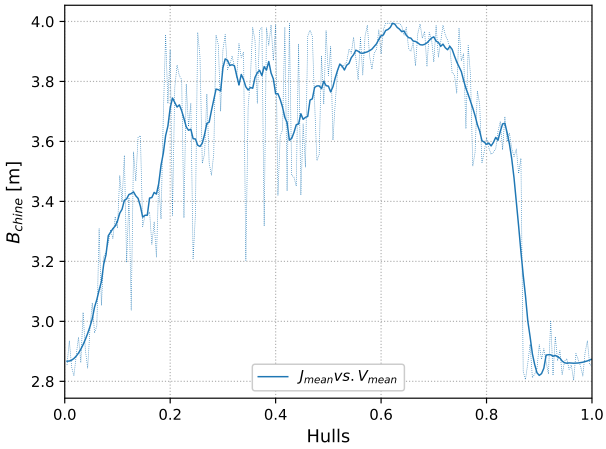

Figure 4.14: Example of a contour evaluation, displaying the unfiltered and filtered trend.

For the sake of explanation, in fig. 4.14 the maximum beam at the chine B_{chine} is evaluated (see section 2.2.3 for context). By connecting the B_{chine} of each hull, a curve is obtained which turned out to be rather noisy (illustrated with the dashed curve), thus the Savitzky–Golay filter (a low pass filter) is applied in order to discern the trend.

Such methodology is systematically applied for all three contours, and different parameters describing the hull shape are explored. The utilized parameters to describe the hull geometry are introduced in section 4.4.1, categorised in: dimensions, ratios and coefficients.
Furthermore, the Pareto fronts of each contour are highlighted with a thicker line and the equivalent parameter of the 4212 marked with a horizontal dashed line.

4.4.1 Hull geometry trends

The trends of the various parameters describing the hull geometry are presented here. As it will be seen, the general trend is towards bulkier forms. However, some parameters showed an intermediate position in-between the trend extremes, denoting a weaker influence on the wet deck slamming.

4.4.1.1 Dimensions

The hull dimensions refers to the directly quantifiable aspects of the hull geometry, some of them related to the parametric hull model for FASTSHIP (see section 2.2.3). Such considered dimensions namely are: the propulsion clearance form factor α, the maximum beam at the chine B_{chine}, the maximum beam at the wet deck height B_{deck}, the dead rise angle β, the height of the keel-bow connection H_{keel} and the angle of attack of the waterplane area θ. Discussed next.

$\underline{\alpha}$

Starting with the propulsion clearance form factor α, first, an illustration of the effect of such parameter to the hull shape is displayed in fig. 4.15. As it can be appreciated, it varies the volume at the aft, directly affecting the space destined for the propulsion device (i.e. propeller, waterjet, etc.). A low value of α translates into larger aft volume and less propulsion space and viceversa.

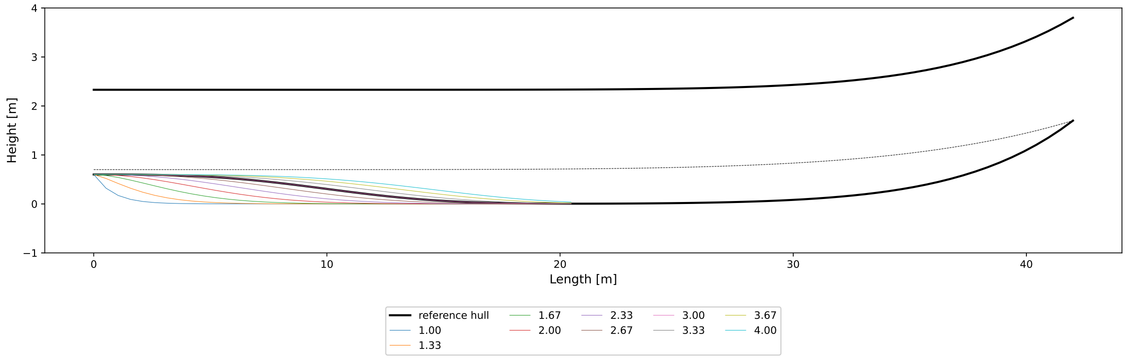

Figure 4.15: Illustration of the effect of the propulsion clearance form factor α, by displaying the resultant shape of various values.

According to the study (fig. 4.16), the hulls with poorer performance have higher α values (bigger clearance), close to the reference hull, at $\alpha = 3$. As it can be appreciated, the thick lines (representing the Pareto fronts) falls between the aforementioned value and

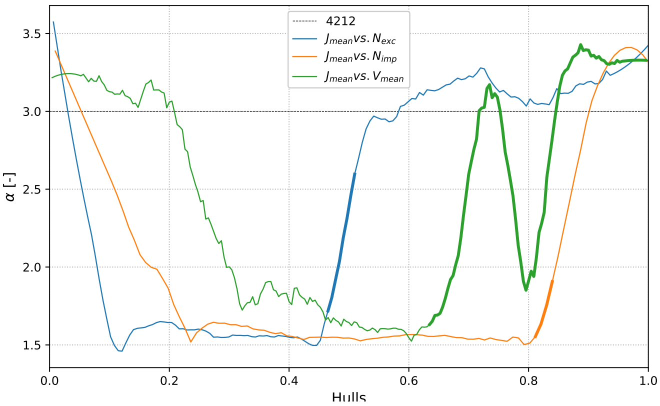

Figure 4.16: Contour evaluations of α.

a distinguishable lower limit of $\alpha = 1.5$. Although the results does not point towards a clear trend, it can be still concluded that a lower α, between 1.5 and 2.5, is preferable.

B_{chine} & B_{deck}

The FFC's demihull maximum breadths are determined by the breadth parameters B_{chine} and B_{deck}, representing the beams at the chine and wet deck (height) respectively. Which trend are plotted in fig. 4.17 and fig. 4.18 respectively.

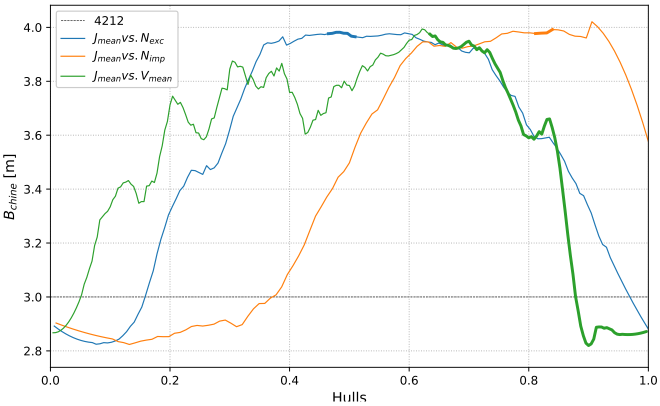

Figure 4.17: Contour evaluations of B_{chine}.

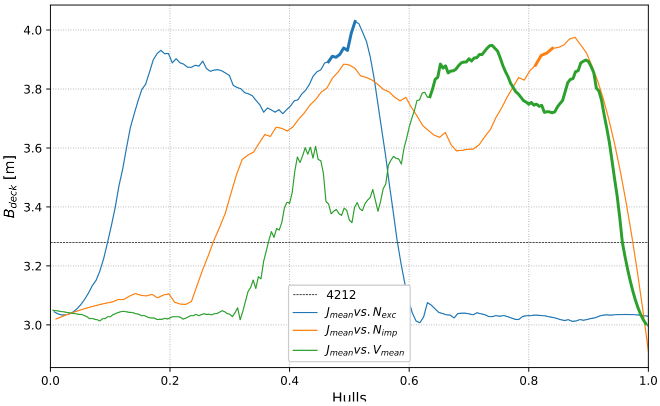

Figure 4.18: Contour evaluations of B_{deck}.

According to the plots, the Pareto fronts of both parameters tends to be located at the upper limit, indicating the trend towards wider demihulls than the 4212. Thus, buoyancy is increased.

β

The dead rise angle β is a parameter that may vary drastically from aft to bow, thus an evaluation is performed at 4 different locations along the hull length, for each of the hulls contained in the contours. Namely at 0%, 25%, 50% and 75% of the LOA, with respect to the transom.

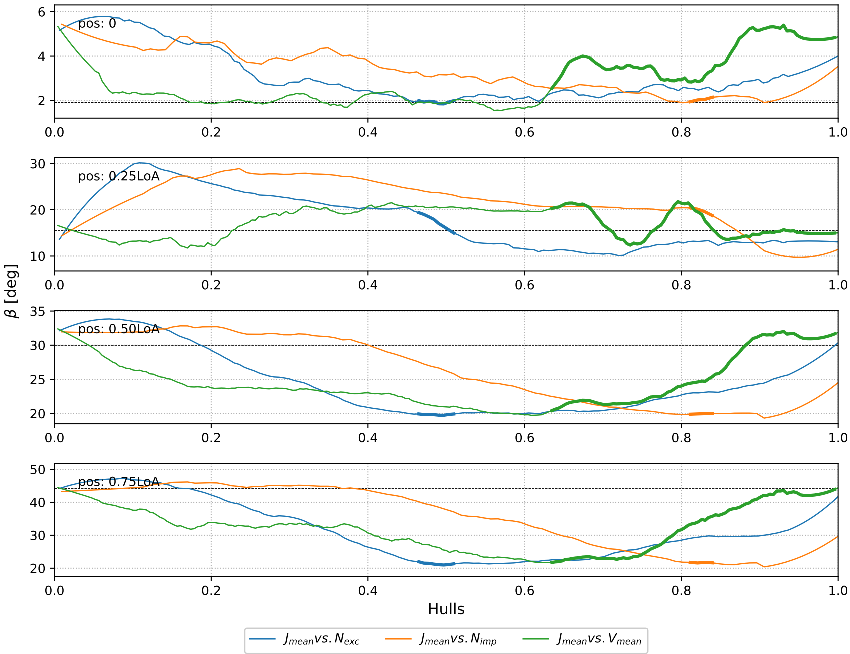

Figure 4.19: Contour evaluations of β.

As displayed in fig. 4.19, the general trend is toward smaller dead rise angles, particularly at the fore-half of the hull. Compared to the reference hull, the dead rise angles at the aft-half does not deviate much from, thus it is inferred that the dead rise angles at the fore sections have more influence on the overall wet deck slamming performance than the aft sections.

H_{keel}

The height of the keel-bow connection H_{keel} affects the shape of the bow, fig. 4.20 illustrates the effect of such parameter to the hull form for a better understanding.

As it can be appreciated, the resultant bow geometry may vary from an Axe-bow-like to the classic flared bow type.
Looking at design trend, fig. 4.21 shows that dragging down the keel-bow connection leads to wet deck slamming reduction. According to the figure, the optimal range stays between 0 and 0.5 m (with respect to the baseline). Thus, the design trend is somewhere in-between an Axe-bow-like and a flared bow.

θ

The angle of attack of the waterplane area in the present research is denoted as θ. Since the hull geometry is parametrized, θ is computed by performing the fist derivative of the

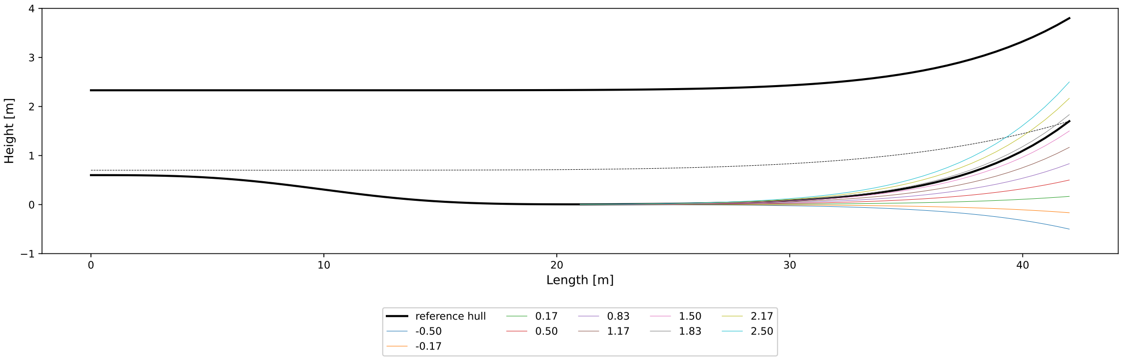

Figure 4.20: Illustration of the height of the keel-bow connection H_{keel}, by displaying the resultant shape of various values.

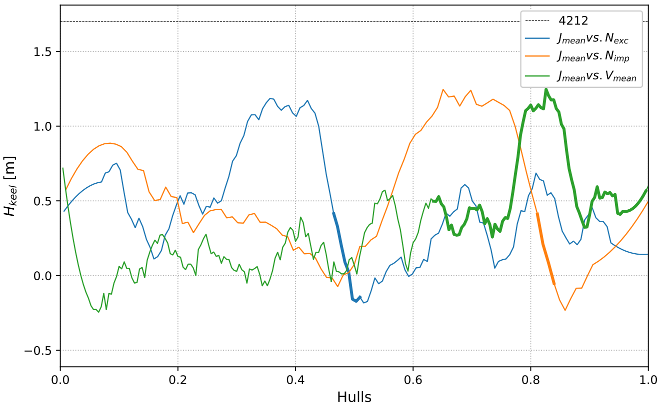

Figure 4.21: Contour evaluations of H_{keel}.

waterplane area contour. Based on fig. 4.22, θ has to increase in order to reduce the wet deck slamming.Furthermore, it can be appreciated how the Pareto fronts falls at the upper limits of the trends. Where the maximum attained angle of attack values reaches the 24 degrees. Such measure will surely increase the wave making resistance.

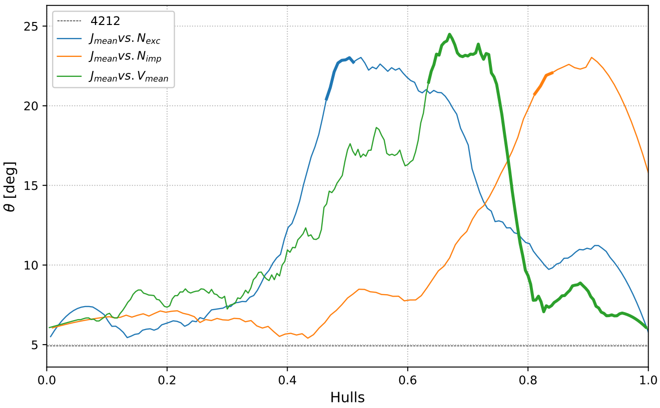

Figure 4.22: Contour evaluations of θ.

4.4.1.2 Ratios

The ratios refers to the relation between two geometrical hull parameters. In the naval architecture field, such relations often follows from empirical rules or general trends that engineers commonly use to describe not only the hull shape but even its performance, in a non-dimensional manner. Roughly used for the comparison with other hulls or just quick understanding.

In the present research, the following rations have been inspected, namely the relative position of the LCF with respect to the LCB, modelled as

$$\frac{LCF - LCB}{LOA}$$

a ratio related to the coupling between the heave and the pitch, and lastly the B over T rations of both, at wet deck level and at chine level, respectively

$$\frac{B}{T} \quad , \quad \frac{B_c}{T_c}$$

informing about the stability performance in the case of monohulls but in the present case, hull slenderness. Such relations are plotted in figs. 4.23 to 4.25 respectively.

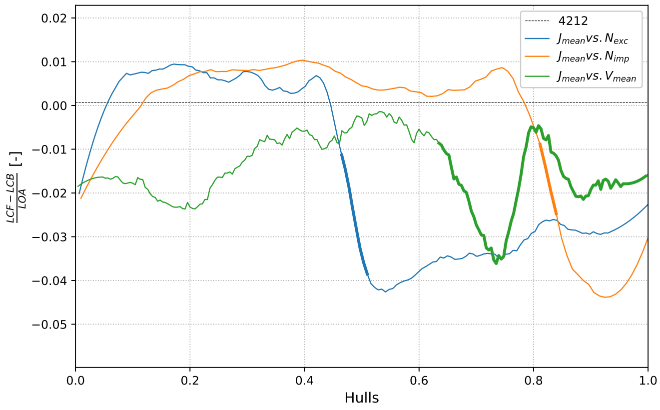

Figure 4.23: Contour evaluations of the LCF position relative to LCB.

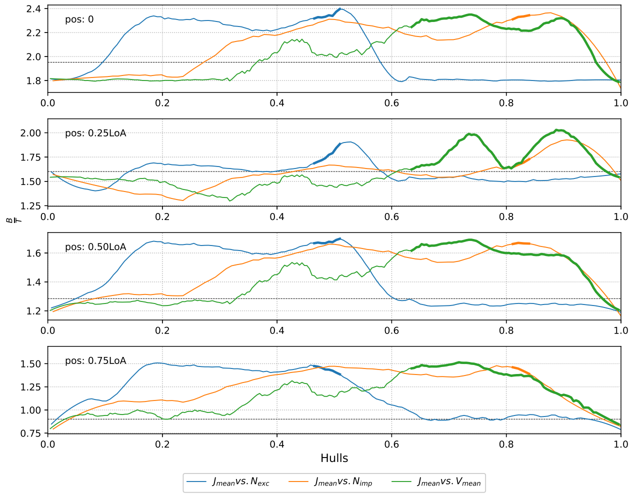

Figure 4.24: Contour evaluations of B/T ratio at the wet deck level.

According to the results, and in concordance with the trends of the previous section, the design tonality moves towards wider or bulkier forms. Thus, the B over T ratios tends

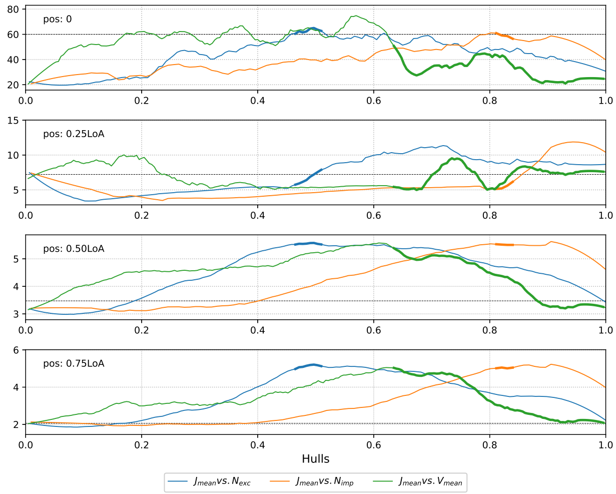

Figure 4.25: Contour evaluations of B_c/T_c ratio at the chine level

to be higher than the reference hull. Furthermore, the ratios are systematically computed in four locations along the hulls contained in the contour, namely at 0%, 25%, 50% and 75% of the LOA, with respect to the transom, as appreciable in figs. 4.24 and 4.25. Regarding the LCF position, the general trend is to move it aftwards, although the Pareto fronts does not falls into the lowest limit, rather it stays in between. Namely between 1%—4% towards the aft.

4.4.1.3 Coefficients

The coefficients refers to the common non-dimensional quantities used in naval architecture, namely the block coefficient, the prismatic coefficient and the waterplane area coefficient, denoted as C_b, C_p and C_w respectively. These coefficients indicates the volume distribution across the length of the hull, and informs about the hull slenderness. Since such parameters just describes the general hull shape, details cannot be inferred solely based on these quantities. Nevertheless, it provides a general trend, thus general design walls.The contour trends of C_b, C_p and C_w are illustrated in figs. 4.26 to 4.28 respectively.

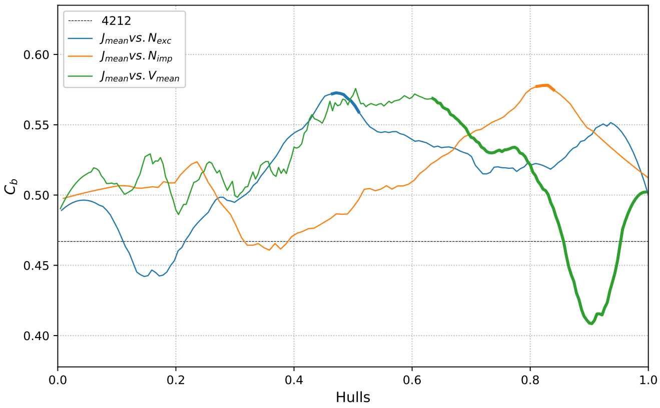

Figure 4.26: Contour evaluations of C_b.

As expected, the general trend of all three coefficients moves towards bulkier forms, thus higher coefficients.

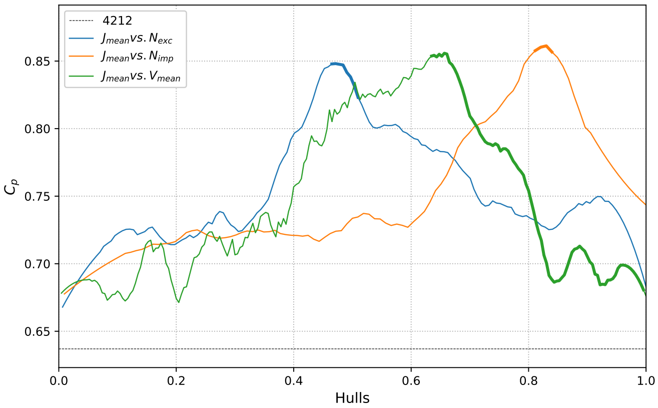

Figure 4.27: Contour evaluations of C_p.

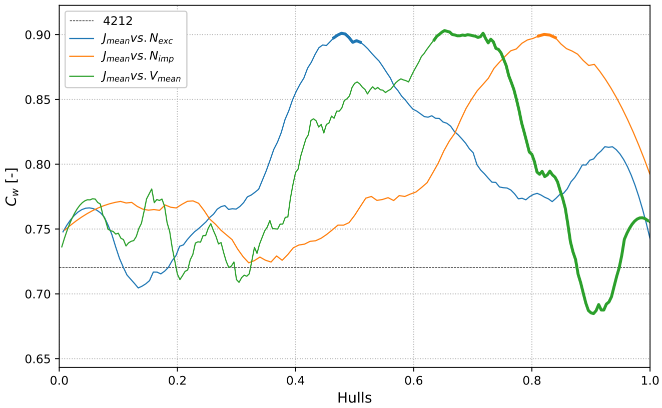

Figure 4.28: Contour evaluations of C_w.

In summary, the hulls within the various Pareto fronts corresponding to the correlations of J_{mean}—N_{exc}, J_{mean}—N_{imp} and J_{mean}—V_{mean} have been analyzed. Furthermore, in order to display the trend of the hull characteristics from sub-optimal wet deck slamming performance to Pareto-optimum region, the contours of the built correlations are considered. The analysis is achieved by applying the post-processing step described in fig. 4.13.

The results revealed that generally bulkier forms minimises all the above mentioned objective functions. The details concerning the local geometries of the hull will depend on the user's necessities since a trade-off exist within the optimum region (hence, the existence of the Pareto front).

By achieving the results presented in this chapter, it is concluded that the analysis of wet deck slamming on catamarans sailing in head waves can be reduced to its demihull only, offering a valuable design tool for the naval engineering field, wanting to perform a relatively fast and simple seakeeping and wet deck slamming evaluation.

Further plots displaying the above presented results in a different format can be found in Appendix B.2.

4.4.2 Hull lines

In the present section, a comparison between the hull lines of the reference hull (4212) and a representative of both, a hull within the sub-optimal region and a hull within the Pareto-optimal region, of the above presented multi-objective space is realised.

The comparison is realised by displaying the difference in the main hull lines of the demihulls, namely the keel, chine and deck profiles, from two different views, side and top view. Furthermore, 3-dimensional views of the corresponding representative hulls are also shown.

Sub-optimal hull

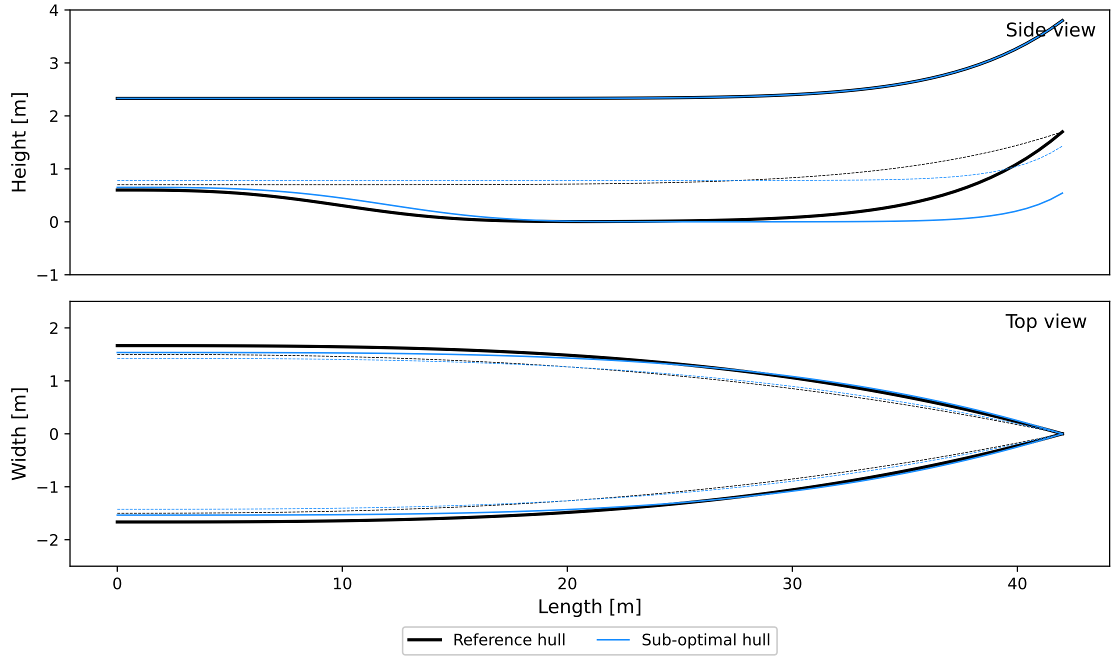

Figure 4.29: Hull line comparison between the reference hull (4212) and a random hull in the sub-optimal region of the considered multi-objective space.

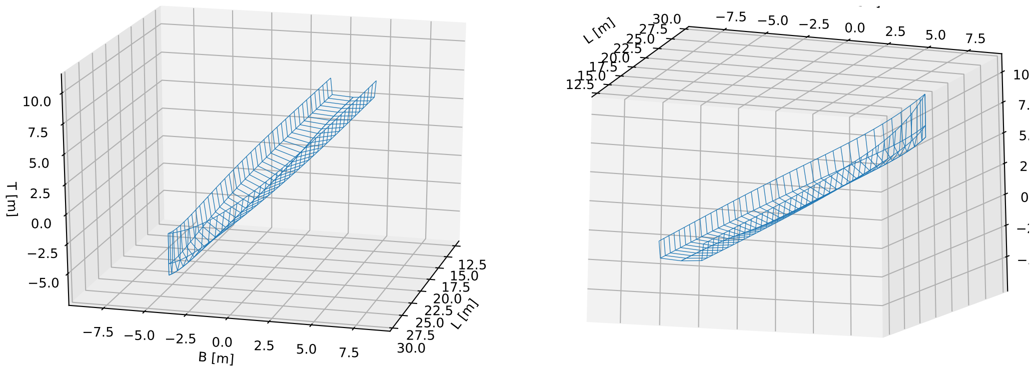

(a) Bird view

(b) Fish view

Figure 4.30: Part 1 of 2. 3D view of a random hull in the sub-optimal region of the considered multi-objective space

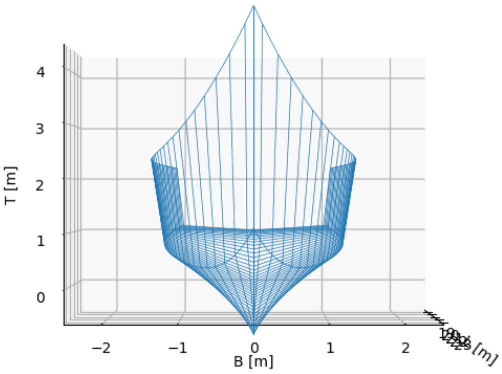

(c) Front view

Figure 4.30: Part 2 of 2. 3D view of a random hull in the sub-optimal region of the considered multi-objective space

Pareto-optimal hull

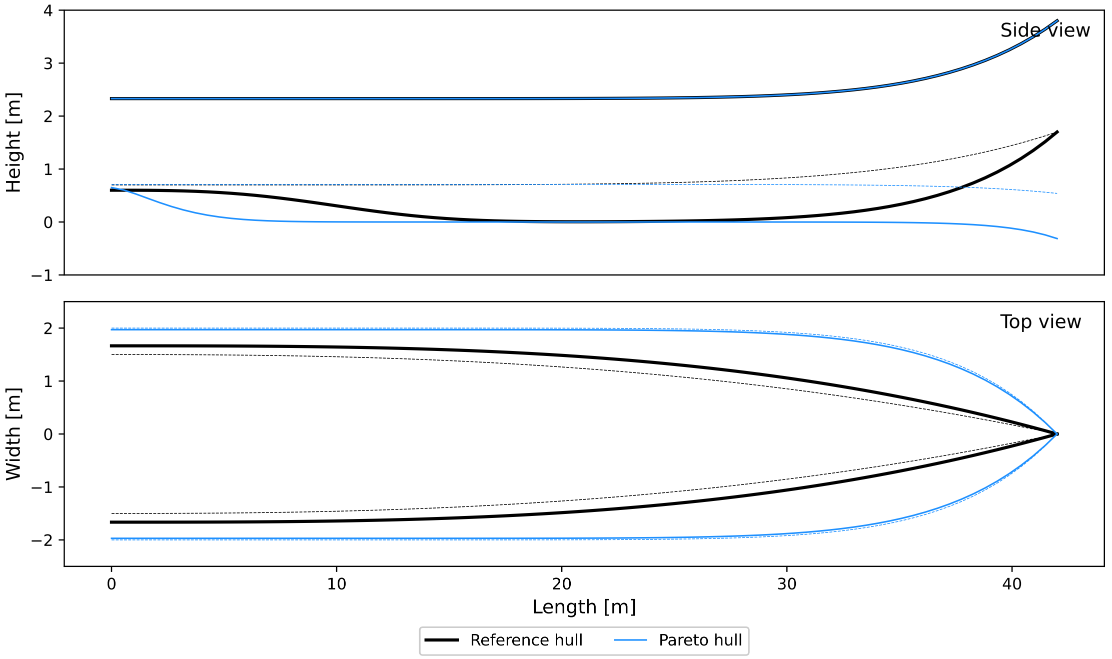

Figure 4.31: Hull line comparison between the reference hull (4212) and a random hull in the Pareto-optimal region of the considered multi-objective space.

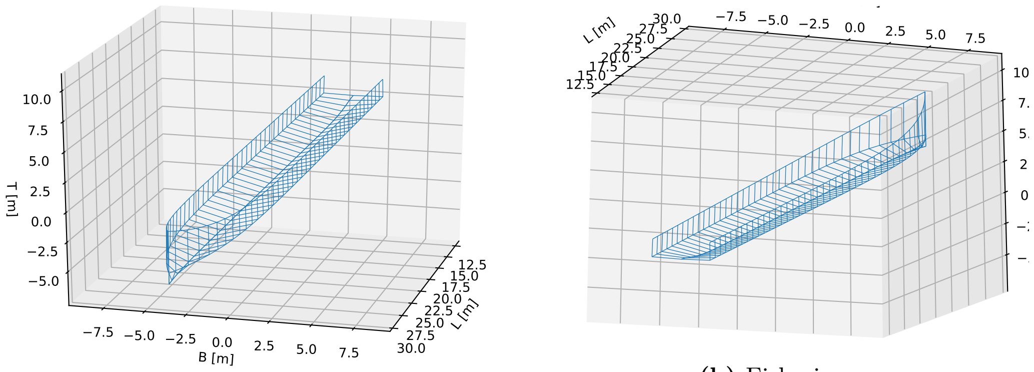

(a) Bird view

(b) Fish view

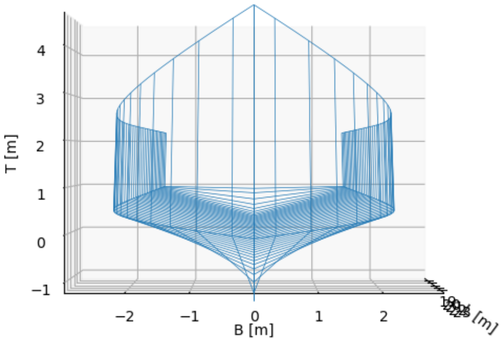

(c) Front view

Figure 4.32: 3D view of a random hull in the Pareto-optimal region of the considered multi-objective space

5

Optimisation

Optimisation in the DOE context is the application of a numerical methodology to either maximize or minimize a given objective function $f(\bar{x})$, which domain is accessed through a p-dimensional vector $\bar{x}$ of real-valued design variables or design parameters $x_1, x_2, ..., x_p$. Each parameter can be bounded by an upper and lower limit, thus defining the boundaries of the searching space, also referred as design space or parameter space. Moreover, optimisation can be performed with additional constraints that sets further numerical boundaries (otherwise, classified as unconstrained). These additional constraints can be categorized as either linear or nonlinear, and within such categories further distinction could be made based on either the equality or inequality of the constraint(s) condition. Moreover, objective functions can also be distinguished between linear or non-linear. Typically, optimisation problems with nonlinear objective functions require more computational resources, as the amount of calculations and iterations in order to infer the response space are larger. Furthermore, when coupled with an equality constrain, complexity increases as the searching space becomes narrower, meaning there are more penalties to avoid during the search. Therefore, it is common practice to reformulate the problem into a simpler form with linear and inequality characteristics.

There are several optimisation methods, depending on the problem's specifics, one may look for special attributes that can exploit these specifics. According to [1], besides the aforementioned categorisation criteria, optimisation methods can also be classified by the searching goal or the searching method. The searching goal refers to the ultimate objective of the optimization algorithm, either global or local best solution(s). And searching methods refers to the mechanisms to achieve such goals, classified into gradient-based local methods, derivative-free local methods or derivative-free global methods, described next.

> **Gradient-based local methods:** Gradient-based optimizers are optimisation methods that navigates through the response space by performing spatial differentiations or additionally Hessians. The most convenient way to manage such information is to directly provide it to the optimisation scheme (because they are available). However, this is not often the case, to which typical analytical procedures such as the forward-difference or central-difference schemes can be used.
>
> These optimizers are fast and efficient for local searches, provided that the response

surface is sufficiently smooth and that the starting point is close to either the local minima or maxima. Otherwise, rough or noisy surfaces can lead to inefficient or wrongful searching behaviors. Furthermore, they are generally less expensive to perform, although these kind of optimisation methods do not cope well with global searches, because they do not have escaping protocols when a local minima is found.

Derivative-free local and Derivative-free global methods: Derivative-free methods do not require the computation of any spatial differentiation, although it can be used in combination of a gradient-based techniques for extra robustness and flexibility. Nevertheless, these type of methods requires more computational resources in order to populate the design space to screen the response surface (of the order of hundreds to thousands of function evaluations), thus the rate of convergence is generally slower then the above mentioned method. However, derivative-free methods are more robust against non-smooth response surfaces and the best alternative against unfeasible, unreliable or expensive gradient-based approaches. Furthermore, the nature of such scheme allows for better performance with multi-objective oriented optimisation and may even allow for concurrent computation, thus decreasing the computational time.
Derivative-free methods can be further distinguished by the search goal, either local or global. As the name infers, each method screens the response surface at different scales.

In the present case, the goal of the optimisation is to screen for the global minimum across the p-dimensional design space, where the hulls with the lowest response attributes introduced in the previous chapters are found (translating into less potential slamming). According to the DOE study, a trade-off between the different considered responses exists, thus search of a local minimum is deemed unnecessary since there is no such thing as the single best hull geometry. Therefore, a derivative-free global optimisation method is deemed appropriate for the present research. Furthermore, the present problem is classified as bound-constrained, since only upper-lower boundaries per design parameter are specified in the problem[11].

Within the derivative-free global methods two methods are considered, brute force optimisation and Multi-Objective Genetic Algorithm (MOGA), both coupled with the surrogate model introduced in section 4.3, making the wet deck slamming evaluations practically inexpensive. The first method is thus renamed as Brute Force Surrogate-based Optimisation (BFSO). Both methods applies different approaches to find the optimum region, and depending on the user necessities one might be more convenient than the other. Nevertheless, both are discussed in the present work.

The BFSO method shares a lot of commonalities with the applied DOE methodology described in chapter 4, given the performed brute force search to explore the design space, which ultimately lead to the finding of the Pareto front. As a matter of fact, both methods leads to the same outcome but differs on the intention, since the applied DOE study pursued amongst others, the extraction of knowledge and data trend from sub-optimum regions to Pareto-optimum regions of the design space whereas BFSO would only care about the information contained in the Pareto front.

Regarding to the MOGA method, it is decided to couple the surrogate model to an evolutionary-based algorithm method because of the inexpensive built and also as a mean

---

[11] As a matter of fact, the optimisation problem is actually linear with inequality constraints (for some of the input parameters) but a redefinition of the input parameters was carried in order to indirectly comply with such constraints. Thus the corresponding constraints were implicit in the problem formulation.

of cross-validating the first-mentioned method with a full global-search-oriented method, which does not requires human interaction (unlike BFSO).

In the present chapter, the BFSO and MOGA methods will be described and the corresponding results compared.

5.1 Brute Force Surrogate-based Optimisation

Brute force optimisation explores every single possible solution within the response domain, it does not strategies the available resources, instead, it exploits it until a solution or stopping criteria is met.
Such method is typically applied in small problems or small and controlled response surfaces. Moreover, it could also be used in problems with a poor understanding of the design space, where a complex relation between the various involved (input) parameters exist.

Hence, brute force-based methods can become really expensive, however, when a surrogate model is involved in the evaluation of the objective function the cost of the corresponding computations becomes practically insignificant. The complete procedure and results of BFSO are reflected in chapter 4, where the following steps can be summarised for easy comprehension, provided the surrogate model is already obtained.

1. Populate the design space with a sampling-based method and evaluate response with the surrogate model.
2. Ensure the Pareto front is independent from the sampled data size.
3. Proceed to identify the resultant Pareto front based on the previous step.
4. Analyse the members of the Pareto front.

As aforementioned, see chapter 4 for further details and results.

5.2 Multi-Objective Genetic Algorithm

Multi-Objective Genetic Algorithm (MOGA) is an evolutionary-based algorithm based on *Darwin's* theory of survival of the fittest, oriented to the global search of Pareto fronts. The synopsis of the theory states, amongst others, that *"those individuals with heritable traits better suited to the environment will survive"*. Thus, the concept of fitness is introduced, interpreted as a score that enables the distinction between design points $\bar{x}_m$ contained in the design space, $\bar{x}_m \in \mathbb{R}^p$ from a population of size m. The design point $\bar{x}$ is the analogous of a DNA in a biological system, and the input parameters $x_1, x_2, ..., x_p$ contained in it, the genes. The best design points in the population (typically those having low objective function values) are considered to be the most "fit" and are allowed to survive and reproduce [1]. The normal convention is to attribute the highest score to the best design point and the lowest score to the worst design point.

The key component in the genetic algorithm success is its stochastic approach, a mechanism that enables the algorithm to have an escape route when convergence is going towards a local minima thus, ensuring the global minima is thoroughly searched.
The MOGA procedure starts with an initial population of m number of design points, which can be generated with a stochastic-based method or with a user defined distribution scheme. Each design point is evaluated and a fitness score is assigned according to its performance (based on its objective function value(s)). Amongst the best design points,

different evolutionary-based processes can be applied in order to generate $< m$ number of points, that will substitute the current worst design points. Thus, giving birth to a new 'generation'. New generations will be sequentially produced until the solution has been reached or a stopping criteria is met.

The biological-inspired processes to produce new points are namely crossover and mutation, both methods can be interpreted in different manners, thus different subvariations can exist. Nevertheless, both follows the same principles explained next.

> **Crossover** is based on the combination of the best genes between two (or more) design points from the fittest amongst the population. Analogous to the biological process of two parents producing an offspring.
>
> **Mutation** is based on the appearance of a random perturbation within a design point by randomly modifying an input parameter by either adding or subtracting a random quantity, thus implementing a stochastic mechanism. Such process ensures gene variety and artificially avoids premature convergence due to the breeding between similar individuals within the population.

The application of MOGA is carried by means of the software DAKOTA, where further and detailed information about the computational mechanisms can be found [2].

5.3 Performance comparison

The differences between the two considered global-search derivative-free optimisation methods above mentioned will be discussed in this section.

Given the fact that both methods relies on a surrogate model to perform the objective function evaluations, in terms of computational cost both methods are equally inexpensive and no substantial difference can be withdrawn. Amongst the various tests performed in the present research, both methods were systematically completed within $30s$. Hence, to the user, any difference is negligible. Furthermore, both methods reached the same multi-objective space, that is, the same Pareto front.
Nevertheless, a quantitative comparison based on the amount of design points required in both methods can be realised, in order to extrapolate the computational cost, in case the true model were used instead of a surrogate model. BFSO required 120.000 points while MOGA only required 2.600 points. Hence, in the present work, MOGA is of the order of 46 times more efficient in terms of resource efficiency.

Based on the authors experience and the provided descriptions, it can be inferred how BFSO requires from constant human input at every step along the process (see section 5.1) in order to find the Pareto fronts, unlike MOGA which directly runs into an (automatic) iterative process until the Pareto front is reached. Depending on the user's necessities, one method might be more advantageous than the other. In the case of BFSO, the main advantage is the ability to screen the entire design space and be able to store all the information. Therefore, BFSO is recommended when the details of the problem are relevant and information at every step during the Pareto search is necessary, in order to add context to the reached solution. In the case of MOGA, due to the nature of the algorithm, solutions pertaining to the sub-optimal region are lost in the iterative process and only the identified Pareto front is recorded into a file. Thus, MOGA will filter out non-optimal design points that can be considered noise and directly offers the solution.

Finally, as mentioned in the first paragraph, both methods reached the same solution thus, the details can be found in section 4.4.

6

Conclusions

The present research aimed to identify the demihull characteristics that enhance the seakeeping performance of a fast ferry catamaran sailing in irregular head waves by reducing wet deck slamming. To address the main research question, two main parts are distinguished, the numerical approach for modelling wet deck slamming and the numerical set-up to measure it, introduced next.

Modelling wet deck slamming

According to the literature review, research addressing wet deck slamming with numerical methods generally used high-fidelity CFD programs, which predictions were satisfactory validated. However, due to the relatively expensive simulations, such experiments are generally restricted to short duration, like free fall tests. Nevertheless, in order to assess wet deck slamming in a seakeeping context, more than one wave encounter is required. Thus, lower-fidelity programs had to be used, which obviously entailed a reduction in prediction accuracy. In the present work, the strip theory-based program FASTSHIP is considered for the seakeeping evaluation, which only addresses the interaction between the (demi)hull and the free surface. In order to address the interaction between the wet deck and the free surface, the impulse formulation is introduced, which allowed to quantify the interaction between these two elements in both time and space. Furthermore, it enabled the analysis of wet deck slamming in an intermediate point between purely statistical and physical oriented methods. Thus, offering the advantages of large simulation duration statistical analysis with the insights of physical-based approaches.

Impulse is defined as the integral of a (slamming) force F over a period of time Δt, measured whenever the free surface exceeds the wet deck with an upward relative velocity v. This velocity did not comply with the Dirichlet (no penetration) boundary condition, instead it just goes through the wet deck, hence an important modelling assumption is considered. However, the influence of such assumption to the research outcome is considered rather low. Mainly because indication towards lower slamming were not dictated by the impulse accuracy but rather by its average magnitude, which correlated satisfactorily with the hull shape modifications. Thus, assessing the seakeeping performance with regards to wet deck slamming.

Numerical set-up

The combination of an in-house built parametric hull with a DACE methodology and FASTSHIP conformed the research numerical set-up. In order to perform a design exploration, first, a sampling-based method to populate it was necessary. The Latin Hypercube Sampling (LHS) was identified as the most suitable sampling method, fulfilling the needs of high spatial variance and homogeneity. The sampled points were used to built a surrogate model of FASTSHIP with the method known as Kriging. Such choice proved to be a worth investment, specially for projects involving large amount of simulations, requiring a one-time process to built it, in exchange of inexpensive hull evaluations.

With all the required ingredients for mass evaluation of hulls set, the research goal was finally addressed. The main objective function considered in the research is the mean impulse J_{mean}, identified as a good indicator of wet deck slamming. Secondary objectives were namely the maximum number of wet deck exceedance recorded over the entire simulation N_{exc}, the overall number of recorded impulses N_{imp}, and the mean slamming velocity V_{mean}. All these objective functions were related to wet deck slamming. Nevertheless, a competition existed amongst each other, leading to the existence of a multi-objective optimal space, known as the Pareto front. Thus, a trade-off existed, where further (and final) decision shall depend on the naval architect (user) necessities.

The hulls within the Pareto region shared similar geometrical attributes, thus clearly defining the boundaries of the optimum design space. Comparing the hulls in the Pareto fronts with the parent hull used during the analysis, known as the 4212, the following main discrepancies were detected

- The dead rise angle at the aft-most region remained fairly similar, because a flat bottom is required anyways for the waterjets. Otherwise, low dead rise angles are required.
- Following from the previous bullet point, the Pareto-optimal hulls also displayed more volume at the aft, meaning less hull clearance for a propulsion device.
- The breadth at the chine and deck tend to be wider, which resulted in higher B/T ratios as well.
- The local draught at the bow tended to increase, meaning, the keel profile slightly bent downwards as one approeaches closer to the bow.
- The waterplane area angle of attack increased, thus increasing the wave making resistance. In an implicit way, the block and prismatic coefficients increased accordingly as well.

6.1 Recommendations

Based on the knowledge acquired during the research and the many faced obstacles, the following aspects are left as recommendations.

- According to the literature review, the hull motions are dictated by the relative difference between the hull dimension and the significant wave length. The present research only considered one environmental sea condition. Performing the same experiment with different sea characteristics (namely different significant wave height H_s and peak period T_p) shall provide a better insight on the wet deck slamming performance of the hulls within the Pareto fronts.

- Given the allowed time frame for the present project and the work required in setting-up the numerical platform of the research, the seakeeping simulations ended up being carried out by FASTSHIP, due to its acceptable accuracy to computational speed ratio. The method offered a good insight on the research questions, however, a higher-fidelity program will certainly offer a greater freedom and solve some of the faced limitations, in exchange of a relatively higher computational cost. For instance, PANSHIP, a time domain panel method for simulation of ship motions in waves developed at MARIN. Panel method-based programs uses potential flow, where fluid is assumed to be incompressible, inviscid and irrotational. Thus, local water deformations that are mainly driven by viscous-based phenomenon are out of its capabilities. Nevertheless, it offers a wider range of hull geometry tolerance, that can be coupled with the introduced parametric design tool (modified Wigley hull). Furthermore, as demonstrated in the present research, wet deck slamming in catamarans sailing in head waves can be reduced to its demihull, thus reducing the geometry complexity and thus, computational time. However, although not strictly necessary, it is highly recommendable to have access to a cluster.

Finally, it is worth mentioning that for mesh convergence study, MARIN recommends a structured mesh with the mesh cells as squared as possible. Furthermore, the main output parameter to track should be the motions and accelerations, where at least 180 wave encounters should be ensured for robust statistics.

Appendices

A

FASTSHIP

A.1 Mathematical model

A.1.1 Basic equation of motions

The general equation of motions with the main forces: thrust T, drag D, hydrodynamic force F_{dyn} and hydrostatic force F_{sta} are assembled as follows.

$$\begin{cases} M\ddot{X}_{CG} &= T\cos(\theta+\tau) - F_{dyn}\sin(\theta) - D\cos(\theta) \\ M\ddot{Z}_{CG} &= -T\sin(\theta+\tau) - F_{dyn}\cos(\theta) - F_{sta}\cos(\theta) + D\sin(\theta) + W \\ I\ddot{\theta} &= Tl_T + F_{dyn}l_{dyn} + F_{sta}l_{sta} - Dl_D \end{cases} \tag{A.1}$$

Where l_T, l_{dyn}, l_{sta} and l_D are the thrust, hydrodynamic force, hydrostatic force and drag lever arm with respect to the center of gravity, respectively.

A.1.2 Force breakdown

The modelling of F_{dyn} according to the current literature regarding basic naval architecture, is known as the total bare hull resistance R_T, which can be discretised into: wave resistance R_w, pressure resistance R_P, viscous resistance R_v and typically for high speed crafts, spray resistance R_{spray} and rail resistance R_{rail}. The latter two are directly ignored. R_w is assumed to be small at planing speeds $Fn_\nabla \geq 1.5$ and therefore negligible (so large inaccuracies arises below this regime) and same applies to viscous induced pressure resistance. Viscous induced pressure resistance is just part of R_v and at planing speeds, a phenomenon such as flow detachment is in fact negligible, thus it will not be considered. The other part of R_v is the viscous induced cross flow drag force, and this one is considered.

$$\begin{aligned} R_T &= \cancel{R_w} + R_P + R_v + \cancel{R}_{spray} + \cancel{R}_{ray} \\ &= R_P + R_v \\ &= \text{some hydrodynamic induced pressure lift} + \text{some viscous induced lift} \end{aligned}$$

Once identified the relevant terms that contribute to the equilibrium of forces, next, an evaluation is done at every strip.

A.1.2.1 Drag

Drag refers basically to friction resistance, dependent on the instant wetted surface, and is formulated as follows.

$$D = \frac{1}{2} C_F \rho U^2 A_w \tag{A.2}$$

Where U is the flow velocity parallel to the keel modelled as $U = \dot{X}_{CG}\cos(\theta) - \dot{Z}_{CG}\sin(\theta)$. In this expression the orbital velocity influence is omitted as it is considered negligible. The friction coefficient C_F is obtained by means of the ITTC formula, with the particularity that the Reynolds number is updated at each timestep by computing the mean of the wetted keel and wetted chine lengths, L_m.

$$\begin{aligned} L_m &= \frac{L_k + L_c}{2} \\ R_n &= \frac{U L_m}{\nu} \\ C_F &= \frac{0.075}{(log(R_n) - 2)^2} \end{aligned}$$

A.1.2.2 Hydrostatic force

The hydrostatic force is computed by identifying the volume underwater of each strip. However, at planning regime an under-pressure surrounding the hull arises, resulting in a lower effective hydrostatic force. Therefore, the buoyancy is corrected with the buoyancy correction factor a_{bf} and a_{bm} for the transversal and longitudinal planes respectively. The latter is mainly meant for the righting moment correction of pitch motion.

$$\begin{aligned} f_b &= a_{bf} \rho g A \\ a_{bf} &\in [0, 1] \end{aligned} \tag{A.3}$$

A.1.2.3 Hydrodynamic force

As stated at the beginning of this section, the hydrodynamic forces were reduced to the contribution of a pressure-and viscous-based source of resistance, f_{fm} and f_{cdf} respectively. Zarnick [27] modelled f_{fm} as the rate of change of momentum of the flow under the cross section considered.

So a total derivative is applied to the momentum, which is expressed in terms of the added mass.

$$\begin{aligned} f_{fm} &= \frac{D}{Dt}(m_a V) \\ &= V\frac{dm_a}{dt} + m_a\frac{dV}{dt} + \bar{u} \cdot \bar{\nabla}(m_a V) \\ &= V\frac{dm_a}{dt} + m_a\frac{dV}{dt} + \left(-\frac{dx}{dt}\right) \cdot \frac{d}{dx}(m_a V) \\ &= V\frac{dm_a}{dt} + m_a\frac{dV}{dt} - \frac{d}{dx}(m_a V)U \end{aligned} \tag{A.4}$$

Where U and V are the flows parallel and normal to the keel respectively. Due to the considered frame of reference, the Lagrangian term of the total derivative has the negative term $-U$. U, V and dV/dt will be properly derived further down.
For the modelling of the added mass m_a two modes are distinguished (the dry chine and wet chine mode, which depends on the submergence level of the evaluated strip). The main difference between the two modes is the water pile up effect, represented by the pile

up factor C_{pu}.

Therefore, the added mass expression will vary depending on the mode considered. The general form of m_a is based on the Wagner formulation, as shown next, and its time derivative as well.

$$\begin{aligned} m_a &= C_m \frac{\pi}{2} \rho b^2 \\ \frac{dm_a}{dt} &= C_m \pi \rho b \frac{db}{dt} \end{aligned} \tag{A.5}$$

Where C_m is the added mass coefficient, determined empirically. Further details explained below. From this general expression, distinction is made based on the rate of change of the local breadth as the cross section sinks. Which can either be:

- **Dry chine**
  In this case the breadth depends on the instantaneous draught h.

$$b = h \cdot \cot(\beta) \tag{A.6}$$

- **Wetted chine**
  In this case the water pile up factor C_{pu} is introduced. The application of this factor follows from Payne, who realized that using Wagner's pile up factor of $\pi/2$ resulted in too high impact loads compared to the analogous experimental values, and thus added a dead rise angle dependency that improved its accuracy.

$$\begin{aligned} b &= C_{pu} h \cdot \cot(\beta) \\ C_{pu} &= \frac{\pi}{2} - \beta \left(1 - \frac{2}{\pi}\right) \end{aligned} \tag{A.7}$$

Regarding the cross flow drag force, it is formulated as follows, where $C_{D,c}$ is the cross flow drag coefficient which is determined empirically.

$$f_{cdf} = C_{D,c} \cos(\beta) \rho b V^2 \tag{A.8}$$

Finally, by combining eq. (A.4) and eq. (A.8) together the full hydrodyanmic force expression is derived.

$$\begin{aligned} f_{dyn} &= f_{fm} + f_{cfd} \\ &= V \frac{dm_a}{dt} + m_a \frac{dV}{dt} - \frac{d}{dx}(m_a V) U + C_{D,c} \cos(\beta) \rho b V^2 \end{aligned} \tag{A.9}$$

A.1.2.4 Transom flow correction

The transom flow correction is a shape factor that corrects the longitudinal lift profile. It accounts for the developing underpressure at the transom when sailing at planing regime. This factor forces the longitudinal pressure profile along the hull to decay as evaluation gets closer to the transom, until it is completely zero at the transom.

$$C_{tr}(x) = \tanh\left(\frac{2.5}{a}(x - x_{TR})\right) \tag{A.10}$$

Where a is a reduction length and x_{TR} is the longitudinal transom coordinate. The determination of a is achieved by a non-dimensional analysis approach done by Garme, who determined a value for the non-dimensional reduction length $\tilde{a}$ by means of a systematic model experiment.

$$C_v = \frac{V_s}{\sqrt{gB_m}}$$
$$\tilde{a} = \frac{a}{B_m C_v} = 0.34$$

Where B_m is the mainsection breadth and C_v is the Froude number as a function of B_m.

$$C_{tr}(x) = \tanh\left(\frac{2.5}{0.34 B_m C_v}(x - x_{TR})\right) \tag{A.11}$$

This correction is always the same no matter the underwater configuration, which at some points can result in substantial inaccuracies and deviations when compared to experimental results.

A.1.2.5 2D flow around the hull

Lastly, the modelling of the flow around the hull. One of the simplification in FASTSHIP is neglecting the horizontal orbital velocity wave component, as it is considered to be very small compared to the ship speed. Therefore, when describing the relative velocities between the hull and water U and V, only the hull motions and the vertical orbital velocity wave component (w) are considered.

$$\begin{aligned} U &= \dot{X}_{CG}\cos(\theta) - (\dot{Z}_{CG} - w)\sin(\theta) \\ V &= \dot{X}_{CG}\sin(\theta) - (\dot{Z}_{CG} - w)\cos(\theta) - \dot{\theta}x \end{aligned} \tag{A.12}$$

Because dV/dt will be required in the following derivations:

$$\frac{dV}{dt} = \ddot{X}_{CG}\sin(\theta) + \ddot{Z}_{CG}\cos(\theta) + \ddot{\theta}x + \dot{\theta}(\dot{X}_{CG}\cos(\theta) - \dot{Z}_{CG}\sin(\theta)) - \frac{dw}{dt}\cos(\theta) + \dot{\theta}w\sin(\theta) \tag{A.13}$$

A.1.3 Final equation of motions

Assembling all the above explained will lead to a further derived form of eq. (A.1). The integral form of the above introduced forces along the 3 main degrees of freedom are

$$\begin{aligned} F_x &= -\int_L C_{tr} f_{dyn}\sin(\theta)dx \\ F_z &= -\int_L C_{tr} f_{dyn}\cos(\theta)dx - \int_L C_{tr} f_b dx \\ F_\theta &= \int_L C_{tr} f_{dyn} x dx + \int_L C_{tr} f_b \cos(\theta) x dx \end{aligned} \tag{A.14}$$

As it can be appreciated, for each of the terms within the 3 degrees of motions, the transom correction factor is applied.
Substituting eq. (A.3), eq. (A.9), eq. (A.11), eq. (A.12) and eq. (A.13) into eq. (A.14) and then assembling into the general form of eq. (A.1) yields:

$$
\begin{aligned}
F_x = \Big[&-M_a\ddot{X}_{CG}\sin(\theta) - M_a\ddot{Z}_{CG}\cos(\theta) + Q_a\ddot{\theta} \\
&- M_a\dot{\theta}(\dot{X}_{CG}\cos(\theta) - \dot{Z}_{CG}\sin(\theta)) + \int_L C_{tr}m_a\frac{dw}{dt}\cos(\theta)dx \\
&- \int_L C_{tr}m_a\dot{\theta}w\sin(\theta)dx - \int_L C_{tr}\frac{dm_a}{dt}V\,dx + \int_L C_{tr}UV\frac{dm_a}{dx}dx \\
&- \int_L C_{tr}Um_a\frac{dw}{dx}\cos(\theta)dx - \int_L C_{tr}Um_a\dot{\theta}dx \\
&- \int_L C_{tr}C_{D,c}\cos(\beta)\rho bV^2dx\Big]\sin(\theta)
\end{aligned}
$$

$$
\begin{aligned}
F_z = \Big[&-M_a\ddot{X}_{CG}\sin(\theta) - M_a\ddot{Z}_{CG}\cos(\theta) + Q_a\ddot{\theta} \\
&- M_a\dot{\theta}(\dot{X}_{CG}\cos(\theta) - \dot{Z}_{CG}\sin(\theta)) + \int_L C_{tr}m_a\frac{dw}{dt}\cos(\theta)dx \\
&- \int_L C_{tr}m_a\dot{\theta}w\sin(\theta)dx - \int_L C_{tr}\frac{dm_a}{dt}V\,dx + \int_L C_{tr}UV\frac{dm_a}{dx}dx \\
&- \int_L C_{tr}Um_a\frac{dw}{dx}\cos(\theta)dx - \int_L C_{tr}Um_a\dot{\theta}dx \\
&- \int_L C_{tr}C_{D,c}\cos(\beta)\rho bV^2dx\Big]\cos(\theta) - \int_L C_{tr}a_{bf}\rho gAdx
\end{aligned}
\tag{A.15}
$$

$$
\begin{aligned}
F_\theta = &- Q_a\ddot{X}_{CG}\sin(\theta) - Q_a\ddot{Z}_{CG}\cos(\theta) - I_a\ddot{\theta} \\
&+ Q_a\dot{\theta}(\dot{X}_{CG}\cos(\theta) - \dot{Z}_{CG}\sin(\theta)) - \int_L C_{tr}m_a\frac{dw}{dt}\cos(\theta)xdx \\
&+ \int_L C_{tr}m_a\dot{\theta}w\sin(\theta)xdx + \int_L C_{tr}\frac{dm_a}{dt}Vxdx - \int_L C_{tr}UV\frac{dm_a}{dx}xdx \\
&+ \int_L C_{tr}Um_a\frac{dw}{dx}\cos(\theta)xdx + \int_L C_{tr}Um_a\dot{\theta}xdx \\
&+ \int_L C_{tr}C_{D,c}\cos(\beta)\rho bV^2xdx + \int_L C_{tr}a_{bm}\rho gA(x\cos(\theta) + y\sin(\theta))dx
\end{aligned}
$$

where

$$
\begin{aligned}
M_a &= \int_L C_{tr}m_adx \\
Q_a &= \int_L C_{tr}m_axdx
\end{aligned}
$$

Now by substituting eq. (A.15) into the corresponding terms of eq. (A.1) and rearranging the common terms the following system of equations can be obtained.

$$
\begin{bmatrix}
M + M_a\sin^2(\theta) & M_a\sin(\theta)\cos(\theta) & -Q_a\sin(\theta) \\
M_a\sin(\theta)\cos(\theta) & M + M_a\cos^2(\theta) & -Q_a\cos(\theta) \\
-Q_a\sin(\theta) & -Q_a\cos(\theta) & I + I_a
\end{bmatrix}
\cdot
\begin{pmatrix}
\ddot{X}_{CG} \\ \ddot{Z}_{CG} \\ \ddot{\theta}
\end{pmatrix}
=
\begin{pmatrix}
T\cos(\theta + \tau) + F'_x - D\cos(\theta) \\
-T\sin(\theta + \tau) + F'_z + D\sin(\theta) + W \\
Tl_T + F'_\theta - Dl_D
\end{pmatrix}
\tag{A.16}
$$

Which then can be treated as a linear system of equations, where the motion's accelerations are the unknowns. To solve this equation, a Runge-Merson iteration scheme is applied.

$$
\begin{aligned}
\bar{\bar{M}} \cdot \ddot{\bar{X}} &= \bar{F} \\
\ddot{\bar{X}} &= \bar{\bar{M}}^{-1} \cdot \bar{F}
\end{aligned}
$$

Further clarifications on the derivations

$$\begin{aligned}\frac{d}{dx}(m_a V)U &= UV\frac{dm_a}{dx} + m_a U\frac{dV}{dx} \\ &= UV\frac{dm_a}{dx} + m_a U\frac{d}{dx}[\dot{X}_{CG}\sin(\theta) + (\dot{Z}_{CG} - w)\cos(\theta) - \dot{\theta}x] \\ &= UV\frac{dm_a}{dx} + m_a U\left(-\frac{dw}{dx}\cos(\theta) - \dot{\theta}\right) \\ &= UV\frac{dm_a}{dx} - m_a U\frac{dw}{dx}\cos(\theta) - m_a U\dot{\theta}\end{aligned}$$

A.1.4 Empirical side of the model

The mathematical model of FASTSHIP is now fully derived, but there are four coefficients that are left “open”, namely: C_m, $C_{D,c}$, a_{bf} and a_{bm}. These hydrodynamic coefficients are highly dependent on the hull geometry and flow characteristics. They can be obtained in the Delft Systematic Deadrise Series (DSDS), a polynomial regression generated from a series of experiments with different family hull members in the Delft towing tank.

Solving eq. (A.14), with the hull motions (and forces) known from the sensors placed in the hull and solving for the coefficients, the unknowns, a data set of these coefficients for every speed is generated. But there are 3 equations and 4 unknowns, so the longitudinal buoyancy correction factor is assumed to be $a_{bm} = 1$, based on the fact that the experiments were performed in calm waters. Furthermore, *Keuning* [11] assumed that $C_{D,c} = 1.33$. So the system of equations reduces to 2 equations and 2 unknowns (C_m and a_{bf}) with steady conditions assumed, meaning there are no accelerations, which allows for further simplification.

A.2 Set-up

FASTSHIP is an executable file (.exe) that can be conveniently executed from a batch file. In the present research, FASTSHIP is managed from a *Python* script.

Two input files are required for FASTSHIP:

- **RKVB.inp:** In this file, the hull geometry and simulation parameters are specified.
- **Spectrum.inp** In this file, the wave data is specified, namely the wave amplitude, wave frequency, wave number and phase angle. To specify a regular wave one line with the aforementioned information is required. For an irregular wave an N_f number of regular waves can be set.

In fig. A.1, a flow chart illustrating the *Python* script involving FASTSHIP is displayed. As it can be appreciated, the process starts by specifying the number of simulations N_K. Amongst the different simulation parameters, a default time step $dt = 0.01s$ is set before executing FASTSHIP. Once FASTSHIP process is terminated the output is evaluated and if it doesn’t pass the quality control criteria (i.e. not reaching the specified simulation duration), a new time step is set. Once the criteria is met, the output is conveniently post-processed and next simulation starts.

In the following sections, relevant steps within the pre-processing, processing and post-processing phases will be explained.

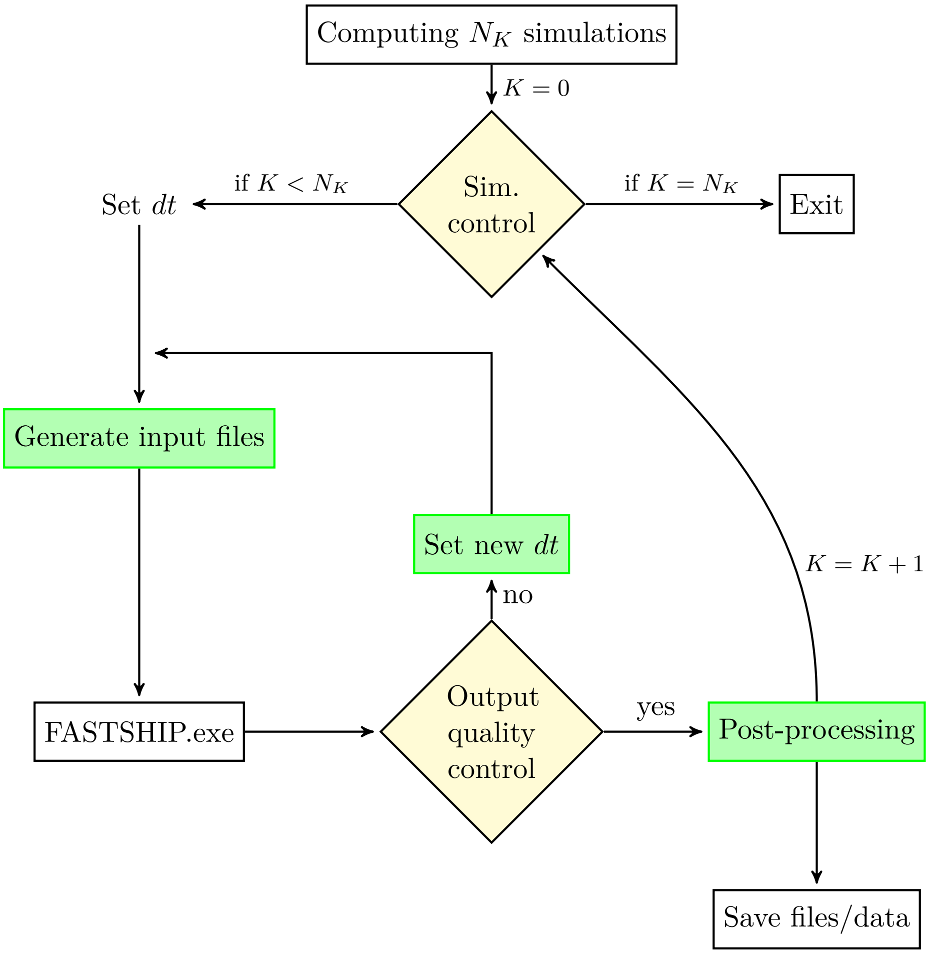

Figure A.1: Flow chart illustrating the *Python* script built around FASTSHIP.

A.2.1 Pre-processing

The pre-processing phase concerns to the preparation of the above described input files, where two main relevant parts will be highlighted, concerning the hull geometry and the wave properties. .

A.2.1.1 Geometry

In FASTSHIP, the hull geometry is described by frames, and each frame described with 3 coordinates namely the keel, chine and deck. The maximum allowable number of sections is 120, and they do not need to be equally distributed along the length.
An important limitation to mention is that FASTSHIP cannot handle flat bottoms ($\beta \neq 0$), so a very small dead rise angle has to be used instead. This is because the added mass formulation from Payne, eq. (A.6) and eq. (A.7) has a $\cot(\beta)$ term in it. Thus when $\beta = 0$ an indeterminate of the form $\cot(0) = \infty$ is obtained.

Other relevant aspects of the geometry are already covered in the main body of the present document.

A.2.1.2 Wave

The simulations can either be in calm water, regular wave or irregular wave. In fig. A.2, a flow chart indicating the steps to specify either of the options can be found.

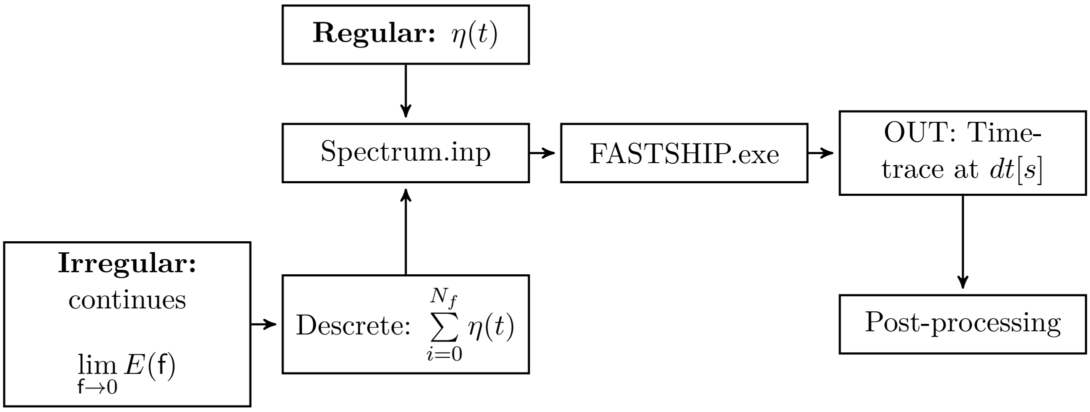

Figure A.2: Flow chart of the steps to consider when setting either a regular or irregular wave environment in FASTSHIP.

In FASTSHIP, irregular waves are modelled with the random phase-amplitude model, as introduced in eq. (3.21).

$$\eta(x,t) = \sum_{i=1}^{N_f-1} a_i \sin\left(\omega_e t + \alpha_i + k(x - LCG) + \varphi_i\right)$$

where the amplitudes and frequencies are obtained from the *Jonswap* spectrum, introduced in 3.22 with a peak enhancement factor $\gamma = 3.3$.

$$E_{Jon}(\mathsf{f}) = \alpha g^2 (2\pi)^{-4} \mathsf{f}^{-5} \exp\left[-\frac{5}{4}\left(\frac{\mathsf{f}}{\mathsf{f}_p}\right)^{-4}\right] \gamma^{\exp\left[-\frac{1}{2}\left(\frac{\mathsf{f}-\mathsf{f}_p}{\sigma \mathsf{f}_p}\right)^2\right]}$$

$$\alpha = 5.061 \mathsf{f}_p^4 H_s^2 (1 - 0.287 log\gamma)$$

The problem with the *Jonswap* spectrum is that there is no spectral energy at the low frequencies, which one could interpret as no swell. The consequences of such phenomenon translates into a wrongful RAO with very big (or even infinite if $S_w(\mathsf{f}) = 0$) values at those frequency ranges. All things considered, the issue is not very relevant since RAOs are not an indicator of slamming for the present research. However, RAOs can inform about the hull's eigen-frequency and thus, add more context and insight into the seakeeping performance. Thus, achieving a correct RAO can potentially benefit the user's research. Therefore, an optional addition to the *Jonswap* spectrum is formulated in order to artificially add energy at low frequencies. The aim is to eliminate the numerical "singularities" that a $S_w(\mathsf{f}) \sim 0$ may suppose. The added term consist of an exponential decaying function as shown next

$$E_1(\mathsf{f}) = E_0(\mathsf{f}_p) \exp\left[-\lambda \left(\frac{\mathsf{f}}{\mathsf{f}_p}\right)^n\right]$$

$$\text{Where:} \qquad \begin{cases} \lambda & = 10 \\ n & = 5 \end{cases} \tag{A.17}$$

where λ is the decaying rate, n the dacaying order and $E_0(\mathsf{f}_p)$ is the spectral energy to be added (left to the user to decided). In fig. A.3, the difference between the original *Jonswap* spectrum and the one with the additional term is illustrated. By means of trial and error, the values of $\lambda = 10$ and $n = 5$ are found to be the best fitting. Thus, adding eq. (A.17) to the original expression yields

$$E(\mathsf{f}) = E_{Jon}(\mathsf{f}) + E_1(\mathsf{f}) \tag{A.18}$$

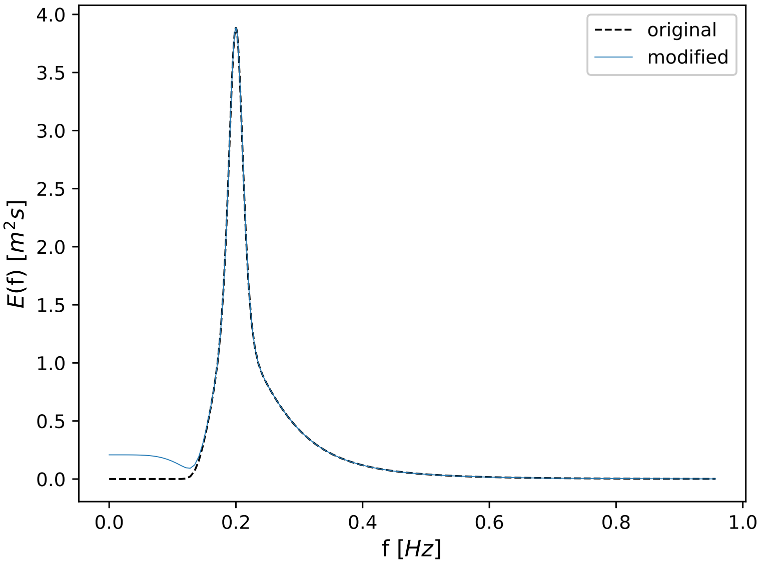

Figure A.3: Comparison between original and modified *Jonswap* spectrum

Another factor to consider is the way the *Jonswap* spectrum is discretized. Due to its narrow energy peak, an even split of N_f number of frequencies can potentially miss it (specially at low N_f). Therefore, a sine-cosine discretization scheme, shown below, is applied in order ensure the *Jonswap* peak resolution is not loss regardless of the N_f value, that is, around the peak frequency f_p.

$$\begin{gathered} distr = \left\{ \sin\left(\frac{\pi}{(N_f-2)} i\right), 2 - \cos\left(\frac{\pi}{N_f}(i+1)\right) \right\} \\ \text{where} \quad i = 0, 1, 2, ..., \left(\frac{N_f}{2} \in \mathbb{N}\right) - 1 \end{gathered} \tag{A.19}$$

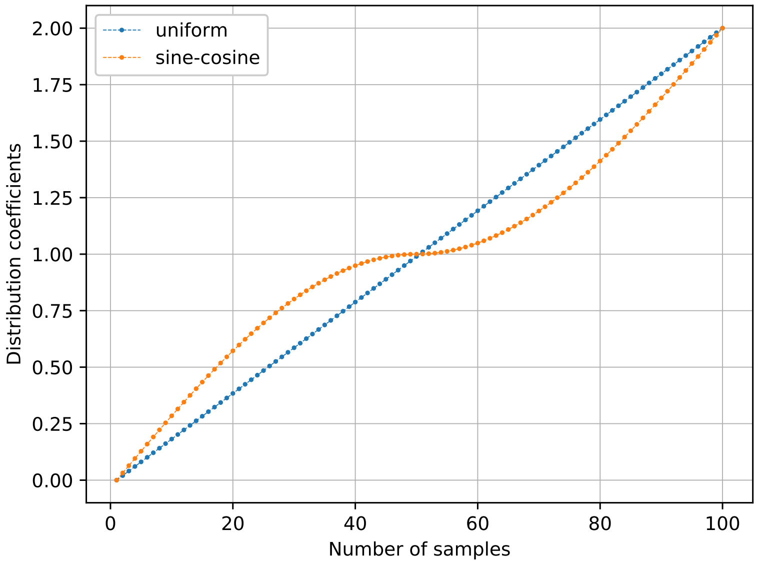

Figure A.4: Sample distribution comparison between a uniform and sine-cosine scheme

In fig. A.4, the difference between the uniform and the sine-cosine distribution is displayed, where same number of discrete points are used. As it can be appreciated, with the sine-cosine scheme, there are more points around the distribution coefficient 1 (in the horizontal axis). Hence, increasing the *Jonswap* spectrum peak resolution, where f_p would be aligned with the coefficient 1.
Furthermore, in FASTSHIP the timetrace outputs of the ship motions —heave and pitch— are defined from a Lagrangian perspective, meaning the timatraces are defined with the hull sailing at speed V_s while encountering head waves. Translating such timetraces into the frequency domain would actually corresponding to the encounter frequency f_e. By anticipating to this fact, output quality can be enhanced by performing the discretization around the encounter peak frequency $\mathsf{f}_{p,e}$ (provided V_s and the significant wave characteristics are known) and then translate it back into the fixed frequency axis f_0. This can be achieved by considering the Doppler shift effect

$$\mathsf{f}_e = \mathsf{f}_0 + \frac{k}{2\pi}U \tag{A.20}$$

The process is as follows:

1. Set the desired peak frequency spectrum $\mathsf{f}_{p,0}$.
2. Translate the peak frequency from the fixed frequency to the encounter frequency axis $\mathsf{f}_{p,e}$ with eq. (A.20).
$$\mathsf{f}_{p,e} = \mathsf{f}_{p,0} + \frac{k}{2\pi}U \tag{A.21}$$
3. Apply the sine-cosine distribution (eq. (A.19)) to $\mathsf{f}_{p,e}$ so the frequency discretezation is performed at the encounter frequency axis.
It is worth mentioning, that the sine-cosine scheme consists on a set of coefficients that ranges from 0 to 2. So the product between *distr* and $\mathsf{f}_{p,e}$ results in a frequency vector which values are proportional to $\mathsf{f}_{p,e}$, as shown below, and according to eq. (A.21), $\mathsf{f}_{p,e}$ is function of $\mathsf{f}_{p,0}$.
$$\begin{aligned} distr &\in [0,2] \\ distr &= (0, ..., 1, ..., 2) \\ distr \cdot \mathsf{f}_{p,e} &= (0, ..., \mathsf{f}_{p,e}, ..., 2\mathsf{f}_{p,e}) \end{aligned}$$
However, waves with a frequency beyond 1 Hz are meaningless for the motion analysis, thus, the boundary [0, 1] Hz is set in the fixed frequency axis. In order to ensure the analogous is set in the encounter frequency axis, the power factor p is introduced, which ensures the same boundary is applied the encounter frequency axis, of the form $[0,\ 1 + 2U/g]$ Hz (by applying eq. (A.20)). With it, a consistent formulation for the discretization of the frequency axis at encounter frequency can be achieved.
$$\begin{aligned} 2^p \mathsf{f}_{p,e} &= 1 + \frac{2\pi U}{g} \\ p \log(2) &= \log\left(\frac{1 + \frac{2\pi U}{g}}{\mathsf{f}_{p,e}}\right) \\ p &= \frac{\log\left(\frac{1+\frac{2\pi U}{g}}{\mathsf{f}_{p,e}}\right)}{\log(2)} \end{aligned} \tag{A.22}$$
thus,
$$\bar{\mathsf{f}}_e = \mathsf{f}_{p,e} \cdot distr^p \tag{A.23}$$

4. Translate back $\bar{\mathsf{f}}_e$ into fixed frequency reference. This is simply done by introducing the dispersion relation (in deep water conditions) into eq. (A.20). Thus, a binomial equation is obtained, as derived below

$$\omega^2 = kg \tag{A.24}$$

$$\begin{aligned} \bar{\mathsf{f}}_e &= \bar{\mathsf{f}}_0 + \frac{\omega^2}{2\pi g}U \\ &= \bar{\mathsf{f}}_0 + \frac{2\pi\bar{\mathsf{f}}_0^2}{g}U \\ \bar{\mathsf{f}}_0 &= -\frac{1-\sqrt{1+\frac{8\pi U}{g}\bar{\mathsf{f}}_e}}{\frac{4\pi U}{g}} \end{aligned}$$

5. Now the spectrum can be strategically discretized into the corresponding regular waves.

$$E(\mathsf{f_i}) = \frac{1}{\Delta\mathsf{f_i}}\frac{1}{2}a_i \qquad \mathsf{f}_i \in \bar{\mathsf{f}}_0$$

A.2.2 Processing

According to the FASTHSIP manual, FASTSHIP makes use of a memory matrix with 75000 slots. Although it is not quite clear how exacty is this memory matrix being used, it is very clear that a very small time step results in a memory shortage and therefore, a big time step results in an underuse of it.

Based on trial and error analysis with different time steps the following time step control function proved to consistently stay within the memory limitations and make the most of it.
Given a vector with different time step values $\bar{t}_{sim}$, this vector contains all the possible time steps.

$$\bar{t}_{sim} = \{0.02, 0.05, 0.075, 0.1, 0.2, 0.4, 0.5, 1\}$$

Based on the desired simulation duration t_0 (specified in minutes) the finer possible time step dt'_{max} that stays within the memory limitations is computed. Any time step lower than dt'_{max} will result in data that won't fit into the memory space.
Based on the dt'_{max} value, the direct value within $\bar{t}_{sim}$ that is greater than dt'_{max} is chosen to be the actual time step dt_{max}. By default $dt_{max} = 0.01$.

$$\begin{aligned} dt'_{max} &= \frac{t_0 \cdot 60}{75000} \\ dt_{max} &= \{\bar{t}_{sim} \mid f(dt_i \in \bar{t}_{sim} > dt'_{max})\} \end{aligned}$$

```python
t0 = 20
tSimMaxVec = np.array([0.02, 0.05, 0.075, 0.1, 0.2, 0.4, 0.5, 1])
if (t0*60)/75000 > 0.01:
    tSimMax = tSimMaxVec[np.where(tSimMaxVec > t0*60 / 75000)[0][0]]
else:
    tSimMax = 0.01
```

Figure A.5: *Python* code of the time step control

A.2.3 Post-processing

FASTSHIP generates the following output files:

- **General.out**
  Summary of the input data and a quality evaluation of it, so the user can re-tune the input if desired.
- **Kutmer.out**
  Contains a log of errors per time step. When an iteration doesn't meet the tolerance set in the input, time step is halved up to 7 times maximum. And this is recorded in the output file.
- **Timetrace.out:** Contains the following data.
  1. Time [s]
  2. Forward speed [m/s]
  3. Heave velocity [m/s]
  4. Pitch velocity [°/s]
  5. Horizontal displacement [m]
  6. Sinkage or rise of CG (sinkage: positive / rise: negative)[m]
  7. Pitch angle [deg]
  8. Total calculated earth fixed horizontal force [N]
  9. Total calculated earth fixed vertical force [N]
  10. Total calculated pitch moment [Nm]
  11. Vertical acceleration in CG [m/s2]
  12. Vertical acceleration at the bridge [m/s2]
  13. Vertical acceleration at the bow [m/s2]
  14. Wave height at CG
- **Waves.out**
  Contains time trace of the wave elevation and wave vertical horbital velocity per strip.

Next, the relevant post-processing is explained.

A.2.3.1 Frequency domain

Switching from time domain to frequency domain is done by means of the Discrete Fourier Transform (DFT). As shown below, DFT stipulates that any time dependent signal $f(t)$ can be represented as a sum of a constant a_0 and a combination of sines and cosines.

$$f(t) = \frac{1}{2}a_0 + \sum_{i=0}^{\infty}(a_k\cos(2\pi kt) + b_k\sin(2\pi kt))$$

Continue:

$$\mathcal{F}(F_s) = \int_{-\infty}^{\infty} f(t)\cdot\exp\left(-2\pi F_s ti\right)dt \tag{A.25}$$

Discrete:

$$\mathcal{F}_k = \sum_{n=0}^{N-1} a_n\cdot\exp\left(-\frac{2\pi kn}{N}i\right)$$

There are few details that needs to be taken into consideration when performing the switch to frequency domain. To understand the process, the frequency domain transformation is explained below.

1. Given a timetrace of length L_{data} and duration D with time step dt, the sampling frequency is:
$$F_s = \frac{1}{dt} \tag{A.26}$$
2. When the timetrace is too large, sampling it directly with the DFT would result in a noisy spectrum, because the data is not stationary. Meaning, too much waves per frequency slots exist, annihilating the "uniqueness" of the regular waves involved in the timetrace. To deal with that, the timetrace is split into P_{block} even blocks, each with duration D_{block}. Each block then will have a length P_{row}.
$$\begin{aligned} P_{row} &= \mathbb{N}\left\{\frac{L_{data}}{P_{block}}\right\} \\ D_{block} &= \frac{D}{P_{block}} \end{aligned} \tag{A.27}$$
3. The longest wave that can be fitted within D_{block} will mark the frequency resolution $d\mathsf{f}$ of the DFT. Next, different ways of computing $d\mathsf{f}$ is shown:
$$d\mathsf{f} = \frac{1}{D_{block}} = \frac{1}{D/P_{block}} = \frac{P_{block}}{D} = \frac{P_{block}}{(L_{data}-1)dt} = \frac{P_{block}F_s}{L_{data}-1}$$
4. Due to the aliasing effect, the second half of the DFT will be a mirror of the first half. Thus, only the data up to the Nyquist frequency f_N is considered.
$$\mathsf{f}_N = \frac{F_s}{2} \tag{A.28}$$
   The DFT values will be layout in a frequency axis going from 0 to f_N with $d\mathsf{f}$ frequency steps. As shown in the previous point, the longer the block duration D_{block} the smaller will be the frequency resolution, thus the frequency discretization becomes finer. One should be careful on tuning $d\mathsf{f}$ because the smaller it is, the larger the amount of frequency bins and since the wave input is discrete, some frequency bins might be zero. Thus, a trade-off between N_f and $d\mathsf{f}$ exists, where the frequency axis of the DFT should match the frequency axis described in the pre-processing section.

   Next, a demonstration of how the frequency vector up to f_N is indeed half of the block length.
$$\frac{\mathsf{f}_N}{\mathsf{f}_N} = \frac{F_s}{\frac{P_{block}}{D}2} = \frac{DF_s}{P_{block}2} = \frac{D}{P_{block}dt2} = \frac{D(L_{data}-1)}{P_{block}2D} = \frac{P_{rows}}{2} \tag{A.29}$$
5. The resulting frequency domain will thus be
$$\bar{\mathsf{f}} = \{0, i\cdot\mathsf{f}, \ldots, \mathsf{f}_N\} \quad \text{where} \quad i = 1, 2, 3, \ldots, \frac{P_{rows}}{2} \tag{A.30}$$

Tuning N_f and $d\mathsf{f}$, in order to ensure the resulting DFT frequency axis matches the input frequency can be an arduous task for little pay-off. To bypass this problem, on top of the above mentioned mechanisms and due to the amount of noise that can result in these calculations, a low pass filter is used is applied. Namelu, the Savitzky-Golay filter, proved to be perform very satisfactory. An example is shown in fig. A.6, where the orange line is the filtered signal and the blue dashed line the DFT signal. As it can be appreciated, the Savitzky-Golay filter interprets pretty well the underlying shape of the noisy spectrum and is not greatly affected by local points that may deviate largely from the overall trend, unlike other filters, for instance, a polynomial fit.

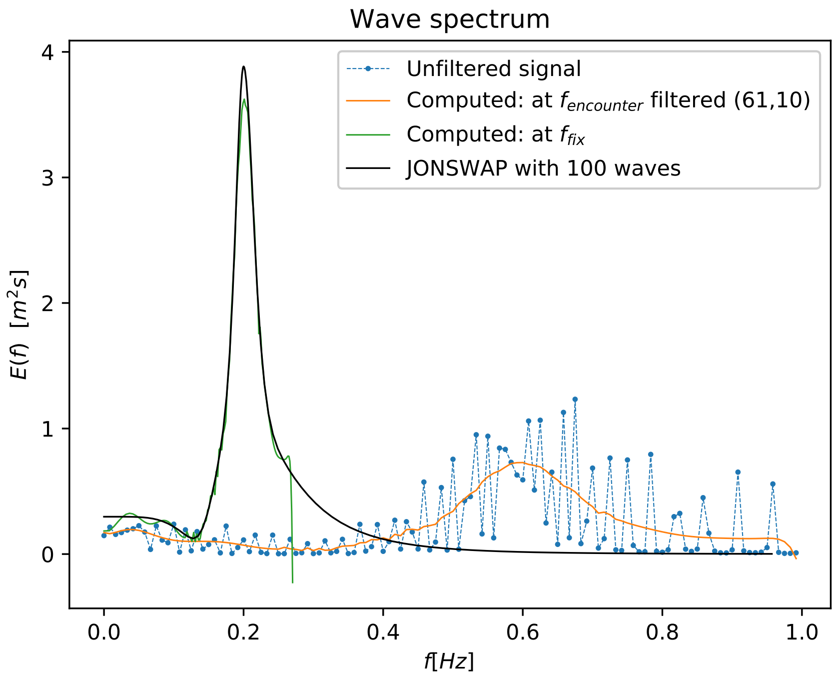

Figure A.6: *Jonswap* spectrum comparison between the inputed and outputed from FASTSHIP

B

DOE

B.1 Sampling methods

In this section, further details of the sampling-based methods considered in the present research can be found.

Central Composite Design

Box-Wilson Central Composite Design also known as central composite design (CCD) is a method that builds the response surface with a quadratic function approximation technique. Upon specifying a lower and upper limit for each of the k number of variables (of the problem), the overall amount of points involved is 2^k, if full combination is considered, also known as full factorial. CCD can reduce the combinations to $< 2^k$ amount of points, known as an embedded factorial design or fractional factorial design, and combines it with a center-point and a group of points known as 'star points', that allows for the estimation of response surface curvature.

This method exponentially increases the computational load as the number of variables to account increases. The number of samples N_s within CCD as a function of the number of variables N_{var} can be computed with:

$$N_s = 1 + 2N_{var} + 2^{N_{var}} \tag{B.1}$$

Box-Behnken Design

Box-Behnken Design (BBD) is similar to CCD approach but is full factorial instead (all combinations accounted), but rather considering 2 points per variable, it requires 3. Thus, the overall amount of points for k number of variables (of the problem) is 3^k. These points are the lower-upper limits and a mid point of the previous.
A required characteristic that BBD needs to fulfill is rotationality, where the distance between the points around the central one must be equal. This approach quickly loses its efficiency when there are more than 4 variables to account —due to the 3^k relation— as the required amount of computations massively increases, to a higher rate than CCD.

The number of samples N_s within BBD as a function of the number of variables N_{var} can be computed with:

$$N_s = 1 + 4N_{var} + \frac{N_{var} - 1}{2} \tag{B.2}$$

Orthogonal Array Designs

Orthogonal array (OA) is a sampling method that treats each of the n number of input variables as independent of each other. Thus, an initial assumption of no interaction between variables is set. For every variable, the user has to specify an s amount of values per variable, not necessarily the same amount for each of them. Based on these parameters, the amount of sample points m can be obtained as

$$m = 1 + \sum_{i=1}^{n} (s_i - 1) \tag{B.3}$$

OA is based on array orthogonality, a property that enables a pairwise comparison between arrays in an isolated manner. After evaluating different pairs of orthogonal arrays, the influence of each variable to the response can be computed.

Grid Design

Grid design method creates a mesh from the specified input variables and values, and builds a multi-dimensional matrix similar to the multi-dimensional parameter study. However, it adds a small random perturbation that unstructures the mesh and allows to capture periodic phenomena that otherwise, would be missed.

Monte Carlo Design

Monte Carlo sampling method is a purely stochastic method that upon the specification of an the upper-lower bound for every variable, it generates the samples with an uniform distribution.

Latin Hypercube Sampling

Latin Hypercube Sampling (LHS) is a near-random sampling technique that given a multi-dimensional parameter space containing the k number of input variables, only one sample per crossing hyperplane in the multi-dimensional space is allowed.
The samples are generated from a user specified distribution scheme per variable.
Unlike the classical random sampling techniques, LHS keeps track of the produced pseudo-random samples. Thus, each new point will be distanced from previous existing points according to the LHS sampling mechanisms.

FSUADE

The Florida State University Design and Analysis of Computer Experiments (DACE) is a DACE method that mixes the use of Monte Carlo sampling (Halton and Hammersley) with a Cetroidal Voronoi Tessellation (CVT) method. Both methods are meant to generate a uniform distributed set of points within a user-specified bounds per variable.

Monte Carlo sampling capabilities are better exploited in low dimensions (preferably 1-D) whereas CVT sampling capabilities are better used for higher dimensions such as volumetric spaces. In the opposite dimensions of the mentioned, these methods tends to perform a poorer isotropic distribution.

PSUADE

Problem Solving Environment for Uncertainty Analysis and Design Exploration (PUSADE) is a tool that supports metamodeling, sensitivity analysis, uncertainty quantification, and optimization studies. However, specific to the DACE field, it uses the Morris One-At-A-Time (MOAT) screening method. A method that quantifies among the k number of input variables, which one(s) has greater influence on the output. By looking at its behaviour, the method will determine whether the effect of the input to the output is negligible, linear and additive or non-linear or input interactive behaved.

Based on the input variables, tuppled in a vector $\bar{x}$ of length k, each one uniformly partitioned into p levels, a grid of p^k points is assembled. Moreover, a perturbation Δ is performed to each of the variables x_i, one at a time. This way, the effect of the perturbation is used to analyze the effect on the response $y(\bar{x})$ in an isolated manner. To assess such perturbation, a parameter named elementary effect, function of the input space, $d(\bar{x})$ is used. For a case where the levels of an input is scaled between the range $[0, 1]$, $\Delta = \frac{p}{2(p-1)}$.

$$d(\bar{x}) = \frac{y(x_1, x_2, \ldots, x_{i-1}, x_i + \Delta, x_{i+1}, \ldots, x_k) - y(\bar{x})}{\Delta} \tag{B.4}$$

MOAT computes an r amount of elementary effects for each input variable and assembles it into an array F_i, which will contain a distribution of $d\bar{x}$. This method performs the amount of necessary computations in a limited amount of executions (compared to other methods), with a cost of $k/(k+1)$, which is the ratio of the necessary executions in order to gather the minimum required amount of data to perform the MOAT study.
The nature of the method is such, that the mean and modified mean, respectively shown below, are an unbiased represantation of the overall effect of the input to the output.

$$\mu_i = \frac{1}{r}\sum_{j=1}^{r} d_i^{(j)} \tag{B.5}$$

$$\mu_i^{\star} = \frac{1}{r}|\sum_{j=1}^{r} d_i^{(j)}| \tag{B.6}$$

Whereas the standard deviation will quantify the nonlinear effects or input interactions.

$$\sigma_i = \sqrt{\frac{1}{r}\sum_{j=1}^{r}\left(d_i^{(j)} - \mu_i\right)^2} \tag{B.7}$$

B.2 DOE results

In this section, further results from section 4.4 are shown, displaying the same information in a different format. The following plots considers the contours introduced in fig. 4.12 and directly looks into the various hull characteristics, without the post-processing explained in fig. 4.13. The hull characteristics are plot in the vertical axis while the mean impulse J_{mean}, is kept in the horizontal axis. Furthermore, the dashed lines corresponds to the upper side of the contours and the smooth lines to the lower side of the contours. Thus, the bottom-left corner is the Pareto front.
These plots, offers a direct illustration of the relation between the hull characteristics and the considered main objective function. The analysed parameters are namely, the dead rise angle β, the block coefficient C_b, the prismatic coefficient C_p and the relative LCF position with respect to LCB.

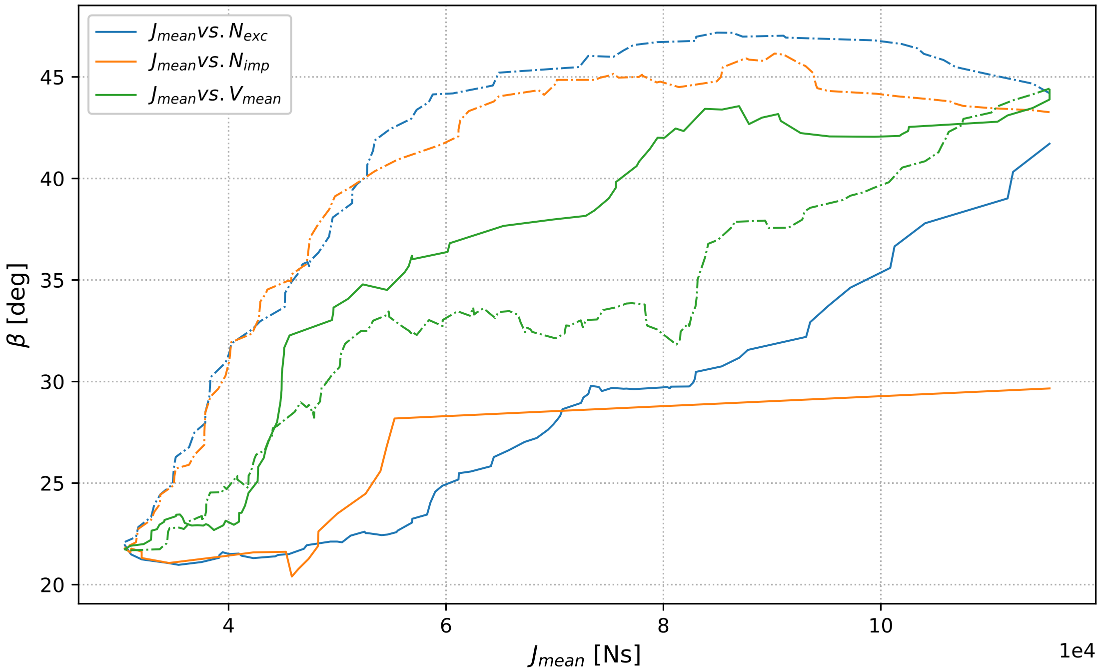

Figure B.1: Contour evaluation of the dead rise angles β with respect to J_{mean}.

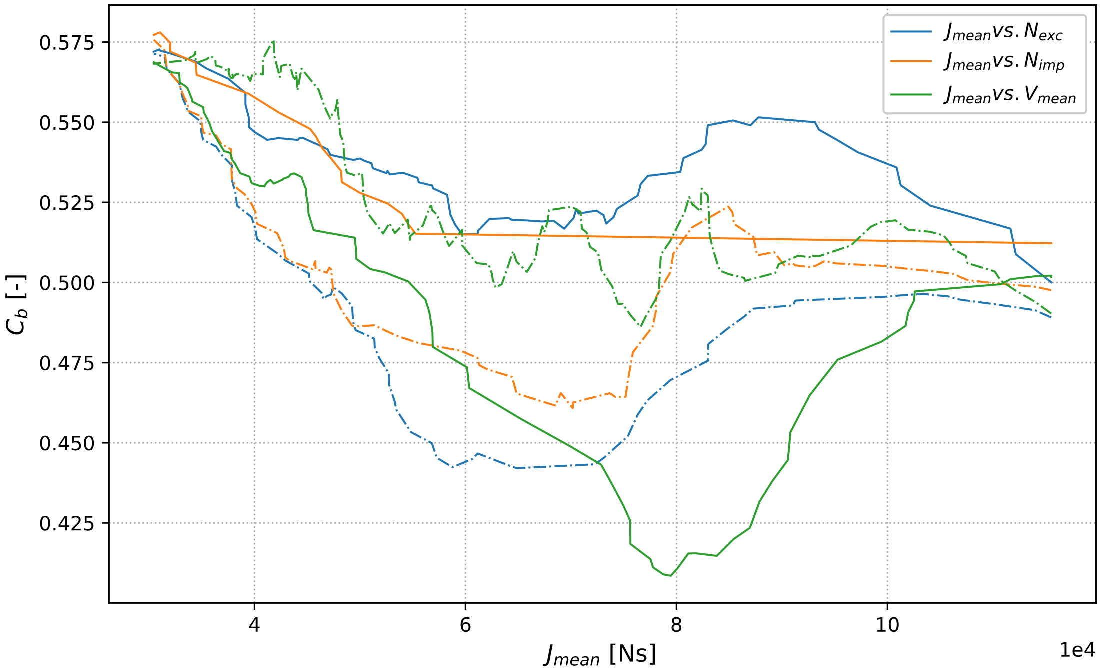

Figure B.2: Contour evaluation of the block coefficients C_b with respect to J_{mean}.

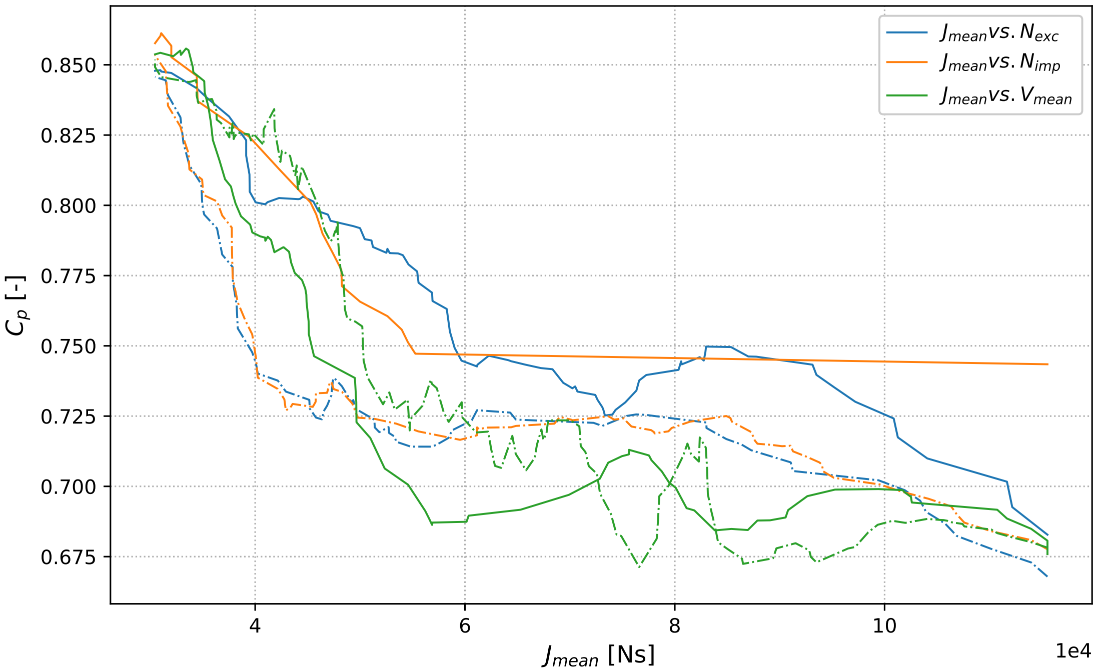

Figure B.3: Contour evaluation of the prismatic coefficients C_p with respect to J_{mean}.

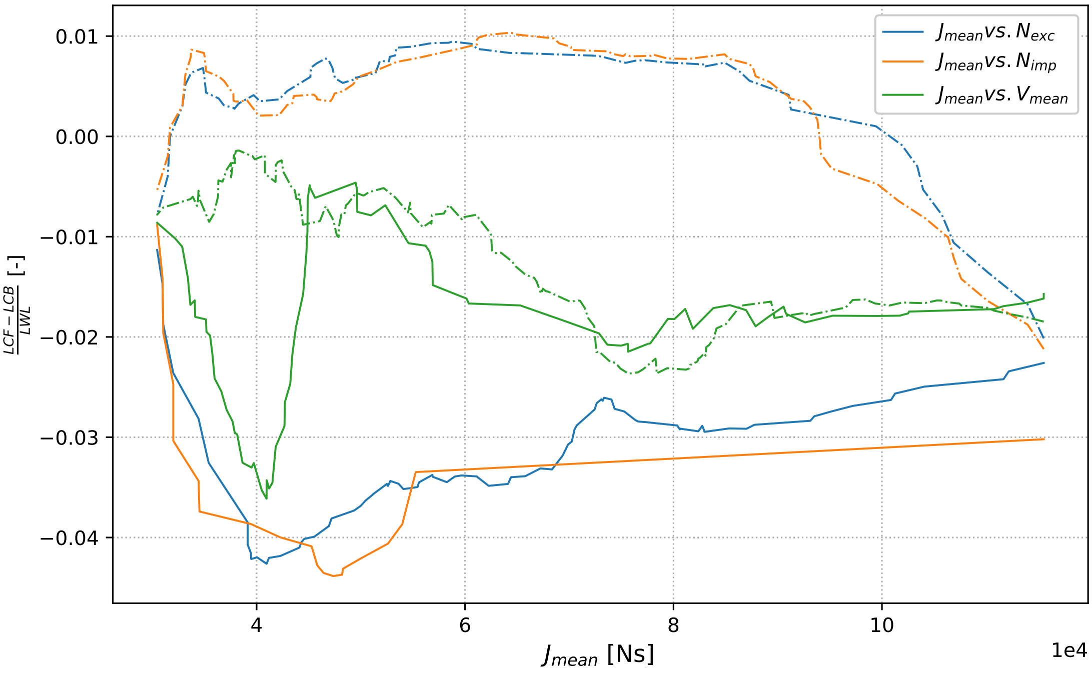

Figure B.4: Contour evaluation of the LCF position with respect to LCB $(LCF - LCB)/LWL$ with respect to J_{mean}.

Bibliography

[1] B.M. Adams, W.J. Bohnhoff, K.R. Dalbey, M.S. Ebeida, J.P. Eddy, M.S. Eldred, G. Geraci, R.W. Hooper, P.D. Hough, K.T. Hu, J.D. Jakeman, M. Khalil, K.A. Maupin, J.A. Monschke, E.M. Ridgway, A.A. Rushdi, J.A. Stephens, L.P. Swiler, D.M. Vigil, T.M. Wildey, , and J.G. Winokur. *Dakota, A Multilevel Parallel Object-Oriented Framework for Design Optimization, Parameter Estimation, Uncertainty Quantification, and Sensitivity Analysis: Version 6.11 User's Manual.* Sandia Technical Report SAND2014-4633; updated November 2019, July, 2014.

[2] B.M. Adams, W.J. Bohnhoff, K.R. Dalbey, M.S. Ebeida, J.P. Eddy, M.S. Eldred, G. Geraci, R.W. Hooper, P.D. Hough, K.T. Hu, J.D. Jakeman, M. Khalil, K.A. Maupin, J.A. Monschke, E.M. Ridgway, A.A. Rushdi, J.A. Stephens, L.P. Swiler, D.M. Vigil, T.M. Wildey, , and J.G. Winokur. *Dakota, A Multilevel Parallel Object-Oriented Framework for Design Optimization, Parameter Estimation, Uncertainty Quantification, and Sensitivity Analysis: Version 6.11 Reference Manual.* Sandia Technical Report SAND2014-4633; updated November 2019, July, 2014.

[3] B.M. Adams, W.J. Bohnhoff, K.R. Dalbey, M.S. Ebeida, J.P. Eddy, M.S. Eldred, G. Geraci, R.W. Hooper, P.D. Hough, K.T. Hu, J.D. Jakeman, M. Khalil, K.A. Maupin, J.A. Monschke, E.M. Ridgway, A.A. Rushdi, J.A. Stephens, L.P. Swiler, D.M. Vigil, T.M. Wildey, , and J.G. Winokur. *Dakota, A Multilevel Parallel Object-Oriented Framework for Design Optimization, Parameter Estimation, Uncertainty Quantification, and Sensitivity Analysis: Version 6.11 Theory Manual.* Sandia Technical Report SAND2014-4633; updated November 2019, July, 2014.

[4] R. L. Bisplinghoff and C.S.Doherty. Some studies of the impact of vee wedges on a water surface. *Journal of the Franklin Institute*, 253:547–561, 1952.

[5] MIT (Massachusetts Institute of Technology) Design of Ocean Systems. Lecture 9: Ocean wave environment. `https://ocw.mit.edu/courses/mechanical-engineering/2-019-design-of-ocean-systems-spring-2011/lecture-notes/`, March 7 2011.

[6] Det Norske Veritas & Germanischer Lloyd (DNVGL). Rules for classification: high speed and light craft. part 3: Structures, equipment. chapter 1: Design principles, design loads. December 2015.

[7] Q. Du, V. Faber, and M. Gunzburger. Centroidal voronoi tessellations: Applications and algorithms. *SIAM Review*, (41):637–676, 1999.

[8] K. Garme. *Modelling of planning craft in waves.* Royal Institute of Technology KTH, Department of Aeronautical and Vehicle Engineering, Stockholm, Sweden, September 2004.

[9] Raphael T. Haftka, Christian Gogu, and Felipe A. C. Viana. Making the most out of surrogate models: tricks of the trade. *ASME 2010 International Design Engineering*

Technical Conferences & Computers and Information in Engineering Conference, 28813, 2010.

[10] Kapsenberg G. K. Slamming of ships: where are we now? *Phil. Trans. R. Soc. A.*, 369: 2892–2919(1947), 2011.

[11] J.A. Keuning. Nonlinear behaviour of fast monohulls in head wave. *Delft University of Technology repository*, 1994.

[12] Freier L., Wiechert W., and von Lieres E. Kriging with trend functions nonlinear in their parameters: Theory and application in enzyme kinetics. *Engineering in Life Science*, (17):916–922, 2017.

[13] Pyrcz M. and University of Texas Data Analytics & Geostatistics. Pge 337: Spatial statistics: Kriging. `https://www.youtube.com/watch?v=CVkmuwF8cJ8`, November 9 2018.

[14] J. M. McFarland. Uncertainty analysis for computer simulations through validation and calibration. *PhD thesis, Vanderbilt University, Nashville, Tennessee*, 2008.

[15] M. D. Morris. Factorial sampling plans for preliminary computational experiments. *Technometrics*, 33(2):161–174, 1991.

[16] NIST/SEMATECH. e-handbook of statistical methods. *Engineering in Life Science*, 2012.

[17] Michel K. Ochi. Prediciton of slamming characteristics and hull responses for ship design. *SNAME Transactions*, 1973.

[18] P.R. Payne. The vertical impact of a wedge on a fluid. *Ocean Engineering*, 8(4):421–436, 1981.

[19] P.R. Payne. A unification in the added mass theory of planing. *Ocean Engineering*, 19(1):39–55, 1992.

[20] P.R. Payne. Recent developments in added mass planing theory. *Ocean Engineering*, 21(3):257–309, 1994.

[21] Babak Shabani, Jason Lavroff, Damien S. Holloway, Michael R. Davis, and Giles A. Thomas. The effect of centre bow and wet-deck geometry on wet-deck slamming loads and vertical bending moments of wave-piercing catamarans. *ELSEVIER, Ocean Engineering*, (169):401–417, 2018.

[22] Jalal Rafie Shahraki. *The influence of Hull Form on the Slamming Behaviour of Large High-Speed Catamarans.* NCMEH, Australian Maritime College, 2014.

[23] Ahmed Swidan, Giles Thomas, Dev Ranmuthugala, Irene Penesis, Walid Amin, Tom Allen, and Mark Battley. Prediction of slamming loads on catamaran wetdeck using cfd. *Conference: 13th International Conference on Fast Sea Transportation (FAST 2015)*, 1, 2015.

[24] Ahmed Abdelwahab Swidan. *Catamaran Wetdeck Slamming – A Numerical and Experimental Investigation.* NCMEH, Australian Maritime College, 2016.

[25] A.F.J. van Deyzen. A nonlinear mathematical model of motions of a planning monohull in head seas. *Delft University of Technology repository*, 2008.

[26] Hang Xie, Huilong Ren, Hui Lia, and Kaidong Tao. Numerical prediction of slamming on bow-flared section considering geometrical and kinematic asymmetry. *ELSEVIER, Ocean Engineering*, (158):311–330, 2018.

[27] E.E. Zarnick. A nonlinear mathematical model of motions of a planing boat in regular head waves. *David W. Taylor Naval Ship Research and Development Center, Bethesda, Md 20084, USA, Report Nr. DTNSRDC-78/032*, 1978.